

Modeling and Emulation of Induction Machines for Renewable Energy Systems

Mohammad Masadeh

A Thesis
In the Department
of
Electrical and Computer Engineering

Presented in Partial Fulfillment of the Requirements
For the Degree of
Doctor of Philosophy (Electrical and Computer Engineering) at
Concordia University
Montreal, Quebec, Canada

October 2018

© Mohammad Masadeh, 2018

Concordia University
School of Graduate Studies

This is to certify that the thesis prepared

By: Mohammad Masadeh

Entitled: Modeling and Emulation of Induction Machines for Renewable Energy Systems

and submitted in partial fulfillment of the requirements for the degree of

Doctor of Philosophy (Electrical & Computer Engineering)

complies with the regulations of the university and meets the accepted standards with respect to originality and quality.

Signed by the final examining committee:

_____	Chair
Dr. Adam Krzyzak	
_____	External Examiner
Dr. Kodjo Agbossou	
_____	External to Program
Dr. Muthukumaran Packirisamy	
_____	Examiner
Dr. Mohammad Zahangir Kabir	
_____	Examiner
Dr. Luiz A.C. Lopes	
_____	Thesis Supervisor
Dr. Pragasen Pillay	

Approved by:

Dr. Mustafa K. Mehmet Ali, Graduate Program Director

Wednesday, January 9, 2019

Dr. Amir Asif,
Dean, Gina Cody School of Engineering and Computer Science

Abstract

Modeling and Emulation of Induction Machines for Renewable Energy Systems

Mohammad Masadeh, Ph.D.

Concordia University, 2018

Electric motors with their drive systems utilize most of the generated power. They account for about two-thirds of industrial energy utilization and about 45% of the global energy utilization. Therefore, optimizing a motor and its corresponding drive system with their control can save energy and improve system efficiency. It can be risky and difficult however to test large prototype electrical machines and study their dynamic characteristics; or to test electric drives at high power levels with different machine ratings and operating conditions. One way to effectively evaluate these systems is to emulate the electric machine using a power electronic converter with the help of a real-time simulation system.

Power electronic converters and their control systems are increasingly being used in industries with different power ratings at high switching frequencies in the kHz range. In this thesis, an induction motor emulator based on a power electronic converter is developed to allow detailed testing the converter and controller. A proportional-resonant current controller in the abc-frame and pulse-width modulation are employed. The conventional model of the induction machine (IM) with constant parameters does not represent accurately the machine's performance for severe transients specifically during starting and loading conditions. Magnetic saturation effects should be considered. Hence, experimental procedures to determine the flux saturation characteristics in the main and both stator and rotor leakage flux paths are achieved. Machine models that consider or neglect the main and leakage flux saturation are compared with experimental results. The model which considers the magnetic saturation effect in both flux paths results in more accurate transient responses. Likewise, the dynamic response of the induction motor emulator during startup and loading transients show the effectiveness of using the developed emulator to resemble closely a real motor.

The relationship between the stator and rotor leakage reactance of the induction machine according to IEEE Std. 112™ is assumed to be constant under all operating conditions.

However, this is not accurate during severe transients such as the direct online startup and loading conditions of a three-phase induction motor. The leakage reactance of the machine can vary widely during severe conditions. Hence, using constant parameters in the machine model will result in an inaccurate dynamic performance prediction. Moreover, considering a constant ratio between the stator and rotor leakage reactance is no longer valid for all current levels. In this thesis, a direct and precise method is proposed to estimate and separate the stator and rotor leakage reactance parameters under normal operating conditions and when the core is deeply saturated. The method exploits the 2D time-stepping finite element method (FEM) with a coupled circuit. The obtained current-dependent reactance functions in both leakage flux paths are included in the dq-model of the IM. Other machine parameters are determined by implementing the standard tests in FEM. To verify the effectiveness of the proposed method, the predicted results are compared to the dynamic responses obtained experimentally from a three-phase, 5-hp squirrel-cage IM.

A power electronic converter-based self-excited induction generator (SEIG) emulator is developed. The testbed replaces a wind- or microhydro-turbine driven squirrel-cage induction generator that works within an isolated power system to feed power in remote areas. It supports testing and analyzing the dynamic performance of islanded generation systems which comprise numerous kinds of parallel-operated renewable energy sources. The risk and cost associated with the testing, analysis and development of novel control topologies and electrical machine prototypes are reduced considerably. The dq-model of the SEIG in the rotor reference frame is implemented in a real-time controller. Saturation in the main and leakage flux paths are included in the machine model. The generator model with modified parameters is verified and used in the emulator. The cascaded voltage and current loops utilizing the proportional-integral controllers in dq-frame are employed. A voltage-type ideal transformer model is used as a power interface for the emulator whereas an excitation capacitance is added to the power-hardware-in-the-loop block diagram. Likewise, the dynamic response of the induction generator emulator during voltage buildup and loading conditions validates the effectiveness of using the developed emulator to resemble closely a real generator.

Acknowledgments

All the praise and thanks be to *Allah*, God the Almighty, most beneficent and most merciful.

I would like to express my deep appreciation and gratefulness to my supervisor *Professor Pragasan Pillay* for his patience, kind support and professional guidance throughout these years that finally crowned with lots of knowledge and experience.

I would also like to thank my committee members, *Professor Luiz A.C. Lopes*, *Professor Muthukumaran Packirisamy*, *Professor Mohammad Zahangir Kabir*, and *Professor Kodjo Agbossou* for being as committee members even at hardship and for the bright comments, suggestions, and valuable time.

A special thanks to my family back home for their prayers and continuous support especially my great parents, *Dr. Ali Saleem Masadeh* and *Mrs. Rasmiyeh Ali Hussein*. Many thanks for all the sacrifices and prayers in which sustained me thus far.

I would also like to thank my beloved wife *Mrs. Muna Al-Kassawneh* who supported me morally during my research and express my gratitude to my beautiful kids *Rayan*, *Leen* and *Larin* for the long lonely hours they spent while I was busy with this research.

Many thanks to my colleagues in the Power Electronics and Energy Research (PEER) group of Concordia University for the wonderful research environment I have experienced during the years I spent with them. I would like to thank *Dr. Maher Al-Badri*, *Dr. Maged Ibrahim*, *Dr. Mohammadhossein Ashourianjozdani*, and *Mr. Amitkumar Kortagere* for the advice and valuable discussions.

I would like to acknowledge Philadelphia University-Amman, Jordan for the financial support under a scholarship program and Concordia University for the numerous financial awards. I also acknowledge the support of the Natural Sciences & Engineering Research Council (NSERC) of Canada and Hydro-Québec for this work.

Table of Contents

List of Tables	ix
List of Figures	x
List of Abbreviations	xiv
List of Symbols	xvi
Chapter 1. Introduction	1
1.1 General	1
1.2 Problem Statement	2
1.3 Motivation	3
1.4 Objectives	3
1.5 Limitations	5
1.6 Literature Review	5
1.7 Thesis Outline	12
1.8 Thesis Contributions	14
1.8.1 Journal papers	14
1.8.2 Conference papers	14
Chapter 2. Induction Machine Model with Modified Parameters	15
2.1 Introduction	15
2.2 Induction Machine Dynamic Model	15
2.3 Conventional Induction Machine Model	16
2.4 Induction Machine Model Including Flux Saturation Effect	18
2.4.1 Magnetizing reactance calculation	19
2.4.2 Stator and rotor leakage reactance calculation	21
2.5 Experimental and Simulation Results	23
2.6 Summary	24
Chapter 3. Impact of the Stator/Rotor Leakage Split Ratio on Induction Machine Performance	25
3.1 Introduction	25
3.2 Finite Element Model with Coupled Circuit	26
3.3 Stator Leakage Reactance Estimation	28

3.3.1	Method I: Calculation when the rotor is removed and replaced by air	28
3.3.2	Method II – Proposed Method: Calculation when the rotor has a non-magnetic material with $\mu_r = 10^{-6}$	32
3.4	Experimental and Simulation Results.....	38
3.4.1	FEM-based machine parameters with a constant X_{ls}/X_{lr} ratio.....	38
3.4.2	FEM-based machine parameters with a variable X_{ls}/X_{lr} ratio	39
3.4.3	FEM- and Matlab/Simulink- based IM performance including the saturation effect with variable X_{ls}/X_{lr} ratio compared to the experimental IM dynamic response	43
3.5	Summary.....	45
Chapter 4.	Power Electronics Converter-Based Induction Motor Emulator Including Main and Leakage Flux Saturation.....	46
4.1	Introduction	46
4.2	Induction Motor Emulator Structure	48
4.2.1	Voltage source converters	48
4.2.2	Synchronous reference frame phase-locked loop.....	49
4.2.3	Coupling network	51
4.3	Current Controller Design	53
4.4	Experimental Results and Discussion	57
4.5	Summary.....	62
Chapter 5.	Self-Excited Induction Generator Emulator for Renewable Energy Tests within an Isolated Power System	64
5.1	Introduction	64
5.2	Self-Excited Induction Generator Model with Modified Parameters.....	66
5.3	Self-Excited Induction Generator Emulator Structure	70
5.4	Block Diagram and Stability of the PHIL Emulation System.....	71
5.5	Voltage Source Converter Modeling and Control.....	74
5.5.1	Current control scheme.....	75
5.5.2	Voltage control scheme	77
5.6	Experimental Results and Discussion	82
5.6.1	SEIG Model with modified parameters verification	83

5.6.2	SEIG emulator during voltage buildup.....	87
5.6.3	SEIG emulator during loading condition	90
5.7	Summary.....	94
Chapter 6.	Conclusions and Future Work.....	95
6.1	Conclusions	95
6.2	Future Work.....	97
References	99
Appendix - A	106
abc/dq	Coordinates Transformation.....	106
Appendix - B	107
LCL	Transfer Function.....	107
Appendix - C	108
System	Parameters and Specifications	108

List of Tables

Table 1-1 Summary of induction motor emulation in the literature.	11
Table 2-1 IM measured parameters based on IEEE Std-112™ and specifications at rated conditions.	19
Table 3-1 Comparison between the total stator leakage reactance calculated in FEM using the two methods and the measured value at the rated current condition.....	34
Table 3-2 Comparison between experimental and FEM-based parameters of the 5-hp induction machine with a constant X_{ls}/X_{lr} ratio	39
Table C-1 IM under test specifications and some design parameters	108
Table C-2 SEIG measured parameters and specifications.....	108
Table C-3 Magnetizing and leakage reactance saturation parameters.....	108
Table C-4 Hardware and control systems parameters	109

List of Figures

Fig. 1-1	Conventional test platform and the power electronic-based emulator.	2
Fig. 1-2	Physical load connected to the application under test (AUT).	5
Fig. 1-3	Induction motor PHIL simulation using LinVerter [13].	8
Fig. 1-4	Inverter control for emulation of a synchronous generator [18].	9
Fig. 2-1	Three-phase induction machine windings distribution in abc and dq axes [5].	15
Fig. 2-2	dq-equivalent circuit for a three-phase induction machine (0-axis is neglected) [4].	16
Fig. 2-3	No-load measured magnetization curve for the 5-hp machine and the corresponding main reactance.	20
Fig. 2-4	Leakage reactance measurements for the 5-hp machine.	22
Fig. 2-5	Predicted line current response during DOL startup of the 5-hp IM at rated voltage compared to the measured current response. (a) Model without saturation. (b) Model with saturation.	23
Fig. 2-6	Predicted speed response during DOL startup of the 5-hp IM at rated voltage compared to the measured speed response. (a) Model without saturation. (b) Model with saturation.	24
Fig. 3-1	Electromagnetic coupled circuit model in MagNet. (a) Stator circuit and (b) Part of the rotor circuit.	28
Fig. 3-2	Magnetic flux distribution in the induction machine when the rotor is removed and space is replaced by air: (a) flux density map and (b) flux lines.	30
Fig. 3-3	Magnetic vector potential: (a) Its distribution along the outer diameter of the rotor space and (b) spectrum analysis.	31
Fig. 3-4	Magnetic flux distribution in the induction machine when the rotor space is replaced by a non-magnetic material with $\mu r = 10 - 6$. (a) Flux density map. (b) Flux lines. (c) Enlarged view.....	33
Fig. 3-5	Variation of the stator and rotor leakage reactance with current using the FEM for the 5-hp IM.	35
Fig. 3-6	The electromagnetic coupled circuit of the stator in MagNet during the locked-rotor test of IM for rotor leakage reactance estimation.	35

Fig. 3-7	Experimental measurements of the total leakage reactance for the 5-hp machine compared to the calculated values using FEM with the current.....	37
Fig. 3-8	Stator to rotor leakage reactance ratio with current estimated in FEM.....	38
Fig. 3-9	Predicted current response during DOL startup of a 5-hp IM compared to the experimentally measured current when: (a) the machine model includes the saturation effect with a constant leakage reactance ratio and (b) the machine model includes the saturation effect with a variable leakage reactance ratio.....	40
Fig. 3-10	Predicted speed response during DOL startup of a 5-hp IM compared to the experimentally measured speed when: (a) the machine model includes the saturation effect with a constant leakage reactance ratio and (b) the machine model includes the saturation effect with a variable leakage reactance ratio.....	40
Fig. 3-11	Machine parameters variation during DOL startup, SS with no-load, and loading condition. (a) Line current response. (b) Stator leakage reactance. (c) Rotor leakage reactance. (d) Leakage reactance ratio.....	42
Fig. 3-12	Current response during DOL startup of the 5-hp IM.....	43
Fig. 3-13	Speed response during DOL startup of the 5-hp IM.....	44
Fig. 3-14	Electromagnetic torque response during DOL startup of the 5-hp IM.....	44
Fig. 4-1	Emulator structure with abc-reference frame current control.....	48
Fig. 4-2	A three-phase synchronous reference frame PLL. (a) General structure. (b) PLL response to varying grid frequency 60.5 Hz and a phase jump of 90°.....	50
Fig. 4-3	Grid-emulator network coupling per-phase using: (a) An L. (b) An LC. (c) An LCL.....	52
Fig. 4-4	Equivalent circuit for a single-phase LCL filter.....	52
Fig. 4-5	Equivalent circuit for a single-phase LCL filter.....	53
Fig. 4-6	Block diagram of the AC-input current control system.....	54
Fig. 4-7	Bode plot of PR current controller with different values for Kr	55
Fig. 4-8	Bode plot of PR current controller with damping factor $\omega_{co} = 10$ rad/s, $Kp = 1$, and $Kr = 100$	57
Fig. 4-9	Experimental setup for the power electronic-based induction motor emulation system.....	58

Fig. 4-10	Experimental phase current response drawn by the 5-hp IM emulator during the DOL startup with 60% of the rated voltage and no-load compared to the current drawn by the IM model in RTS.	59
Fig. 4-11	Experimental phase current response of the 5-hp IM PEC-based emulator at 60% of the rated voltage and no-load condition compared to the real machine's current response under similar operating conditions during: (a) DOL startup and (b) steady-state operation.	60
Fig. 4-12	Experimental current response drawn by (a) the 5-hp IM during loading condition of 12 N.m at 60% of the rated voltage and (b) the IM emulator running under the same operating conditions.	61
Fig. 4-13	Experimental current response drawn by (a) the 5-hp IM at steady-state with a load torque of 12 N.m and 60% of rated voltage and (b) the IM emulator running under the same operating conditions.	62
Fig. 5-1	Equivalent circuits of SEIG squirrel-cage type in the dq-coordinates and arbitrary reference frame	67
Fig. 5-2	General block diagram for the SEIG in dq-frame.	69
Fig. 5-3	Equivalent circuit. (a) The original system. (b) PHIL with voltage-type ITM power interface for the SEIG emulator.....	71
Fig. 5-4	Block diagram of the PHIL for the SEIG emulator. (a) Block diagram for the equivalent circuit. (b) Reduced block diagram.....	72
Fig. 5-5	Schematic diagram of the developed emulator with the cascaded control system...	74
Fig. 5-6	Block diagram for the current control scheme of the SEIG emulator.	75
Fig. 5-7	Block diagram for the voltage across the filter capacitance the SEIG emulator.	78
Fig. 5-8	Block diagram for the voltage control scheme of the SEIG emulator.....	78
Fig. 5-9	Open-loop system Bode plot.	81
Fig. 5-10	Experimental setup for the converter-based SEIG emulator system.	83
Fig. 5-11	Measured and predicted output performance of the 5-hp SEIG for two different excitation capacitance values. (a) V-I output characteristics. (b) P-I output characteristics.	84
Fig. 5-12	Predicted response of the 5-hp SEIG during buildup with $C = 36 \mu\text{F}$. (a) Frequency. (b) Generator terminal voltage. (c) Generator line current.....	85

Fig. 5-13	Measured responses of real 5-hp SEIG during buildup with $C = 36 \mu\text{F}$. (a) Frequency. (b) Generator terminal voltage. (c) Generator line current.....	86
Fig. 5-14	Experimental results of the SEIG emulator buildup process at no-load with $C = 40 \mu\text{F}$; (a) output frequency, (b) generator model terminal voltage in RTS, (c) generator emulator terminal voltage, (d) a zoom-in during building up at $t = 7.7 \text{ s}$, (e) a zoom-in at steady-state at around $t = 35 \text{ s}$	88
Fig. 5-15	Measured leakage and magnetizing reactance parameters variation in RT during voltage buildup at no-load condition of the SEIG emulator.....	89
Fig. 5-16	Measured output voltage of the SEIG emulator during voltage buildup at no-load condition compared to the one calculated in RTS; (a) d-axis generator terminal voltage, (b) q-axis generator voltage.	90
Fig. 5-17	Experimental results of the SEIG emulator during loading condition with $R_L = 25 \Omega$; (a) generator terminal voltage in RTS, (b) emulator terminal voltage, (c) zoom-in during loading condition around $t = 11.8 \text{ s}$, (d) zoom-in at steady-state at around $t = 20 \text{ s}$, and (e) actual load current.....	92
Fig. 5-18	Measured leakage and magnetizing reactance parameters variation in RT during SEIG emulator loading condition with $R_L = 25 \Omega$	92
Fig. 5-19	Experimental results of the SEIG emulator during loading condition with $R_L = 25 \Omega$; (a) generator emulator torque calculated in real-time, (b) generator slip ratio.....	93
Fig. 5-20	Measured output voltage of the SEIG emulator during loading condition with $R_L = 25 \Omega$ compared to the one calculated in RTS; (a) d-axis generator terminal voltage and (b) q-axis generator terminal voltage.....	93

List of Abbreviations

Symbol	Description
2D	Two-Dimension
A/D	Analog-to-Digital Converter
AC	Alternating Current
AFEC	Active Front-End Converter
AUT	Application Under Test
D/A	Digital-to-Analog Converter
d-axis	Direct-Axis
DC	Direct Current
DOL	Direct Online operation
EMF	Electro-Motive Force
FEM	Finite-Element Method
IEC	International Electrotechnical Commission
IEEE	Institute of Electrical and Electronic Engineers
IGBT	Insulated Gate Bipolar Transistor
IM	Induction Machine
IME	Induction Machine Emulation
ITM	Ideal Transformer Model
LPF	Low Pass Filter
MVP	Magnetic Vector Potential
PEC	Power Electronic Converter
PHIL	Power Hardware-in-the-Loop
PI-Controller	Proportional-Integral Controller
PLL	Phase-Locked Loop
PR-Controller	Proportional-Resonant Controller
PV	Photovoltaic
PWM	Pulse Width Modulation

q-axis	Quadrature-Axis
RCP	Rapid Control Prototyping
RMS	Root Mean Square
RPM	Revolutions per Minute
RT	Real-Time
RTS	Real-Time Simulator
SEIG	Self-Excited Induction Generator
SS	Steady-State
VSC	Voltage Source Converter
VSI	Voltage Source Inverter

List of Symbols

Symbol	Unit	Definition
B	T	Flux density
B_m	-	Machine friction coefficient
C	F	Excitation capacitance
C_f	F	Shunt capacitor filter
$c_{1,2}, \dots$	-	Curve fitting parameters
H	A/m	Magnetic field intensity
i_{dr}	A	d-axis rotor current
i_{ds}	A	d-axis stator current
i_{qr}	A	q-axis rotor current
i_{qs}	A	q-axis stator current
i_{Cd}	A	d-axis excitation capacitor current
i_{Cq}	A	q-axis excitation capacitor current
i_{Ld}	A	d-axis load current
i_{Lq}	A	q-axis load current
i_m	A	Main or magnetizing current
$i_{i\ abc}$	A	SEIG emulator inverter-side abc-current
$i_{o\ abc}$	A	SEIG emulator load-side abc-current
i_{id}	A	d-axis SEIG emulator inverter-side current
i_{iq}	A	q-axis SEIG emulator inverter-side current
i_φ	A	Phase current
I_m	A	Magnetizing amplitude current value
I_r	A	Rotor amplitude current value
I_s	A	Stator amplitude current value
J_m	Kg.m ²	Moment of inertia of the rotor and connected load
$k_{1,2}, \dots$	-	Curve fitting parameters
K_I	-	Integral controller gain
K_P	-	Proportional controller gain
k_w	-	Stator winding factor
L_f	H	Inductance of the coupling filter

L_{ls}	H	Stator leakage inductance
L_{lr}	H	Rotor leakage inductance
L_M	H	Magnetizing (main) inductance
m_{abc}	-	abc-frame modulation indices
m_d	-	d-axis modulation index
m_q	-	q-axis modulation index
P	-	Number of poles in the machine
R_f	Ω	Internal resistance of the coupling filter
R_L	Ω	Load resistance
R_r	Ω	Rotor resistance
R_s	Ω	Stator resistance
s	-	Laplace operator
T	-	abc/dq coordinate transformation matrix
T_d	sec	Total time delay
V_m	V	Peak value (amplitude) of the voltage signal
v_{ds}	V	d-axis stator voltage
v_{qs}	V	q-axis stator voltage
v_{dr}	V	d-axis rotor voltage
v_{qr}	V	q-axis rotor voltage
v_{Ld}	V	d-axis load voltage
v_{Lq}	V	q-axis load voltage
v_{Cd}	V	d-axis excitation capacitor voltage
v_{Cq}	V	q-axis excitation capacitor voltage
v_{conv}	V	Converter-side voltage per-phase
v_g	V	Grid-side voltage per-phase
V_φ	V	Phase voltage
X_{ls}	Ω	Stator leakage reactance
X_{lr}	Ω	Rotor leakage reactance
X_M	Ω	Magnetizing (main) reactance
Z	Ω	Machine impedance during blocked-rotor test
λ_0	Wb-turn	Residual flux linkage
λ_{ds}	Wb-turn	d-axis stator flux linkage

λ_{qs}	Wb-turn	q-axis stator flux linkage
λ_{dr}	Wb-turn	d-axis rotor flux linkage
λ_{qr}	Wb-turn	q-axis rotor flux linkage
μ_o	H/m	Magnetic permeability of the air
μ_r	-	Relative magnetic permeability
μ	H/m	Magnetic permeability of the material
ω	Rad/s	Electrical-angular speed in the arbitrary reference frame
ω_r	Rad/s	Electrical-rotor angular speed
ω_s	Rad/s	Electrical-stator angular speed
ω_m	Rad/s	Mechanical-rotor angular speed
ω_c	Rad/s	Controller cutoff angular frequency
ω_o	Rad/s	PR-controller resonant angular frequency
ω_{co}	Rad/s	PR-controller cutoff frequency
θ	Rad	Arbitrary dq-frame angle
θ_r	Rad	Rotor angle
$\frac{d}{dt}$	-	Derivative operator
*	-	Superscript indicates reference signal
$[\]^T$	-	Superscript indicates matrix transpose

Chapter 1. Introduction

1.1 General

Electric motors convert electrical power into mechanical power within a motor-drive system. The large majority of electricity used by electric motor drive systems is converted by the electric motor itself. Only a very small portion of energy is used to power control functions or other auxiliary circuits.

Electric motors with their drive systems are the sole largest utilizers of electricity in industry. They account for about two-thirds of industrial electrical power consumption and about 45% of global electrical power consumption, giving rise to about 6040 million tonnes of CO₂ emissions. By 2030, without effective energy technology procedures, energy consumption from electric motors and their drive systems is expected to escalate to 13360 TWh per year and to 8570 million tonnes of CO₂ emissions per year [1], [2].

The majority of electric motors and their drives operate with low efficiency, are oversized, or run unnecessarily. This has significant environmental and economic implications. Choosing and optimizing an electric motor and its related drive system can typically improve system efficiency by 20% to 25%, which in turn can reflect energy savings by as much as 7% of total global electric power demand [3].

Power electronic converters and their control of electromechanical systems are extensively used in industries at different power rating levels. These systems employ electronic devices which can run at high switching frequencies in several kHz. The load can be static such as a transformer or dynamic such as a motor or a generator. The power electronic converter which is intended to be used in an electric drive system is usually tested by connecting it to standard equipment such as a motor or generator. The machine, however, may not have the specifications and characteristics that are desired for a specific test or may not be well-matched to the intended application. Moreover, some characteristics of the mechanical load or prime mover should be included in the test in order to realize the effect for longer terms. All of those operating conditions are difficult to replicate in the laboratory.

It is possible for the electromechanical system with its associated load, as the one shown in Fig. 1-1 (upper part), to be replaced with power electronics devices that can be controlled and flexibly programmed to emulate the real machine. An emulator can be implemented with a bidirectional power electronic interface as depicted in Fig. 1-1 (lower part). It can be controlled to run either as an energy sink which draws electrical energy from the grid e.g. inverter or any

other application under test (AUT), or as an energy source supplying electrical power back to the grid. Moreover, it can be utilized to provide different load characteristics by which various control topologies and industrial inverter designs can be tested. Therefore, it can facilitate testing both the hardware and software of the inverter, which will offer a more flexible platform for testing inverters in a laboratory environment. Moreover, the various power losses available in the conventional test platform such as mechanical, electrical, and magnetic losses will be limited to few watts due to switching losses.

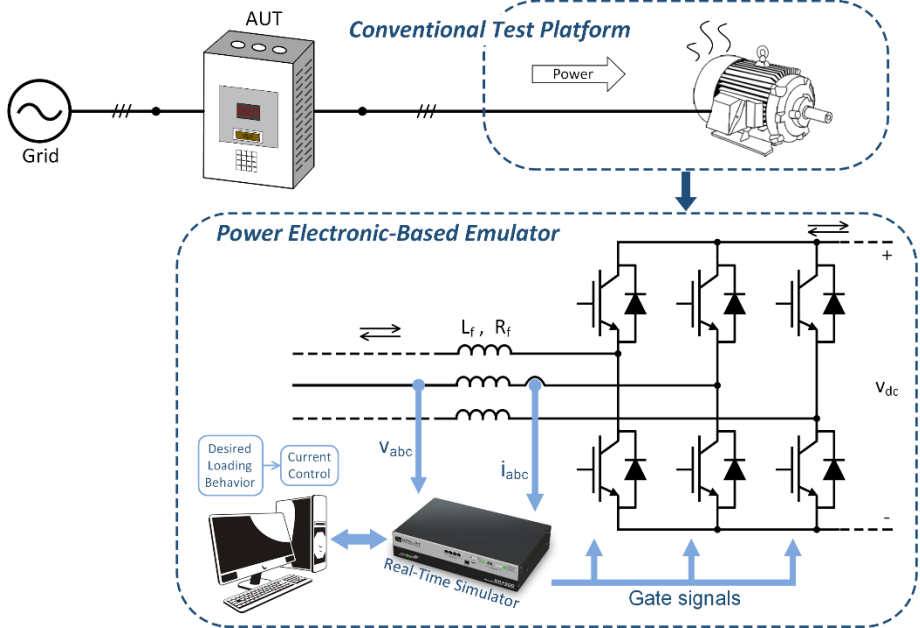


Fig. 1-1 Conventional test platform and the power electronic-based emulator.

1.2 Problem Statement

This research presents a method to emulate induction machines by utilizing the concept of power hardware-in-the-loop along with a comprehensive model of the machine and load dynamics. This will eliminate the need for expensive test benches and equipment, and avoid the risk associated with development and testing of new drive systems, electrical machine prototypes, and novel control schemes as well as any combination of the aforesaid functions.

The existing emulation systems do not include the saturation effect in the machine model. Moreover, they do not discuss the application of induction machine emulation in the generation mode. For induction motor emulations, most of the work done in this field involve high ripples in the drawn current and produced torque. Also, there is inaccurate tracking and correlation with real current measurements.

1.3 Motivation

Designing and developing a three-phase induction machine emulation platform is important for testing operation and control topologies of low, medium, and high power rating machines. Moreover, it will help in testing the operation and control of novel drive systems in real-time operation, which is presently considered expensive and inaccessible.

The dynamic conditions of online starting and power load transients of a large three-phase industrial induction motor as well as the full details of stator and rotor current dynamic responses including induced high-frequency current oscillations are crucial in the evaluation of transient stability events for real-time emulation systems. This research will study the transient as well as the steady-state characteristics of a three-phase induction machine when it is run either as a motor or generator. The dynamic responses when it is subjected to different types of mechanical or electrical disturbances will also be considered.

The design of a three-phase induction machine emulation system is based on the concept of constructing a stand-alone power electronic dynamic emulator with the capability for bidirectional power flow and connecting it to peripheral equipment. For easy structure rearrangement and flexible control scenarios, the induction machine model and its load dynamics will be built in the real-time environment. A comprehensive model will be simulated in Matlab/Simulink by using the well-known dq-coordinate mathematical model [4], [5], [6] in the synchronously rotating reference frame. The appropriate control signals generated by the simulation will be used in the control system in which it will be achieved in different reference frames such as the dq-synchronous reference frame control, and the natural abc-frame control.

1.4 Objectives

The main objective of this work is to design and develop a three-phase bidirectional power electronic converter to be utilized as an emulator test platform. The other specific objectives of the emulation system include:

- Building a comprehensive mathematical model for a three-phase induction machine. The machine model with modified parameters will be run in the real-time simulator and used in the emulation system. This embraces:
 - a) Including the saturation effect in the main as well as both stator and rotor leakage flux paths in the machine model.

- b) Proposing a direct and precise method to estimate and separate the stator and rotor leakage reactance parameters under normal operating conditions and when the core is deeply saturated. The technique exploits a two-dimensional, time-stepping finite element method with a coupled circuit. The obtained current-dependent reactance functions in both main and leakage flux paths are included in the dq-model of the induction machine.
 - c) Studying the impact of the stator-to-rotor leakage split ratio on the induction machine performance.
- Building an induction machine emulation test platform in the motoring mode. This includes:
 - a) Utilizing the dq-model of the three-phase induction motor in the synchronous reference frame. Moreover, the machine model with modified parameters is implemented in the real-time within the emulation system.
 - b) Designing and setting up the power electronic converter with the coupling inductor.
 - c) Emulating the behavior of induction motor startup and load variation by applying the current control strategy in the natural abc-frame and utilizing the proportional-resonant controller and then, validating the induction motor emulator outputs compared to the results of real motor dynamics.
 - Building a test platform for the induction machine emulation running in the generating mode. This includes:
 - a) Modifying and verifying the mathematical model of the three-phase induction machine model which will run as a self-excited squirrel-cage induction generator with linear load specifically, resistive type.
 - b) Designing the emulating converter cascaded voltage and current controllers. The two loops utilize the proportional-integral in the dq-frame.
 - c) Using a voltage-type ideal transformer model as a power interface for the emulator whereas the excitation capacitance is added to the power hardware-in-the-loop block diagram and validating the dynamic response of the induction generator emulator during voltage buildup and loading conditions

1.5 Limitations

The power level of the emulation system is one of the most important limitations. Therefore, re-scaling the emulator may be utilized. Moreover, increasing the switching frequency for the high-level power emulator results in high power losses. For large scale power electronics testing, the power consumption during the test is still a major limitation.

The complexity of the emulation process is limited by the capability of the bidirectional power converter and the real-time simulation that controls its operation mode. Moreover, the sampling frequency of the emulator is a significant specification of the emulation system when it is used for testing the drive and its control. It should be at least equal to the switching frequency of the emulating converter. This feature limits the application of the emulation system. The emulator's converter is connected to passive components and time-dependent equipment such as inductive filters and capacitors which slow down the system and hence, reduce its total bandwidth. The inductance value should, therefore, be carefully chosen as a compromise between fast transient response and low drawn current ripples.

1.6 Literature Review

Various physical power loads (i.e. resistors, inductors, capacitors, ac/dc motors, and converters) can be used to offer controllable load options in order to provide power loading conditions for application under test (AUT) as shown in Fig. 1-2.

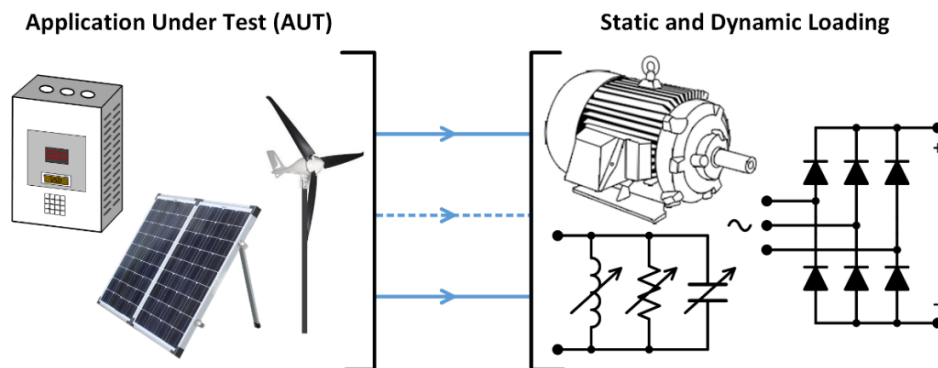


Fig. 1-2 Physical load connected to the application under test (AUT).

During the development of a hardware-in-loop (HIL) simulation system for testing operation and control of micro-grids as reported in [7], the electric load was represented by fixed resistive and inductive loads controlled by separate tap-change transformers to achieve different

load profiles. Due to large power consumption, size, limitation in a laboratory environment, and fixed setup, a passive load could not provide flexible loading profiles nor compact design due to the need for a massive cooling fan. Inability to represent the exact system is one disadvantage of using physical loads.

Test platforms and prototypes for low power machines are relatively inexpensive and accessible. However, as power levels rise into the upper kilowatt and megawatt ranges, validation of prototype machines and drives becomes costly and risky. Dimensional analysis was used in the 1960s to get preliminary test results before constructing a prototype by establishing laws of similitude between the original and its model [8]. The shortcoming of this approach lies in the difficulty of scaling the ratio of machine inertia to frictional loss [9]. Alternatively, power electronics are known for their fast, accurate, and flexible control algorithms, and different power stage options. Hence, it is feasible to use power electronics and their controls to mimic static or slow time-scale electrical dynamics (milliseconds). It can ease testing both the hardware and software of the AUT, which will offer a more safe and flexible platform for testing devices and novel control schemes in a laboratory environment.

Power electronic converters can be controlled to emulate numerous kinds of dynamic systems or machines such as induction motors as achieved in [10] - [15], synchronous generators as in [16] - [19], and static systems or machines such as transformers and different power system loads for diverse testing purposes as in [20] - [27]. Examples of emulating renewable energy systems in a hardware testbed (HTB) are also available in the literature [28] - [33]. Machine emulation is achieved by simulating the dynamic model of the required system component inside a real-time controller. The generated current and voltage commands of the model can then be used as reference signals for the power converter to track and achieve. This offers a flexible and easy way to test and analyze the characteristics of the emulated machine or device under test at particular operating conditions. With proper controller design, converters can behave in a similar manner to the real device.

Several converter-based emulators, or power hardware-in-loop systems, have been proposed in order to emulate machines with different parameters and with wide power ranges for diverse testing purposes.

An induction machine emulation (IME) test platform based on an HIL model is implemented in [10]. The electrical machine and its load dynamics are simulated with a real-

time digital simulator (RTDS) which supplies control reference signals to a power electronics converter that is interfaced with a variable speed drive (VSD) via a transformer-based LCL-type coupling network. The coupling impedance is assumed to be constant however it can vary depending on the VSD operating frequency and on imbalances in the transformer leakage reactance. This variation can result in inaccuracies in the IME. The proposed IME is limited with a minimum operating frequency due to the coupling transformer saturation effect which is not considered in the IME model. It is also limited by the natural filtering effect which results in unstable operation of the IME and overcurrent tripping of the HIL power converter. The IME is also limited with an upper bandwidth which is constrained by the maximum switching frequency of the converter. This limits the system's ability to respond to different transients such as load torque variations. Another drawback of the proposed IME is the initial peak voltage of 10 V that is required for a stable phase-locked loop (PLL) prior to enabling the IM model operation. Also, there is a delay due to the sampling of the measured voltage, computation, and production of the reference signals from the RTDS.

A three-phase induction motor emulator based on a power electronic converter (PEC) in a rectifier mode is introduced in [11]. The induction machine is mathematically modeled using the dq-synchronously rotating reference frame. During start-up, the proposed PEC-based induction motor emulator shows similar output responses of an induction motor. However, the experimental results do not agree well with output results of the induction motor model. Moreover, the results show different torque and speed transients, specifically in torque transients and settling time of the motor speed.

The dynamics of an inverter-virtual induction machine is examined in [12] using a hardware-based inverter and real-time simulation of an induction motor. The inverter is connected to a bidirectional power electronic ac/ac converter through a line inductor. The stator currents obtained from the induction motor model are used as reference signals to control the drawn current from the inverter and to match the current that would be drawn if the inverter was connected to a real motor. To accommodate the induction motor model from the output voltages of the inverter, a voltage sampling system at high frequency is designed.

In an attempt to increase the power and frequency capabilities of the HIL platform, a multilevel parallel switch-based converter is applied in [13]. The work proposes a motor drive test-bed with induction machine and load model controlled by multilevel bridge based

‘LinVerter’ shown in Fig. 1-3. The figure reveals a single-phase representation of the converter within the ‘LinVerter’ frame. The virtual test platform had a motor emulator and regenerative converter to regulate the dc voltage and feedback power to the grid. It draws the same currents from the motor drive performing field oriented-control as motor-load combination during transient and steady-state conditions. It shows a high bandwidth and low-harmonic current content. The drawback however of this topology includes the cost of structural complexity in the three-phase ‘LinVerter’, and large numbers of devices and common-mode chokes.

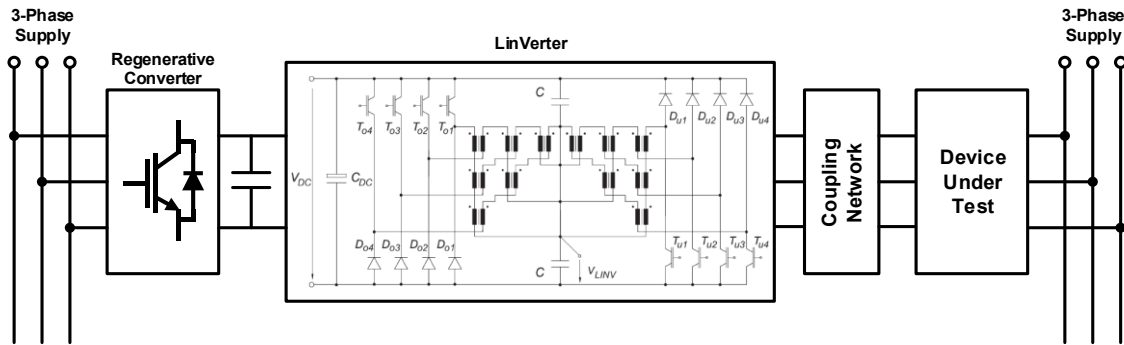


Fig. 1-3 Induction motor PHIL simulation using LinVerter [13].

A commercial power converter is used in [14] to emulate induction motors in order to test the performance of a high power level motor drive system. Slow semiconductor devices with low switching frequency of 3 kHz were utilized. A comprehensive analysis of the characteristics of two possible interface designs using the L and LCL coupling filters for the PHIL experiments is presented in [15].

Synchronous generator emulators are developed in [16] and [17] to investigate the performance of medium voltage micro-grids. Utility interfaced inverters are designed to improve load sharing performance with conventional synchronous generators. In [17], the impedance of the stator windings is represented by the converter output inductance and resistance. Therefore, the converter side voltage represents the back electromotive force (EMF) and the voltage across the converter output capacitor represents the terminal voltage of the synchronous generator. A digital signal processor (DSP) includes the model of the synchronous generator and all controller parts. The simulated stator currents are used as current references for the inverter operating in current control to mimic a real generator as shown in Fig. 1-4 [18].

A HTB-based grid emulator system consisting of a converter that emulates a synchronous generator is developed in [19]. The synchronous machine model is implemented to define the

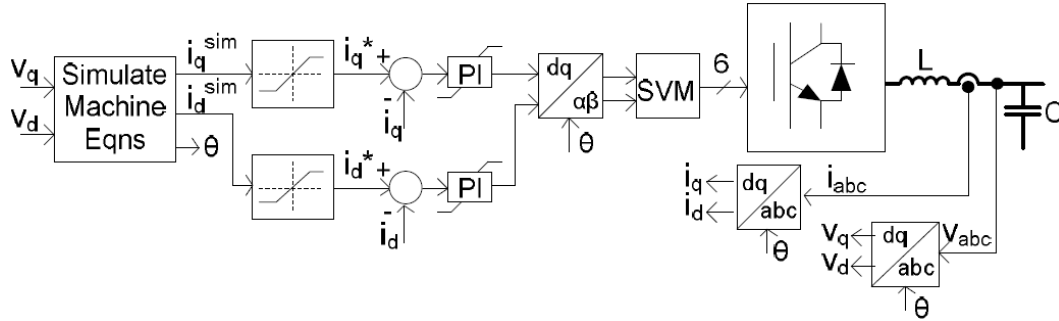


Fig. 1-4 Inverter control for emulation of a synchronous generator [18].

voltage references for the converter in the dq-axes. A voltage control loop with current differential feedback is used in order to minimize the controller output impedance (gain) and eliminate its influence on the generator model and to compensate for load disturbance on the output voltage.

A converter based HTB is used in [9] to emulate a two-area real power grid system. Two limitations that affect the accuracy of the HTB are addressed. First, the switching frequency limits the ability to emulate fast electromagnetic phenomena such as switching transients and traveling wave features. Second, the losses of the inductors that emulate transmission lines cannot be controlled. In [20], a power converter is controlled in rectifier mode in order to emulate a three-phase diode rectifier load to be used in a HTB-based grid transmission network emulator.

In [21], parallel power converters are connected to the grid via an active rectifier to emulate the dynamics of interconnected loads i.e. synchronous generator, induction motor, and constant impedance, current and power (ZIP) load within a wide-area transmission network. The mathematical model for each load is implemented inside the control algorithm of its specific converter. The combined system simulation of regenerative power among generation emulators and different types of loads is capable of normal operation with some fluctuations on the emulated grid voltage. The required power is shared and circulated inside the whole network system for regenerative purposes. Reconfigurable power grid emulators are used in [22] and [23] to emulate both ZIP and three-phase induction motor loads. The trapezoidal numerical method shows an improvement in the induction motor's emulation performance, while other numerical techniques exhibit incorrect output characteristics.

A power HIL application for high power drives at the megawatt level is implemented in [24]. A commercial variable speed drive is connected to a virtual power system through a

megawatt-scale variable voltage source for integrating the drive with the simulated power system. Certain challenges with the accuracy of power HIL interface are investigated. In other words, the need for a high precision interface amplifier is challenging due to the time delay, nonlinearities, and sensor noise in the amplified signal which results in significant simulation errors.

A back-to-back voltage source converter is used in [25] in order to emulate an ac transmission line connecting two-area grid networks. Two approaches in the phasor domain and discrete time domain models are used in order to study the transient features of the ac line. The developed control techniques show less dependency on frequency, and hence allowed high capabilities for emulation of AC transmission line flow dynamics.

A state-space control design method is proposed in [26] and [27] by using the linear quadratic regulator (LQR) optimization. This design was implemented in a digital platform. Experimental validation includes induction motor emulation, unbalanced three phase loads, and non-linear rectifier load emulation have been demonstrated. However, current tracking is inaccurate, with unwanted high order harmonics being introduced into the line currents. Also, the calculated motor torque has significant oscillations.

Due to continuous growth in power demand and the need for clean energy, renewable energy sources and related topics have recently attracted more attention. Physical emulators have been designed to test the interactions between wind turbines and the power grid in real-time [28] - [30]. The developed wind turbine emulators require a torque controlled motor to represent the wind torque and turbine inertia, and other systems to serve as the wind turbine generator. In [31], the emulation of a full-converter wind turbine based on a permanent magnet synchronous generator using a single converter is developed. The emulator is used to analyze machine behavior and system impact, and to verify the feasibility of emulating renewables within a HTB power grid emulation system. The emulating converter measures the grid voltage and generates the current reference signals.

A two-stage (DC-DC-AC) photovoltaic (PV) system emulation is implemented in [32] by using a single power inverter in a HTB-based power grid. In the model, the boost converter model achieves the maximum power point tracking (MPPT) or controls the DC link voltage in the reserved power mode. The inverter realizes DC link voltage control in the MPPT mode or active/reactive power control in the reserved power mode. The inverter-filter terminal voltage

and current measurements are used as model inputs while the generated model current is used as the current reference to be achieved by the inverter. Simulation results of the PV inverter show faster dynamics compared to the PV emulator in MPPT operating mode and under irradiance step change. Moreover, while validating the emulator operation, the MPPT control period was set to a very short time period, with very high frequency, which is unrealistic. Similar work is done in [33], which provides control and emulating methodologies for wind generators and PV by using small-scale voltage source converters which are rated at tens of kW.

A brief review of the works mentioned above and achieved in implementing induction motor emulators, their control topologies, and some concerns are given in Table 1-1.

Table 1-1 Summary of induction motor emulation in the literature.

Case Study	Item	Virtual induction machine power rating/reference frame	Current controller reference frame	Switching frequency	Coupling network	Concerns	Publishing year
H. J. Slater <i>et al.</i> [12]		4 kW dq-stationary reference frame	PI-based natural-abc	13 kHz	L	- Studies only motor running at steady state. - Saturation effect is ignored.	May 1998
M. Armstrong <i>et al.</i> [14]		56 kW dq-stationary reference frame	PI-based natural-abc	6 kHz	L	- High power levels with limited power electronic device switching frequency. - Saturation effect is ignored. - Inaccurate current tracking. - Distorted emulator currents.	Sep. 2005
Y. S. Rao and M. Chandorkar [26]		3 kW dq-stationary reference frame	PI-based natural-abc	10 kHz	LCL	- High oscillations in calculated torque. - Using six current transducers (grid and emulator currents). - Saturation effect is ignored.	Apr. 2010
S. Grubic <i>et al.</i> [13]		dq-model	PI-based natural-abc	12 kHz	LC	- Structure complexity. - A large number of devices and common-mode chokes. - Cost - Saturation effect is ignored.	Apr. 2010
O. Vodyakho <i>et al.</i> [10]		25 kVA dq-synchronously rotating reference frame	PI-based dq coordinates	5 kHz	LCL	- Increasing the number of coupling network will increase the complexity of the control. - Saturation effect is ignored.	Mar. 2012
J. Wang <i>et al.</i> [22]		10 kW dq-synchronously rotating reference frame	PI-based dq coordinates	10 kHz	L	- Different transients between the model and emulator. - Saturation effect is ignored.	Apr. 2016

To date, the literature available focuses mainly on emulating different types of static and dynamic loads as well as studying different network coupling methodologies, control

techniques, and emulating higher power rating loads. All are within a built-in reconfigurable power network HIL test bed. Individual emulators have the advantage of being independently controllable, representing real physical electrical machines and their applications. The literature lacks studies on induction machine emulators running as generators, specifically in one of the innovative renewable energy fields as wind generation systems.

1.7 Thesis Outline

This thesis is organized as follows:

Chapter 1 defines the context for this research by stating the problem, motivation, and objectives of this work. Some technical limitations are reported. Furthermore, this chapter reviews previous and most recent related publications and available applications of electrical machines emulation. It discusses different examples of load emulators, scaled physical components based mini-grids, real-time simulation/emulation platforms, and dynamic and static load emulators. Some examples in the field of renewable energy e.g. PV and wind turbine emulators are also discussed. Contributions of this study are then presented.

Chapter 2 discusses the dynamic model of the induction machine based on the dq-frame equivalent circuits. The mathematical model is expressed by a set of first-order differential equations while the stationary circuit variables are referred to the synchronously rotating reference frame. Experimental procedures are also discussed to estimate different parameters of the induction machine based on IEEE Std-112TM. The reactance parameters are expressed by current-dependent functions in order to include the saturation effect in both the main and leakage flux paths. In this chapter, machine models that consider or neglect the main and leakage flux saturation are compared with experimental results.

Chapter 3 introduces a direct and precise method to estimate and separate the stator and rotor leakage reactance parameters under normal operating conditions and when the core is deeply saturated. The method exploits the 2D time-stepping finite element method with a coupled circuit. This chapter also discusses the relationship between the stator and rotor leakage reactance of the induction machine which is assumed by IEEE Std-112TM to be constant under all operating conditions. However, this assumption is not substantially accurate during severe transients such as the direct online startup and loading conditions of a three-phase induction

motor. Moreover, the impact of the stator/rotor leakage split ratio, estimated by the proposed method on the dynamic performance of the induction machine is also discussed in this chapter. The predicted results are compared to the dynamic responses obtained experimentally from a three-phase, 5-hp squirrel-cage induction motor.

Chapter 4 presents an induction motor emulation based on a power electronic converter. The machine model which includes the main and leakage flux saturation is used in the developed emulation system. Moreover, the proportional-resonant current controller in the abc-frame is discussed and used. Both the machine model and control scheme are implemented on the real-time simulator to control the emulating converter. This chapter presents the experimental results which show the effectiveness of using the developed emulator to resemble accurately an actual induction motor running at different operating conditions.

Chapter 5 describes the development of a power electronic converter-based self-excited induction generator emulator to replace a wind- or microhydro-turbine driven squirrel-cage induction generator that works within an isolated power system to feed power in remote areas. This chapter presents the dq-modeling of the three-phase self-excited induction generator with modified parameters while the stationary circuit variables are referred to a reference frame fixed in the rotor. It discusses the design of the cascaded voltage and current control loops which utilize the proportional-integral type in the dq-frame. Furthermore, the chapter investigates the use of the voltage-type ideal transformer model as a power interface for the emulator whereas an excitation capacitance is added to the power-hardware-in-the-loop block diagram. Likewise, the dynamic responses of the induction generator emulator and real generator recorded during different operating conditions are compared and discussed in this part of the thesis. The results validate the effectiveness of using the developed emulator to resemble closely a real generator.

Chapter 6 presents the conclusions and future works.

1.8 Thesis Contributions

The technical contributions achieved in this Ph.D. work are as follows:

1.8.1 Journal papers

Mohammad A. Masadeh, K. S. Amitkumar and Pragasen Pillay, "Power electronic converter-based induction motor emulator including main and leakage flux saturation," in *IEEE Transactions on Transportation Electrification*, vol. 4, no. 2, pp. 483-493, Jun. 2018. (DOI: 10.1109/TTE.2018.2824619)

Mohammad A. Masadeh and Pragasen Pillay, "Induction generator emulator for isolated renewable energy power system," submitted for publication to *IEEE Transactions on Industrial Electronics*, Oct. 2018 (under revision).

Mohammad A. Masadeh and Pragasen Pillay, "Impact of the stator/rotor leakage split ratio on induction machine performance," submitted for publication to *IEEE Transactions on Industrial Electronics*, Oct. 2018.

Not related topic:

Mohammad A. Masadeh, Kiran Kuruvinashetti, Mehdi Shahparnia, Pragasen Pillay, and Muthukumaran Packirisamy, "Electrochemical Modeling and Equivalent Circuit Representation of a Microphotosynthetic Power Cell," in *IEEE Transactions on Industrial Electronics*, vol. 64, no. 2, pp. 1561-1571, Feb. 2017. (DOI: 10.1109/TIE.2016.2618755)

1.8.2 Conference papers

Mohammad A. Masadeh and Pragasen Pillay, "Induction motor emulation including main and leakage flux saturation effects," in *IEEE International Conference on Power Electronics, Drives, and Energy Systems (PEDES)*, Trivandrum, India, Dec. 2016.

(DOI: 10.1109/PEDES.2016.7914307)

Mohammad A. Masadeh and Pragasen Pillay, "Power electronic converter-based three-phase induction motor emulator," in *IEEE International Electric Machines and Drives Conference (IEMDC)*, Miami, FL, USA, May 2017.

(DOI: 10.1109/IEMDC.2017.8002207)

Chapter 2. Induction Machine Model with Modified Parameters

2.1 Introduction

In this chapter, the mathematical modeling of the electrical and mechanical parts of the three-phase induction machine (IM) based on the dq-frame in the synchronous reference is presented. The machine model is simulated in Matlab/Simulink[®] using parameters measured based on IEEE Std. 112TM [34] and IEC 60034-1 [35] for a three-phase, 5-hp, squirrel-cage induction machine and results are compared with output characteristics of a real machine.

2.2 Induction Machine Dynamic Model

To study the behavior of a three-phase induction machine, its dynamic model can be derived from the two-phase machine theory. In the dq-model, two stator windings (q_s and d_s) replace the three-phase stator coils (a_s , b_s , and c_s), while another two rotor windings (q_r and d_r) replace the three-phase rotor coils (a_r , b_r , and c_r) as shown in Fig. 2-1 [5].

The subscript (s) denotes variables and parameters associated with the stator circuits, and the subscript (r) denotes variables and parameters associated with the rotor circuit. The assumption made for deriving the equations is that the core losses (eddy current and hysteresis) are negligible.

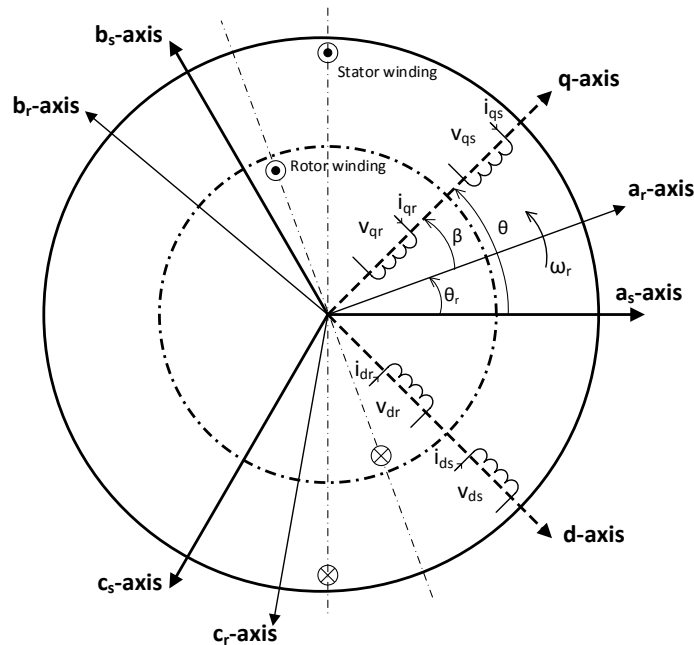


Fig. 2-1 Three-phase induction machine windings distribution in abc and dq axes [5].

The abc-model variables f_{abc} should be transformed into the dq-model variables f_{dq0} with an arbitrary angle value θ and angular speed $\omega = \frac{d\theta}{dt}$ using Park's transform as given in the Appendix - A.

2.3 Conventional Induction Machine Model

To study the behavior of the three-phase induction motor, its dynamic model is derived from the well-known dq-coordinate equivalent circuits shown in Fig. 2-2 in the arbitrary reference frame [22]. The mathematical modeling of the three-phase IM in the synchronously rotating reference frame is given in (2-1) - (2-12). They are expressed as first-order differential equations to represent machine dynamics.

$$v_{ds} = R_s i_{ds} + \frac{d\lambda_{ds}}{dt} - \omega_s \lambda_{qs} \quad (2-1)$$

$$v_{qs} = R_s i_{qs} + \frac{d\lambda_{qs}}{dt} + \omega_s \lambda_{ds} \quad (2-2)$$

$$v_{dr} = R_r i_{dr} + \frac{d\lambda_{dr}}{dt} - (\omega_s - \omega_r) \lambda_{qr} \quad (2-3)$$

$$v_{qr} = R_r i_{qr} + \frac{d\lambda_{qr}}{dt} + (\omega_s - \omega_r) \lambda_{dr} \quad (2-4)$$

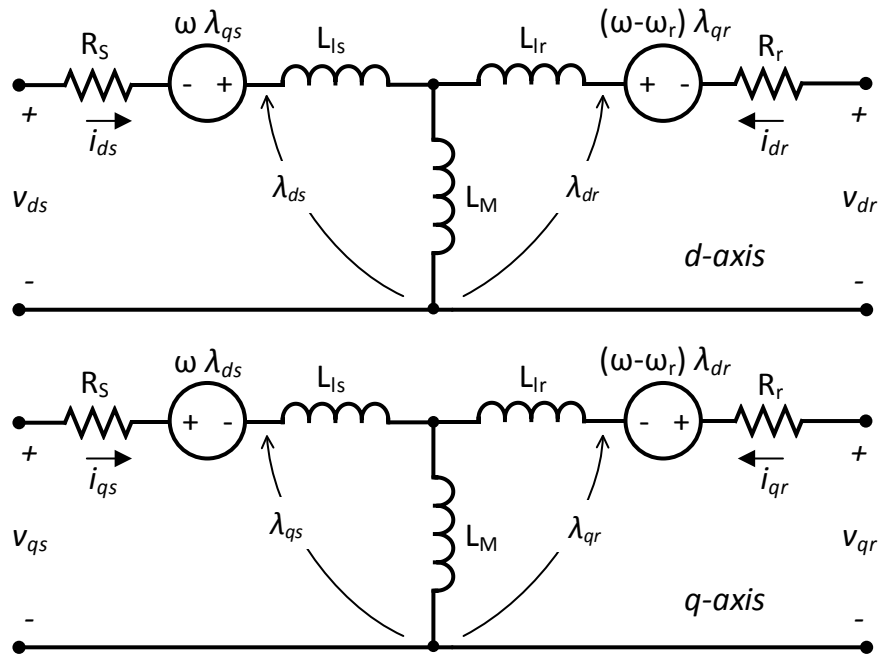


Fig. 2-2 dq-equivalent circuit for a three-phase induction machine (0-axis is neglected) [4].

The flux linkage equations, which relate the stator and rotor flux linkages with the stator and rotor currents, are:

$$\lambda_{ds} = L_{ls}i_{ds} + L_M(i_{ds} + i_{dr}) \quad (2-5)$$

$$\lambda_{qs} = L_{ls}i_{qs} + L_M(i_{qs} + i_{qr}) \quad (2-6)$$

$$\lambda_{dr} = L_{lr}i_{dr} + L_M(i_{ds} + i_{dr}) \quad (2-7)$$

$$\lambda_{qr} = L_{lr}i_{qr} + L_M(i_{qs} + i_{qr}) \quad (2-8)$$

where v_{ds} and v_{qs} are the stator terminal voltages in the d- and q-frame, respectively; v_{dr} and v_{qr} are the rotor terminal voltages in the d- and q-frame, respectively which go to zero in the case of the squirrel-cage machine; i_{ds} and i_{qs} are the stator currents in the d- and q-frame, respectively; i_{dr} and i_{qr} are the rotor currents in the d- and q-frame, respectively; λ_{ds} and λ_{qs} are the stator flux linkages in the d- and q-frame, respectively; λ_{dr} and λ_{qr} are the rotor flux linkages in the d- and q-frame; and R_s and R_r are the stator and rotor resistances, respectively. ω_s is the electrical angular frequency of the synchronously rotating reference frame; ω_r is the electrical angular frequency of the rotor; L_{ls} and L_{lr} are the leakage inductances of the stator and rotor, respectively; and L_M is the mutual or magnetizing inductance. These inductances are denoted by their respective reactance values given as $X = \omega_s L$.

The electromechanical behavior of the induction machine is expressed by (2-9):

$$J_m \frac{d\omega_m}{dt} = T_e - T_L - B_m \omega_m, \quad (2-9)$$

where T_L is the load torque, J_m is the moment of inertia of the machine, B_m is the friction coefficient, and ω_m is the mechanical angular speed of the machine $\omega_m = \frac{2}{p} \omega_r$. T_e is the electromagnetic torque produced by the induction machine which can be expressed either in terms of the stator current and the stator flux or rotor current and the rotor flux as follows:

$$T_e = \frac{3}{2} \frac{P}{2} (\lambda_{ds} i_{qs} - \lambda_{qs} i_{ds}), \quad (2-10)$$

$$= \frac{3}{2} \frac{P}{2} (\lambda_{qr} i_{dr} - \lambda_{dr} i_{qr}), \quad (2-11)$$

This expression yields the torque expressed in terms of currents as:

$$T_e = \frac{3}{2} \frac{P}{2} L_M (i_{qs} i_{dr} - i_{ds} i_{qr}) \quad (2-12)$$

where P is the number of poles in the machine.

2.4 Induction Machine Model Including Flux Saturation Effect

During normal steady-state operation, the flux paths in the stator, air-gap, and rotor circuitry are operated under rated conditions, in which the stator, rotor, and main inductances are considered constant. However, the electromagnetic parameters of an IM can vary widely during different kinds of severe transients such as direct online starting, loading, and faults, which results in flux saturation in different parts of the machine. Hence, different machine behaviors other than the ones predicted by computer simulation may occur [36].

In fact, the large inrush currents that flow in the machine during starting results in larger values of slot leakage flux in both stator and rotor slots, which saturate the machine's teeth; hence, the leakage inductances that are normally considered constant in the conventional model become functionally dependent on machine currents [36]. To have an emulator that resembles closely a real induction motor, the inclusion of new terms representing the main flux as well as the stator and rotor leakage flux saturation is considered in this work.

Since the 1980s, many works were achieved to analytically model the saturation effect in the IM in either the stator and rotor leakage flux paths [36] or in the main flux path [37]. Moreover, recent works are also available in [38], which considers only the leakage saturation based on analytical methods. On the other hand, experimental methods are utilized in [39] to incorporate the magnetic saturation in the main flux path for the wound-rotor IM, and in [40], [41], and [42] to compensate for both the main and leakage flux paths.

Assumptions to include the saturation effects in the emulator model can be summarized as follows:

- The motor is well-ventilated and running under constant temperature. Hence, resistances R_s and R_r of the motor windings are considered constant.
- The three-phase input voltage is symmetrical and balanced. The fundamental frequency of 60 Hz is only considered. Higher frequency impacts on the reactance are not modeled.

In this chapter, the 5-hp IM is considered as the machine-under-test due to the availability of its design specifications. The standard tests; the blocked-rotor and no-load tests were employed to obtain the electrical parameters of the machines. Moreover, the run-down test was run to obtain the mechanical parameters. All linear parameters, in which the saturation is not considered, are given in Table 2-1.

Table 2-1 IM measured parameters based on IEEE Std-112™ and specifications at rated conditions.

Three-phase, 5-hp, 4-pole, 220 V, 16 A, 60 Hz, 1730 rpm, Δ -connected Squirrel-cage induction machine	
Parameter	Value
Stator resistance R_s	0.9649 Ω
Rotor resistance R_r	1.3046 Ω
Magnetizing reactance X_M	76.5378 Ω
Stator leakage reactance X_{ls}	1.8990 Ω
Rotor leakage reactance X_{lr}	4.4164 Ω
Moment of inertia J_m	0.0138 Kg.m ²
Friction coefficient B_m	0.0021

2.4.1 Magnetizing reactance calculation

The model of the IM considering the main flux saturation is developed by replacing the unsaturated magnetizing inductance L_M or reactance X_M in (2-1) - (2-12) by its corresponding saturation function.

In order to obtain the saturation characteristics in the main flux path of the squirrel-cage induction motor, the no-load motor test is carried out. The applied voltage ranging from 125% of the rated voltage down to a point, at which further voltage reduction increases the current [34]. The experimental measurements of the applied line voltage and measured currents per phase for the 5-hp machine are given in Fig. 2-3. The plotted graph represents the magnetization curve for this machine. It describes the unsaturated or the linear part when the voltage varies from minimum to the rated voltage. Thereafter, the machine starts to saturate, in which a very small variation in the applied voltage leads to a large change in the drawn current.

For the no-load test, since $X_{ls} \ll X_M$, the stator leakage reactance can be ignored. Hence, the magnetizing reactance can be determined based on measured values as follows:

$$X_M = \omega_s L_M = \text{Imag} \left(\frac{V_\phi}{I_\phi} \right), \quad (2-13)$$

where V_ϕ is the applied phase voltage and I_ϕ is the measured current per phase.

Therefore, the magnetizing reactance has been calculated based on the measured values and then plotted as shown in Fig. 2-3. The figure shows the reduction in the magnetizing reactance at high current values. The function which signifies the variation of the magnetizing reactance under saturation for this machine with the amplitude of the magnetizing current is given by:

$$X_{M \text{ sat}}(I_m) = k_1 e^{-c_1 I_m} - k_2 e^{-c_2 I_m}, \quad (2-14)$$

where k_1 , k_2 , c_1 , and c_2 are the magnetizing reactance saturation parameters. For the sake of avoiding repetition of the function, these parameters are tabulated and given in Table C-3 in Appendix - C. While implementing the saturation model, the magnetizing reactance $X_{M \text{ sat}}$ is updated during each calculation iteration of I_m . The magnetizing current I_m is calculated in the dq-frame as follows:

$$I_m = \sqrt{(i_{qs} + i_{qr})^2 + (i_{ds} + i_{dr})^2}. \quad (2-15)$$

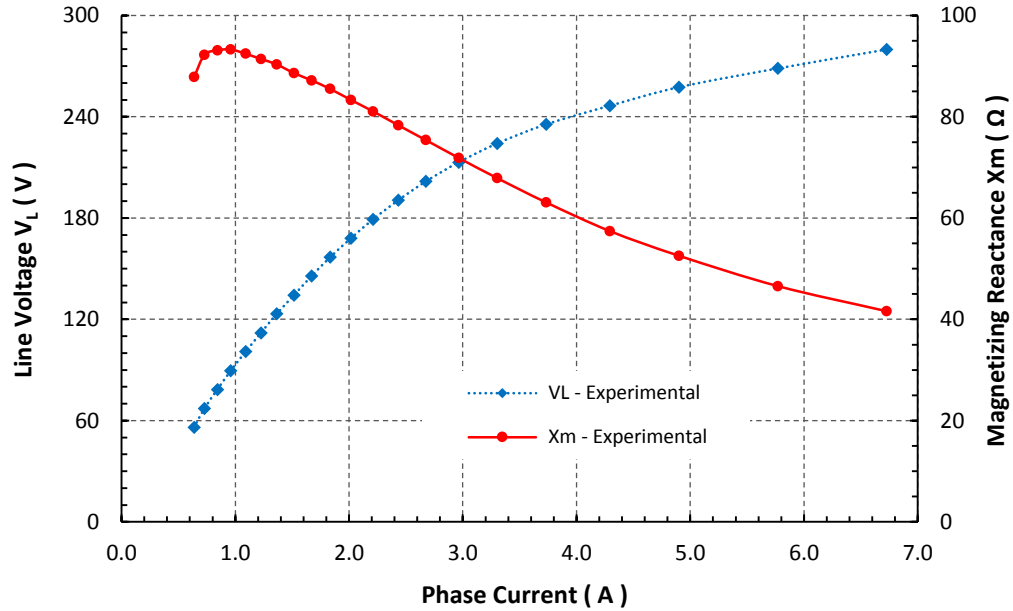


Fig. 2-3 No-load measured magnetization curve for the 5-hp machine and the corresponding main reactance.

2.4.2 Stator and rotor leakage reactance calculation

For different transient conditions, the high inrush current flowing into the stator and rotor windings induces the leakage inductances to saturate. The stator and rotor leakage reactance values have a significant impact on the motor's behavior. This effect should be taken into account in the machine model.

Experimental estimation of the IM leakage reactance is considered challenging [42]. The locked-rotor test only allows the determination of the sum of both the stator and rotor reactance values. Hence, it is hard to conclude the degree of the saturation affecting each reactance. For simplicity, the leakage saturation reactance characteristics are determined based on two methods. First, rapid test measurements at 120% of the rated current down to the lowest possible current according to IEC 60034-1 [35] and machine datasheet have been implemented and recorded. Moreover, a motor startup at reduced voltages to obtain the inrush currents is implemented. Hence, 100%, 75%, and 50% of rated voltage are applied and the corresponding currents are recorded.

Fig. 2-4(a) shows the experimental measurements of the applied line voltages and phase currents for the 5-hp machine. The total leakage reactance has been calculated using (2-16), plotted and curve fitted. The figure describes the machine at high starting currents, while the corresponding total reactance values are significantly reduced at the flux saturation condition.

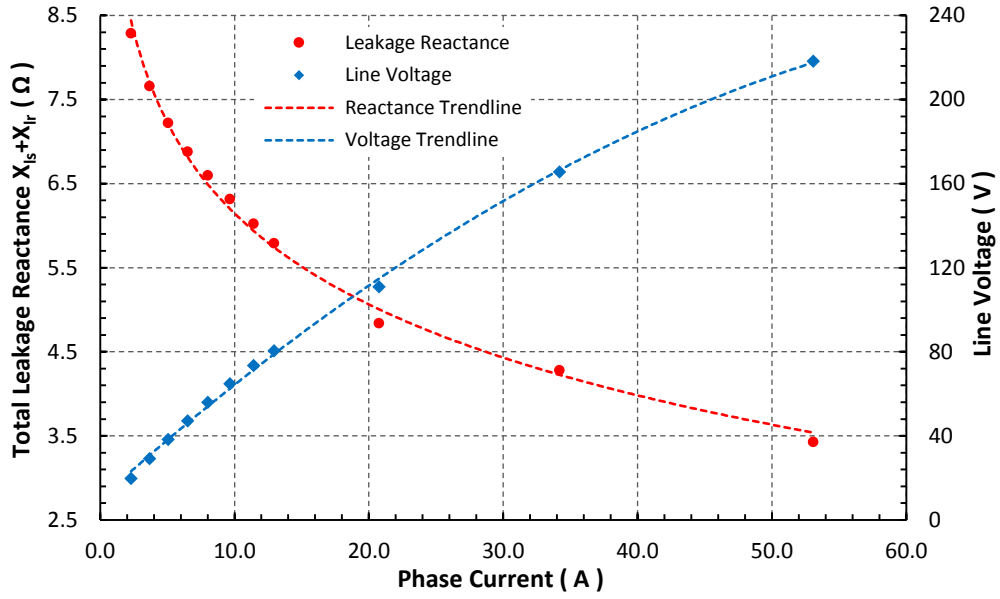
$$X_{ls} + X_{lr} = \sqrt{Z^2 - (R_s + R_r)^2}, \quad Z = \frac{V_\phi}{I_\phi}. \quad (2-16)$$

Since the design of the machine is known as Design C motor, the relationship between the stator and rotor leakage reactance is given by $X_{ls} = 0.43X_{lr}$ [34]. The variation of the stator and rotor leakage reactance values function of the drawn current for both machines are demonstrated in Fig. 2-4(b). The curve fit functions of the stator and rotor leakage reactance under saturation are given by:

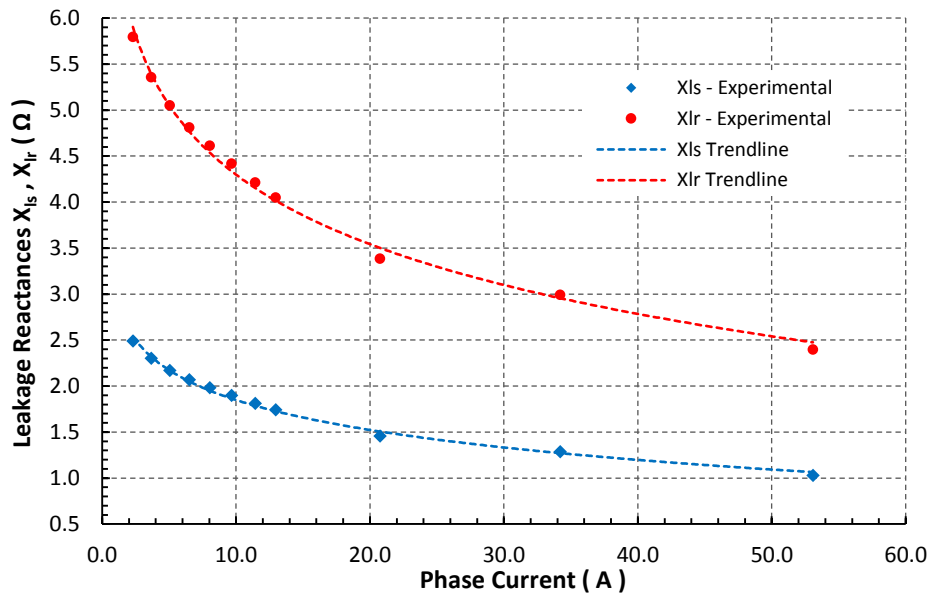
$$X_{ls\ sat}(I_s) = k_{30}e^{-c_{30}I_s} - k_{40}e^{-c_{40}I_s} \quad (2-17)$$

$$X_{lr\ sat}(I_r) = k_{50}e^{-c_{30}I_r} - k_{60}e^{-c_{40}I_r} \quad (2-18)$$

where k_{30} to k_{60} , c_{30} and c_{40} are the initial leakage reactance saturation parameters, they are



(a)



(b)

Fig. 2-4 Leakage reactance measurements for the 5-hp machine.

listed in Table C-3 in Appendix - C. They are updated during each calculation iteration of I_s and I_r . These currents represent the amplitude values of the stator and rotor currents, respectively. They are calculated and implemented in the dq-frame as follows:

$$I_s = \sqrt{(i_{qs} + i_{ds})^2} \quad \text{and} \quad I_r = \sqrt{(i_{qr} + i_{dr})^2}. \quad (2-19)$$

2.5 Experimental and Simulation Results

The saturation model derived in the Section 2.4 was implemented in the machine model (2-1)-(2-12). To prove the effectiveness of using the IM model with modified parameters, an experimental direct online startup was employed. The test results were compared with the motor model while neglecting the flux saturation effect and linear parameters were used and when the saturation effect in both main and leakage flux paths are considered in the machine model.

Fig. 2-5 and Fig. 2-6 show the detailed startup responses of the real 5-hp induction motor at rated voltage with no-load. They show a comparison between the experimental and predicted dynamics when the saturation effect in both paths are ignored and when they are included in the machine model. Fig. 2-5 demonstrates the predicted line current compared to the measured one. Fig. 2-5(a) reveals the differences in the peak values (overshoots) while no significant difference is noticed when the motor reaches its steady-state. The difference in peak values between the predicted and experimental responses has been reduced when the flux saturation effect in both flux paths is considered in the machine model as revealed in Fig. 2-5(b). Moreover, Fig. 2-6(a) shows the predicted speed response of the IM when the saturation effect is ignored and the fixed measured IM parameters are only used. It is compared to the measured speed response. The

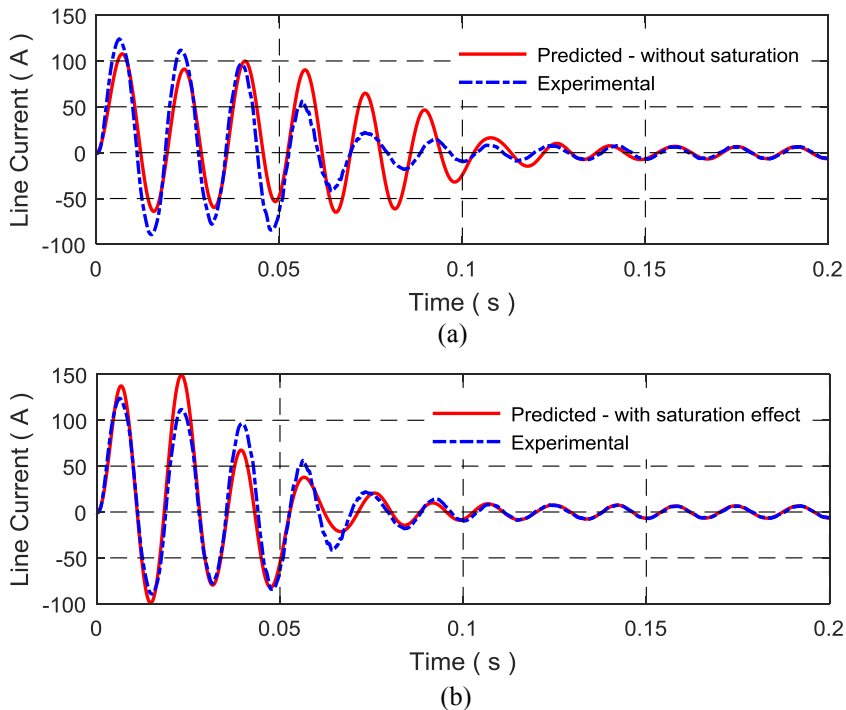


Fig. 2-5 Predicted line current response during DOL startup of the 5-hp IM at rated voltage compared to the measured current response. (a) Model without saturation. (b) Model with saturation.

figure shows the difference between the two responses, especially in the transient condition. However, this difference is decreased by including the saturation effect in the machine model as shown in Fig. 2-6(b). This proves that the leakage and magnetizing reactances should not be considered fixed and their variations should be included in the machine model.

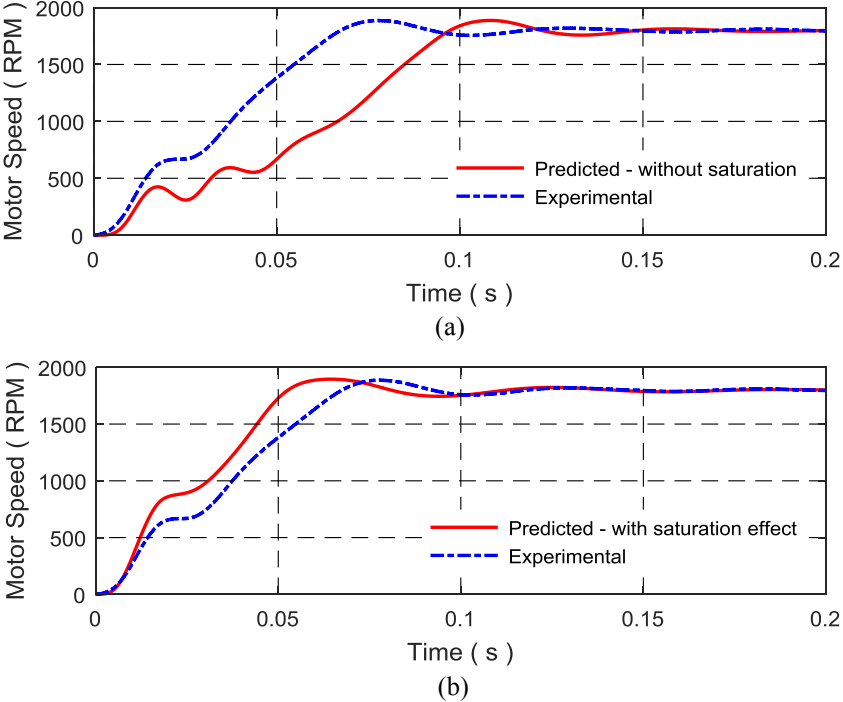


Fig. 2-6 Predicted speed response during DOL startup of the 5-hp IM at rated voltage compared to the measured speed response. (a) Model without saturation. (b) Model with saturation.

2.6 Summary

In this chapter, experimental test procedures in accordance with IEEE Std-112™ and IEC 60034-1 are implemented in order to obtain the leakage and magnetizing reactance saturation characteristics of the mathematical model for the 5-hp IM. This helps to predict closely the performance of the machine during severe transients as well as steady-state condition. The stator and rotor leakage reactance parameters are calculated and separated based on a constant ratio defined by IEEE Std-112™ and the machine specifications. Other linear parameters of the machine are also determined at rated conditions. The derived current-dependent reactance parameters are then included in the dq-model of the IM. Machine models that consider or neglect the main and leakage flux saturation are compared with experimental results. The model which considers the magnetic saturation effect in both flux paths results in more acceptable transient responses.

Chapter 3. Impact of the Stator/Rotor Leakage Split Ratio on Induction Machine Performance

3.1 Introduction

The behavior of the induction machine (IM) can be predicted from its well-known electrical equivalent circuit. However, this is not enough accurate because it assumes the linearity of the core and its parameters are derived from analytical methods with many simplifying assumptions. Some attempts of introducing nonlinear inductances have been done. With linear parameters, significant errors may occur when analyzing the machine performance. Machine parameters with high electric current transients such as the direct online startup are different from the parameters at rated or no-load current values. Therefore, machine behavior may also differ.

IM equivalent circuit parameters are calculated according to different testing methods proposed by IEEE Std 112™ [34]. The total leakage reactance of the machine is determined by using the locked rotor test. Besides, the stator and rotor leakage reactance parameters are calculated and separated according to a constant splitting ratio assumed by [34] at all operating conditions. In fact, the reactance in both the stator and rotor flux paths are widely varying during severe transients [36]. Hence, in order to have a close prediction of the dynamic performance of the machine, the leakage reactance in both paths should be determined and separated according to the machine current and the ratio between them is no longer constant at all electric current values.

With the development of numerical modeling tools, the finite element method (FEM) can be used to precisely predict the performance of an electromagnetic device. Although the field distribution within the machine is three-dimensional, the two-dimensional (2D) field solution can still be highly-accurate in calculating the steady-state (SS) as well as the dynamic performance of electrical machines. Analytically calculated leakage reactance values are sometimes higher than those obtained by the FEM [43]. This can be attributed to the fact that analytical solutions use machine parameters around rated magnetic specification of the core. In other words, they do not take into consideration the effect of saturation of leakage flux paths in the iron.

Induction machine parameter estimation based on complex space vectors of currents and flux linkages is proposed in [44]. It is used to predict the total leakage and magnetizing

inductances based on time-harmonic FE simulations. A 2D nonlinear time-harmonic analysis is used in [45] to extract the induction motor parameters from FE solutions. The leakage reactance was decomposed into the slot, end-winding, harmonic, and skew terms. The frozen permeability method is used in the static magnetic field simulation to separate the leakage reactance terms. However, some parameters are calculated analytically. A novel equivalent circuit for induction motors is proposed in [46]. It includes the stray load loss and harmonic torques that are determined from the FE simulation. The magnetizing and leakage reactance values are calculated from the stator and rotor flux linkages that are produced by their respective currents as a function of the slip frequency.

Experimental procedures are addressed in [39] to obtain the parameters of a dynamic model of the synchronous machine with a saturation effect. The stator leakage inductance is extracted from the frequency response utilizing genetic algorithms to solve the nonlinear optimization problem. A procedure to estimate the stator leakage inductance at steady-state conditions for a nine-phase synchronous machine is discussed in [47]. The methodology is based on a combination of FEM and on measurements taken during no-load and short-circuit tests to identify the magnetizing inductance and only the stator leakage inductance. A test method to characterize experimentally the dq-model of the induction machine based on impedance measurements at steady-state is also proposed in [48].

This chapter presents a direct and precise method to calculate the stator leakage reactance of a three-phase, squirrel-cage induction motor under a wide range of stator current values. It is implemented in a 2D-FEM by feeding the stator coils from a three-phase variable voltage source while the rotor space is replaced by a very low permeability material μ_r of 10^{-6} , the drawn stator currents are recorded. Then, the locked rotor test with current sources in the FEM is performed to estimate the total leakage reactance of the machine at different stator currents. The rotor leakage reactance is then separated under normal operating conditions and when the machine core is deeply saturated. The other machine parameters are determined by applying the conventional tests; no-load and locked rotor tests in FEM with motion analysis [49].

3.2 Finite Element Model with Coupled Circuit

The equations that define the electromagnetic field diffusion are given by Maxwell's equations as follows [50]:

$$\left. \begin{aligned} \nabla \times \vec{H} &= \vec{J} \\ \nabla \times \vec{A} &= \vec{B} \\ \vec{B} &= \mu \cdot \vec{H} \end{aligned} \right\}, \quad (3-1)$$

and

$$\nabla \times \left(\frac{1}{\mu} \cdot \nabla \times \vec{A} \right) = \vec{J}, \quad (3-2)$$

where H is the magnetic field intensity and B is the flux density, A symbolizes the magnetic vector potential (MVP), and μ is the magnetic permeability of the material. The current density J represents the sum of three main components; the current density due to the applied source, another due to the induced electric field produced by the time-varying magnetic flux and the third component is due to the rotor motion. However, when a moving reference frame is defined, the relative velocity of the moving element in this reference frame becomes zero [51]. By considering the source or the current density J directed in the z-axis and the field in the xy-plane, the 2D field equation which uses the Maxwell's equation (3-2) and represents the MVP in the z-direction is given by [52]:

$$\frac{\partial}{\partial x} \left(\frac{1}{\mu} \frac{\partial A_z}{\partial x} \right) + \frac{\partial}{\partial y} \left(\frac{1}{\mu} \frac{\partial A_z}{\partial y} \right) - \sigma \frac{\partial A_z}{\partial t} = -J_z, \quad (3-3)$$

where σ is the electrical conductivity of the conductors.

The external coupling circuit makes the numerical model flexible to the indirect tests e.g. no-load and locked rotor tests. A three-phase voltage source is used for field excitation. In order to calculate the current in the stator winding, the circuit equations are coupled with the field equation. Hence, the coupled stator circuit equation is given by:

$$V_s = R_s I_s + j\omega_s (\psi_{ls} + \psi_m), \quad (3-4)$$

where V_s is the stator phase voltage, R_s is the stator phase resistance, I_s is the stator phase current, ψ_{ls} is the stator leakage flux linkage, ψ_m is the flux linkage in the main path, and ω_s is the source angular frequency.

The electromagnetic circuit model of the squirrel-cage IM under study includes two main parts, first is the three-phase stator windings which are connected in delta (Δ) and fed from three sinusoidal AC voltage sources as shown in Fig. 3-1(a). In this figure, R_1 and L_1 represent the end-winding impedance per-phase of the stator winding. The second part is the rotor bars which are connected in parallel as shown in Fig. 3-1(b). Between every two neighboring rotor coils which are modeling the rotor bars, an impedance that short-circuiting two adjacent rotor bars where R_4 is the rotor bar resistance and the end-ring impedance is represented by R_{32} and L_4 . These parameters are given in Table C-1 in Appendix - C.

The stator and rotor leakage reactance values for the induction motor are calculated and separated by using the 2D, time-stepping, nonlinear analysis in FEM with the coupled circuit shown in Fig. 3-1 and defined in (3-4).

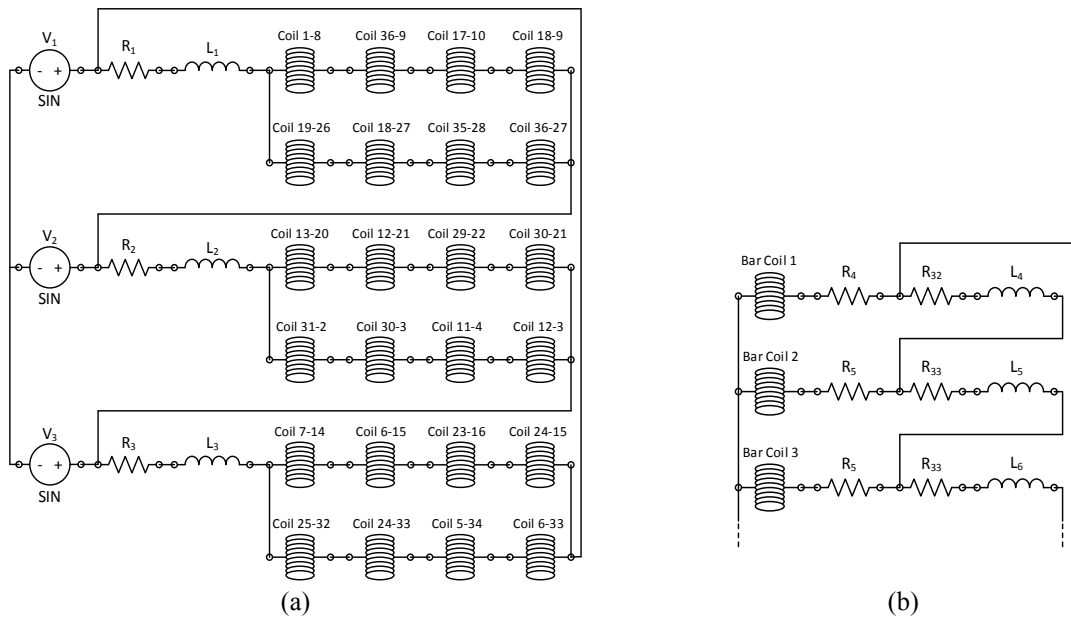


Fig. 3-1 Electromagnetic coupled circuit model in MagNet. (a) Stator circuit and (b) Part of the rotor circuit.

3.3 Stator Leakage Reactance Estimation

3.3.1 Method I: Calculation when the rotor is removed and replaced by air

According to IEC standard [53], the leakage reactance of the stator winding X_σ of the synchronous machine is measured with the rotor being removed and the air is occupying the rotor space. A search coil is placed inside the stator bore during measurement, detailed specifications of the search coil are available in [53]. A symmetrical three-phase voltage is then

applied to the stator windings and the voltage induced across the coil's terminals V_c is measured. In fact, this voltage is directly proportional to the flux available in the rotor's space. Thus, the resulted measured reactance X_b is the part due to the flux present in the space normally occupied by the rotor. This reactance is then subtracted from the total stator measured reactance of one phase X_a as in (3-5) since it is not considered as part of the leakage reactance.

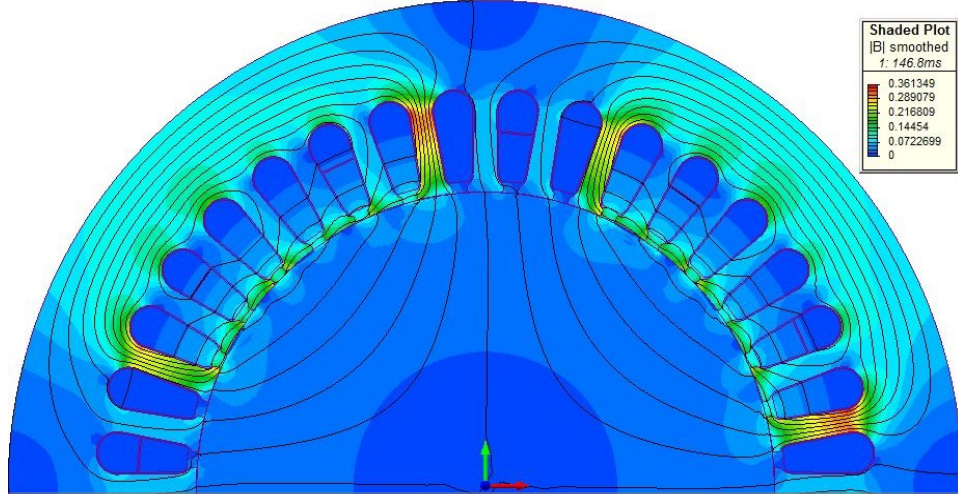
$$X_\sigma = X_a - X_b . \quad (3-5)$$

This technique is implemented in [54] in order to determine the total leakage reactance of the stator for a turbo-generator using the 2D numerical analysis with FE modeling. As well-known, the stator of IMs has a similar design as in the synchronous machines. Therefore, this method is used in this work as a benchmark for stator leakage reactance estimation at the rated current condition. Moreover, it is difficult to separate and measure the end-winding leakage field independently from the leakage field in the machine core [54]. Therefore, the comparison of the obtained results with the measured data is accomplished in terms of the total stator leakage reactance instead of considering the end-winding leakage reactance separately.

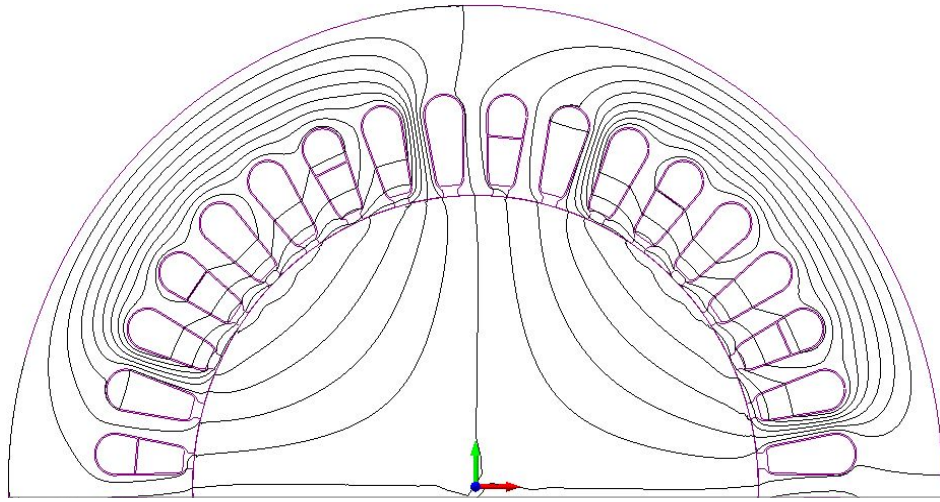
The IEC standard procedures stated earlier have been implemented in a 2D nonlinear analysis in FEM with the coupled circuit. The 5-hp squirrel-cage IM with the design specifications listed in Table C-1 in Appendix - C has been modeled in FEM while, the rotor core, bars, and shaft are removed and space is replaced by the air. The rotor circuit has also been removed from the FE-coupled circuit model. The flux distribution map and its lines in the stator part of the IM when the rotor is removed are shown in Fig. 3-2(a) and (b), respectively. The figure shows the flux in the rotor space which is not part of the leakage field. The part of the reactance X_a which characterizes the flux linkage in the machine core, given as X'_a , can be calculated by using the results obtained from the FEM as follows:

$$\begin{aligned} X'_a &= 2\pi f_s \frac{1}{n_p} \frac{\psi_a}{\left(\frac{I_a}{n_p}\right)} \\ &= 2\pi f_s \frac{\psi_a}{I_a} , \end{aligned} \quad (3-6)$$

where f_s is the source frequency, n_p is the number of parallel branches of the stator per phase, I_a is the total phase current and ψ_a is the total flux linkage in one phase. The later term is



(a)



(b)

Fig. 3-2 Magnetic flux distribution in the induction machine when the rotor is removed and space is replaced by air: (a) flux density map and (b) flux lines.

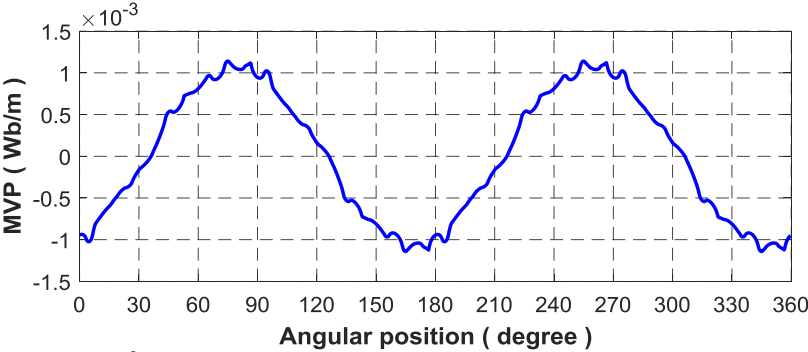
calculated as the sum of all flux linkages of all coils that are connected in series in one phase as given in (3-7). Moreover, the flux linkage of each individual coil is equal to the line integral of the MVP A_z along the contour of the same coil. In the 2D-FEM, this integral is directly proportional to the difference between the average magnetic vector potential in the meshed geometric regions employed by the coil sides placed in different pole regions. This flux linkage is calculated by using the following relationship [44]:

$$\begin{aligned} \psi_a &= \frac{P}{2} \sum_{c=1}^n \psi_c = \\ &= \frac{P}{2} \sum_{c=1}^n \frac{1}{S} \left(\int_{S_+} A_z dS - \int_{S_-} A_z dS \right) N_t l, \end{aligned} \quad (3-7)$$

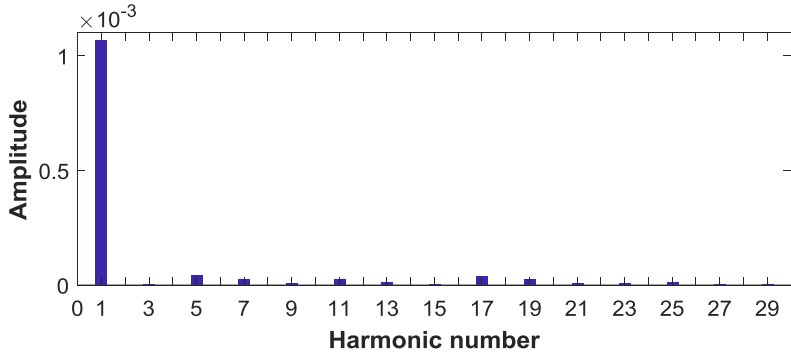
where n is the number of coils per phase in one pole side, ψ_c is the flux linkage for each individual coil in one phase, N_t is the number of turns of each individual coil and l is the stack length of the stator. S is the coil cross section area while S_+ is the total area over one side of the coils in one phase winding in one pole region and S_- is the total area over the other side of the same phase winding in another pole region.

Thus, the reactance X_a is then calculated as the sum of the reactance X'_a that is calculated in FEM as in (3-6) and the end-winding leakage reactance X_{end} . Since the main purpose of this work is to determine and separate the stator and rotor leakage reactance values, X_{end} parameter is determined using MotorSolve FEM [55] and listed in Table C-1 in Appendix - C.

To calculate the reactance X_b due to the flux created by the stator windings in the space which is normally occupied by the rotor, the required voltage V_c is determined by employing the magnetic vector potential distribution along the outer diameter of the rotor space concluded from the FEM which is shown in Fig. 3-3(a). The fast Fourier transform and the magnitude of its fundamental component is depicted in Fig. 3-3(b). Other high order harmonics with lower



(a)



(b)

Fig. 3-3 Magnetic vector potential: (a) Its distribution along the outer diameter of the rotor space and (b) spectrum analysis.

magnitudes are also revealed. The root-mean-square value of the produced V_c is given as follows:

$$V_c = 2\pi f_s \frac{1}{\sqrt{2}} (2 A_{z1} l), \quad (3-8)$$

where A_{z1} is the magnitude of the fundamental component of the MVP distribution along the outer diameter of the rotor space. With the estimated voltage V_c , the reactance X_b is then calculated as follows:

$$X_b = \frac{N k_w}{N_c} \frac{V_c}{I_a}, \quad (3-9)$$

where N is the number of series-connected turns per circuit of a phase of the stator winding, k_w is the stator winding factor, N_c is the number of search coil turns, and I_a is the stator current.

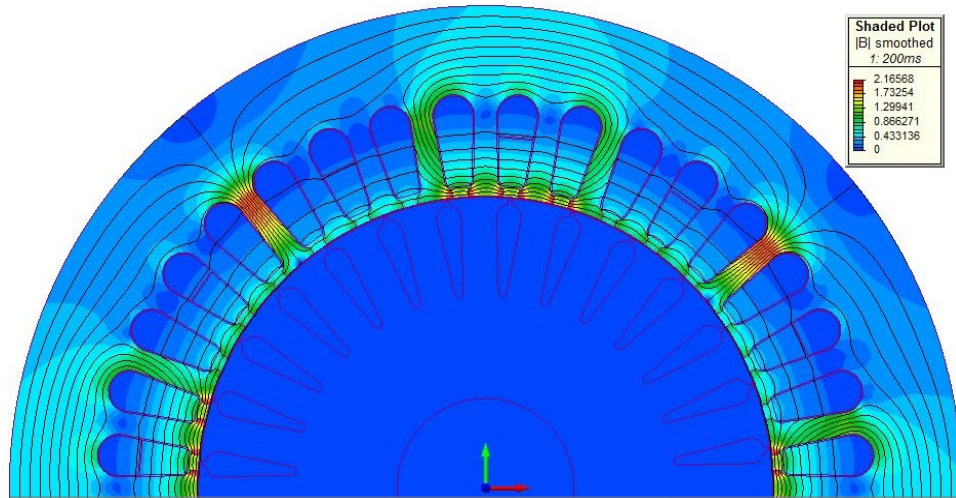
Hence, the stator leakage reactance of the induction machine is determined by subtracting the calculated X_b from X_a in FEM according to (3-5).

3.3.2 Method II – Proposed Method: Calculation when the rotor has a non-magnetic material with $\mu_r = 10^{-6}$

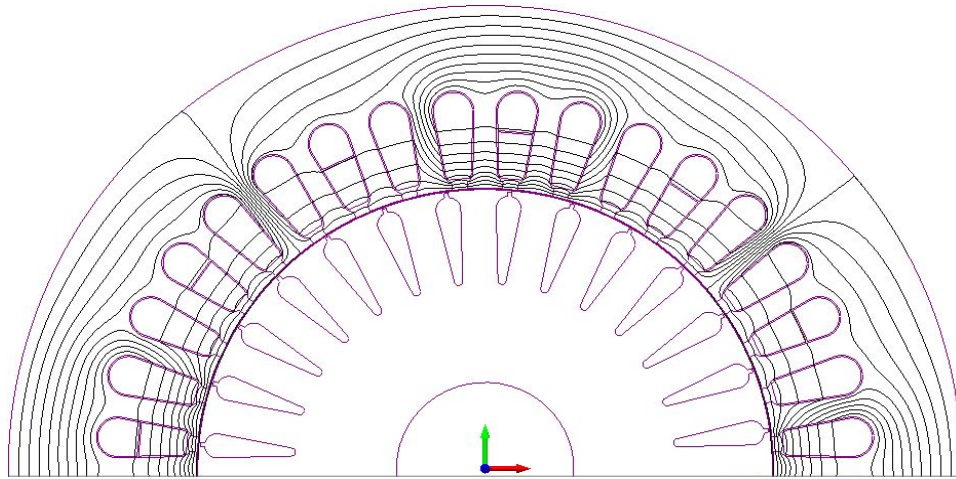
In order to eliminate completely the magnetic field present in the space normally occupied by the rotor, this space is replaced in FEM by a non-magnetic material which has a very low relative magnetic permeability e.g. 10^{-6} . Therefore, the magnetic field does no longer penetrate the rotor space and will only be restricted within the stator core as leakage flux. Fig. 3-4(a) shows the half of the induction machine model in FEM. It also shows the stator leakage field distribution in the machine when the rotor core, bars, and shaft are replaced by a material with a very low magnetic permeability. In Fig. 3-4(b) and the enlarged region in Fig. 3-4(c), it is clear that the flux lines are only constrained in the stator and airgap regions as leakage flux. By using the obtained flux linkages and electric current in one phase in FEM, the stator leakage reactance X'_{ls} is directly calculated as given by:

$$X'_{ls} = 2\pi f_s \frac{1}{n_p} \frac{\sum_{c=1}^n \psi_c}{I_p}, \quad (3-10)$$

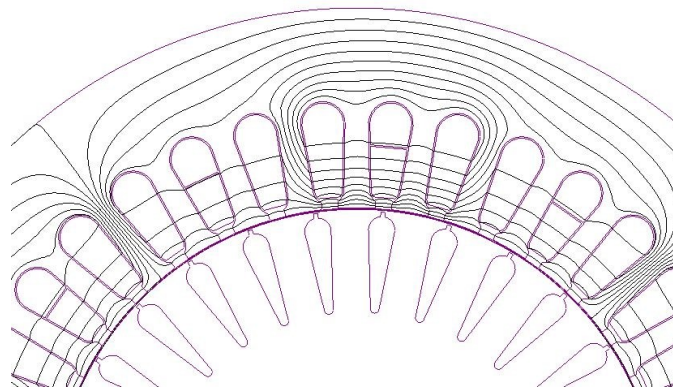
where I_p is the current of the parallel branch per-phase circuit of the stator winding.



(a)



(b)



(c)

Fig. 3-4 Magnetic flux distribution in the induction machine when the rotor space is replaced by a non-magnetic material with $\mu_r = 10^{-6}$. (a) Flux density map. (b) Flux lines. (c) Enlarged view.

Thus, the total stator leakage reactance X_{ls} is then calculated as the sum of the reactance X'_{ls} that is calculated in FEM as in (3-10) and the end-winding leakage reactance X_{end} which is determined in MotorSolve [55] and coupled with the external circuit as shown in Fig. 3-1.

Both aforementioned methods were implemented on the induction machine model in FEM. The machine under test is a three-phase, 5-hp, 220 V four-pole squirrel-cage induction motor. Its specifications and some of the design parameters are listed in Table C-1 in Appendix - C. The total stator leakage reactance values calculated in FEM using the two methods at the rated current condition are given in Table 3-1. The comparison shows the closeness of the total stator leakage reactance for both methods with a relative error of 1.48%. Furthermore, the comparison between the calculated value using the proposed method and the leakage reactance determined experimentally using the conventional locked rotor test with a constant ratio between the stator and rotor leakage reactance values is also presented in Table 3-1. They show an acceptable agreement with a relative error of 1.06%. This verifies the effectiveness of using the proposed technique to determine the stator leakage reactance at the rated current condition.

Table 3-1 Comparison between the total stator leakage reactance calculated in FEM using the two methods and the measured value at the rated current condition

Quantity	Method I: <i>Rotor removed and replaced by air</i>	Method II: (Proposed Method) <i>Rotor replaced by a material with $\mu_r = 10^{-6}$</i>	Relative Error Methods II & I	Measured Value <i>Exp. with constant reactance ratio</i>	Relative Error Method II & Exp.
Total stator leakage reactance X_{ls}	1.9479 Ω	1.9194 Ω	1.48 %	1.8990 Ω	1.06 %

In order to study the stator leakage reactance variation under severe current transients and saturation condition, method II has been implemented using the 2D nonlinear analysis in FEM for a wide range of stator winding electric currents and then, the leakage reactance has been calculated as given in (3-10). Fig. 3-5 demonstrates the stator leakage reactance variation with phase current calculated by using the FEM. Apparently, the stator leakage reactance does not differ significantly with the drawn current and it can be considered as a constant. In fact, this result agrees with the outcome demonstrated in [56] as a function of the slip.

To calculate the rotor leakage reactance, the rotor's core, bars, and shaft will have in this test the original magnetic material (M-45 29 GA) and the coupled circuit model in FEM is operated under the locked rotor test. Current sources are connected to the three-phase stator windings of the induction machine in FEM as shown in Fig. 3-6. To overcome circuit over-

determination, the current source in the third phase is replaced by a direct connection to the common node. The FEM software will determine the current of this phase using Kirchhoff's current law [57]. The rotor circuit is maintained the same as depicted in Fig. 3-1(b). The currents obtained from the previous step are imposed to the FE model. It is assumed that all the flux created in the machine is a leakage flux and the machine is represented by its equivalent circuit

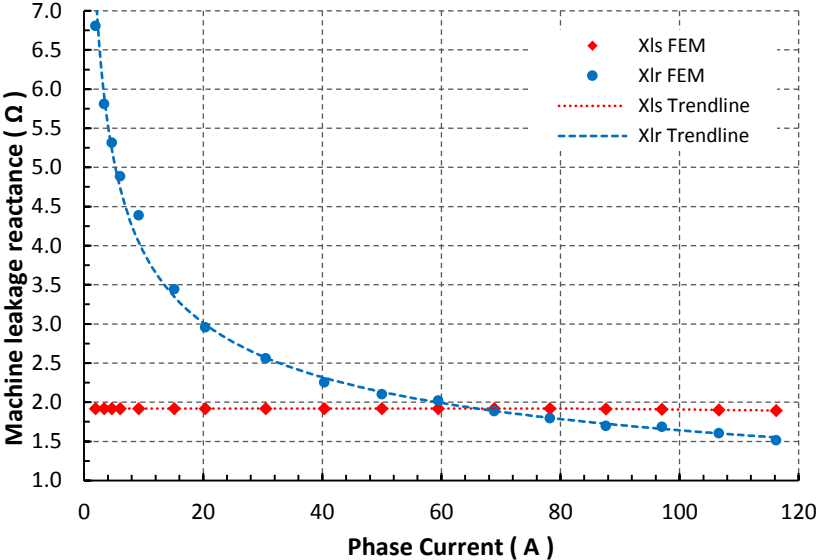


Fig. 3-5 Variation of the stator and rotor leakage reactance with current using the FEM for the 5-hp IM.

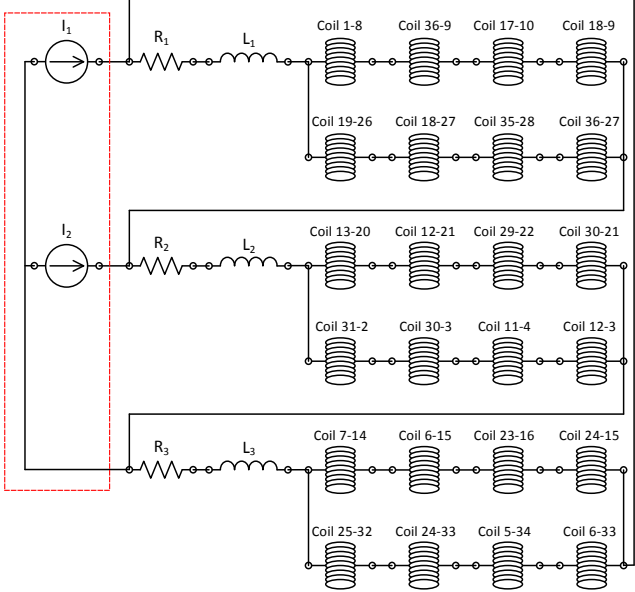


Fig. 3-6 The electromagnetic coupled circuit of the stator in MagNet during the locked-rotor test of IM for rotor leakage reactance estimation.

per phase and the magnetizing branch is neglected. Hence, the total leakage reactance of the machine is calculated using the results obtained from FEM as follows:

$$X_{lFE} = X_{ls} + X_{lr} = \text{Imag} \left(\frac{V_{\phi FE}}{I_{\phi FE}} \right), \quad (3-11)$$

where $I_{\phi FE}$ and $V_{\phi FE}$ are the current and voltage per-phase of the machine in FEM. Then, the rotor leakage reactance is calculated at each specific current value. The variation of this leakage reactance with the drawn phase current is also shown in Fig. 3-5. It is clear that the rotor leakage reactance changes significantly under different loading conditions. At low current values, the rotor leakage reactance increases. This occurs because the rotor slots are closed and the iron bridges on the top of the slots are unsaturated and the leakage flux is large. When the rotor circuit is drawing high currents or under saturation, the leakage flux is very low and the inductance or reactance is also low.

In order to validate the results obtained by implementing method II in the FEM, the total leakage reactance of the real induction machine is measured. The locked-rotor test is achieved based on the two procedures discussed in [58]. Rapid test measurements at 120% of the rated current down to the lowest possible current according to [35] and machine data sheet have been implemented and recorded. Moreover, a motor startup at reduced voltages to obtain the inrush currents is performed. Hence, 100%, 75%, and 50% of rated voltage are applied and the corresponding currents are recorded.

The total leakage reactance for the 5-hp IM has been calculated based on the experimental measurements of the applied voltages and measured phase currents shown in Fig. 3-7 as follows:

$$X_{ltotal} = \sqrt{Z^2 - (R_s + R_r)^2}, \quad Z = \frac{V_{\phi}}{I_{\phi}}, \quad (3-12)$$

where Z is the total stator and rotor impedance. V_{ϕ} is the applied phase voltage and I_{ϕ} is the measured current per phase.

The results in Fig. 3-7 describes the machine at high currents, while the corresponding total reactance values are significantly reduced at the flux saturation condition. Moreover, the total leakage reactance values calculated based on method II in FEM for the same machine have been plotted and compared to the experimental measurements. The figure reveals an acceptable

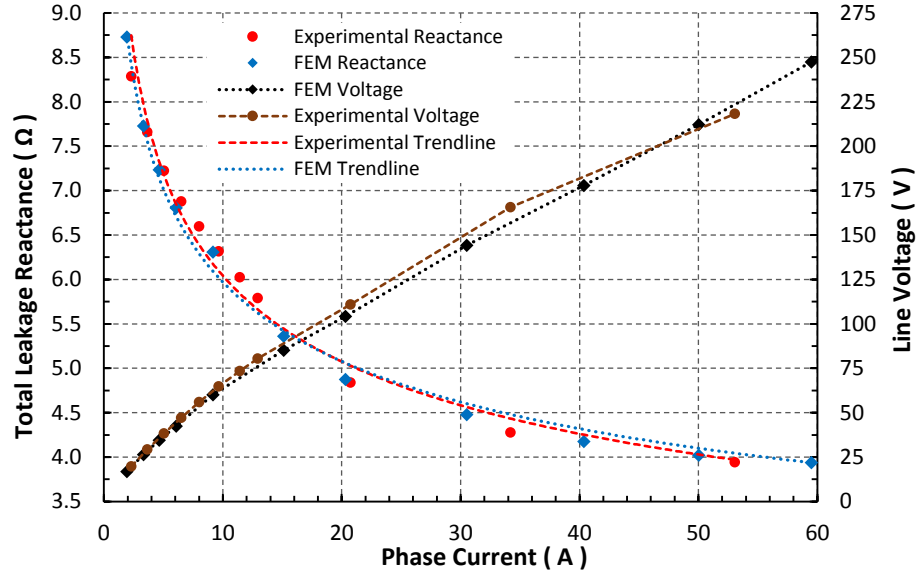


Fig. 3-7 Experimental measurements of the total leakage reactance for the 5-hp machine compared to the calculated values using FEM with the current.

agreement with the experimental results. The slight difference is due to the inaccurate estimation of the end-winding impedance which is considered constant during calculation. However, this error can be mitigated by using a 3D-FEM to determine a more accurate end-winding reactance.

The machine leakage reactance resulted for both the stator and rotor under saturation are then expressed by:

$$X_{lsat}(I_s) \cong k_3, \quad (3-13)$$

$$X_{lr sat}(I_r) = k_4 e^{-c_3 I_r} + k_5 e^{-c_4 I_r}, \quad (3-14)$$

where k_3 to k_5 , c_3 and c_4 are the leakage reactance saturation parameters, they are listed in Table C-3 in Appendix - C. They are updated during each calculation iteration of I_s and I_r . These currents represent the amplitude values of the stator and rotor currents, respectively. They are calculated and implemented in the dq-frame as:

$$I_s = \sqrt{(i_{qs} + i_{ds})^2} \quad \text{and} \quad I_r = \sqrt{(i_{qr} + i_{dr})^2}. \quad (3-15)$$

The ratio between the stator and the rotor leakage reactance (X_{ls}/X_{lr}) values estimated by using the proposed method is calculated and demonstrated with the phase current in Fig. 3-8. At

rated current I_{ph} of 9.2 A (I_{line} of 16 A), the ratio is about 0.447 which represents Design C machines according to IEEE Std. 112™ [34]. The ratio is less than 1 for all currents range up to about 65 A, which represents approximately 7 times the rated phase current. Increasing the drawn current results in a significant reduction in the rotor leakage reactance until it becomes less than the stator leakage reactance of the machine. At extremely high currents, the rotor core is deeply saturated and the reluctance is very high. In other words, the relative magnetic permeability of the rotor core decreases and as a results, it acts as air.

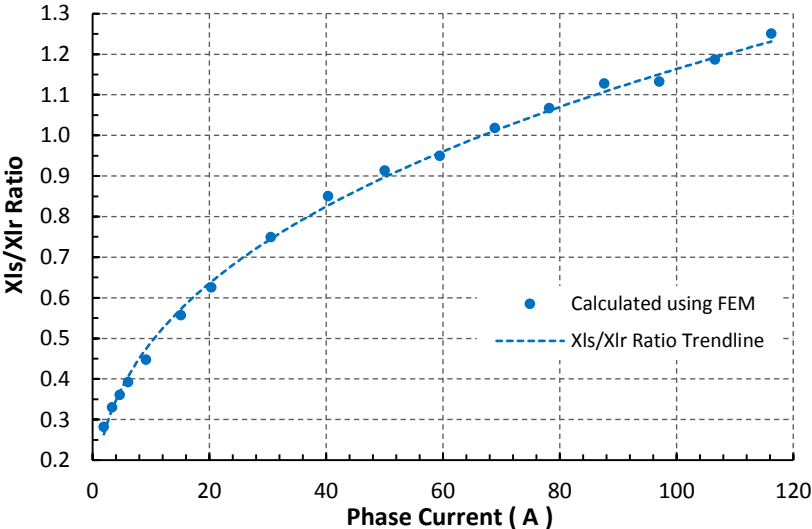


Fig. 3-8 Stator to rotor leakage reactance ratio with current estimated in FEM.

3.4 Experimental and Simulation Results

3.4.1 FEM-based machine parameters with a constant X_{ls}/X_{lr} ratio

The standard machine tests; the dc, no-load and locked rotor tests are implemented in a 2D time-stepping, nonlinear analysis in FEM with a coupled circuit to calculate the main components of the equivalent circuit of the induction machine. The stator, rotor, and magnetizing reactance values have been calculated at rated current condition. They are listed in Table 3-2. The stator and rotor leakage reactance parameters have been primarily separated based on a constant X_{ls}/X_{lr} ratio defined by IEEE Std. 112™ [34]. The results obtained from the FEM are compared with the machine parameters obtained experimentally from the same conventional tests and also listed in Table 3-2. The results show a maximum relative error of 13%. This validates the machine model in FEM with the coupled circuit.

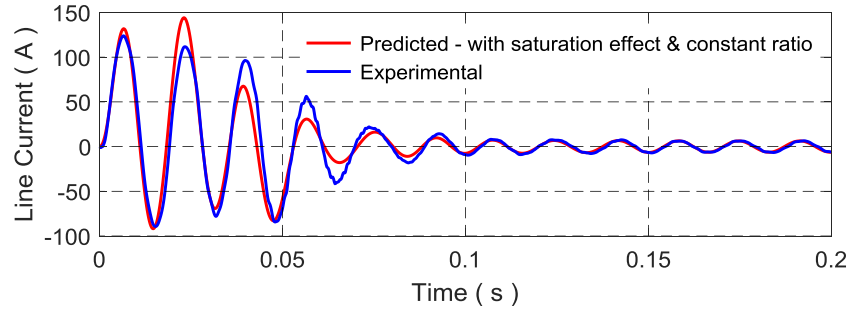
Table 3-2 Comparison between experimental and FEM-based parameters of the 5-hp induction machine with a constant X_{ls}/X_{lr} ratio

Parameter	Experimental Result	FEM Result	Relative Error
Stator resistance R_s	0.965 Ω	0.9679	0.31%
Rotor resistance R_r	1.305 Ω	1.1322 Ω	13.21%
Magnetizing reactance X_m	76.54 Ω	71.3207 Ω	6.82%
Stator leakage reactance X_{ls}	1.899 Ω	1.9194 Ω	1.07%
Rotor leakage reactance X_{lr}	4.42 Ω	4.39 Ω	0.6%

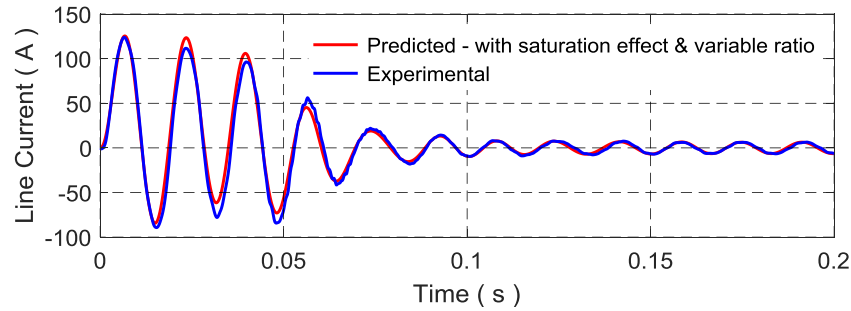
3.4.2 FEM-based machine parameters with a variable X_{ls}/X_{lr} ratio

In IEEE Std. 112™ [34], the calculation of the IM's parameters starts by assuming a constant relationship between the stator and rotor leakage reactance values at all loading conditions. However, machine parameters such as the leakage reactance are highly dependent on the loading conditions as proved earlier. Hence, the dq-model of the induction machine, discussed in Chapter 2 has been simulated in Matlab/Simulink when the saturation effect in the leakage path that derived by using the proposed method is considered. This effect is expressed by the current-dependent functions as given in (3-13) and (3-14). On the other hand, the machine model is also simulated when the X_{ls}/X_{lr} ratio is maintained fixed at 0.43. In fact, this case is realized by separating the total leakage reactance given in (3-12) based on the machine design class specified in its datasheet and assumed by IEEE Std. 112™ [34]. The predicted results obtained from the two aforementioned operating scenarios are compared with the response recorded experimentally for the real machine.

Fig. 3-9 and Fig. 3-10 show the detailed startup responses of the 5-hp induction motor at the rated voltage with no-load. In both figures, the machine model is run when the saturation effect in both leakage flux paths is included. Fig. 3-9(a) shows the predicted line current response compared with the measured response during DOL startup of the induction motor and when the X_{ls}/X_{lr} ratio is kept constant at 0.43 (design C). The figure reveals the discrepancies in the peak values (overshoots) while insignificant difference is noticed in Fig. 3-9(b) when a current-dependent ratio is considered in the machine model. However, both models exhibit an adequate agreement with the measured current response at the steady-state condition. This verifies the effectiveness of including the saturation effect and the current-dependent leakage reactances in the machine model to more accurately predict the machine's dynamic response.

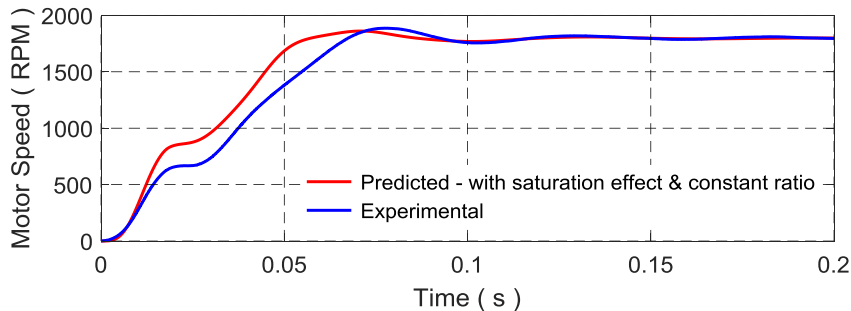


(a)

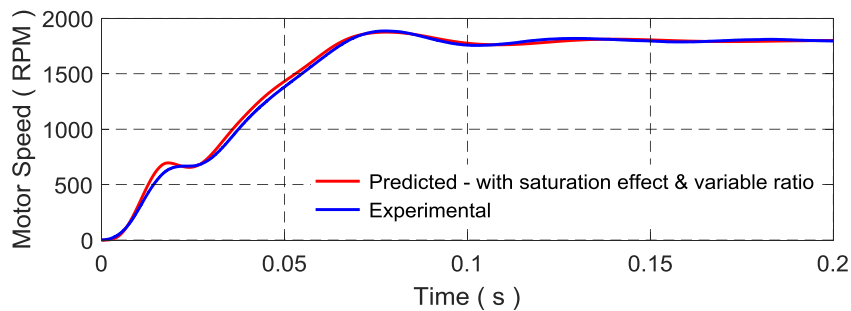


(b)

Fig. 3-9 Predicted current response during DOL startup of a 5-hp IM compared to the experimentally measured current when: (a) the machine model includes the saturation effect with a constant leakage reactance ratio and (b) the machine model includes the saturation effect with a variable leakage reactance ratio.



(a)



(b)

Fig. 3-10 Predicted speed response during DOL startup of a 5-hp IM compared to the experimentally measured speed when: (a) the machine model includes the saturation effect with a constant leakage reactance ratio and (b) the machine model includes the saturation effect with a variable leakage reactance ratio.

During the DOL startup, the predicted speed response of the 5-hp IM model which considers the saturation effect is shown in Fig. 3-10. Moreover, it is compared with the experimental speed response of the motor. Fig. 3-10(a) shows the difference between the two responses, especially in the transient condition or motor acceleration when a fixed reactance ratio is considered. However, this difference can be mitigated by including the variation of the machine leakage reactance ratio in the machine model as demonstrated in Fig. 3-10(b).

In order to investigate the variation of the leakage reactance ratio of the machine under different operating conditions. The machine model which includes the saturation effect in the main flux path which is discussed in [58] and in both the stator and rotor leakage flux paths has been run under the following operating conditions; the DOL startup at rated voltage, running at steady-state with no-load and then operating the motor at the rated conditions. Fig. 3-11(a) shows the response of the line current drawn by the motor at these specified conditions. During the DOL startup, the machine draws enough current values to saturate its core. The machine runs under normal conditions during the steady-state (SS) at no-load condition. However, when a step change of the rated load torque of 20.55 N.m is applied at about 0.4 s, the drawn current passes during another high loading transient current which may saturate the machine's core. Then, the machine's current reduces gradually to reach its rated current at steady-state condition.

Fig. 3-11(b) and (c) depict the variation of both the stator and rotor leakage reactance parameters, respectively during the above-mentioned operating conditions. The stator leakage reactance X_{ls} does not change substantially and keeps fluctuating around the rated value at all scenarios as shown in Fig. 3-11(b). This has been discussed in the previous section. Meanwhile, the rotor leakage reactance X_{lr} reduces significantly during startup which pushes its core to saturate deeply as shown in Fig. 3-11(c). At no-load operation, minimum current is drawn by the rotor circuit which pushes the rotor leakage reactance to the unsaturated region. At the time instant of $t = 0.4$ s, the rated load torque is applied. Higher current is flowing in the rotor circuit to meet the torque demand. Hence, it pushes again the rotor core to saturate which reduces the leakage reactance in the rotor part. When the machines reaches its steady-state condition, its leakage reactance values maintain the rated values which are approximately equal the values calculated and given in Table 3-2. The ratio between the stator and rotor leakage reactance has been calculated and plotted for the same operating conditions. During the DOL startup, a high leakage reactance ratio around 0.8 is shown in Fig. 3-11(d). This is due to the deeply saturated

rotor iron. It also displays a ratio of about 0.3 when it is running with no-load, and around 0.437 at rated conditions. This verifies that X_{ls}/X_{lr} ratio is a current-dependent parameter and to have a closer prediction of IM dynamic response, this ratio should not be assumed constant at all current values.

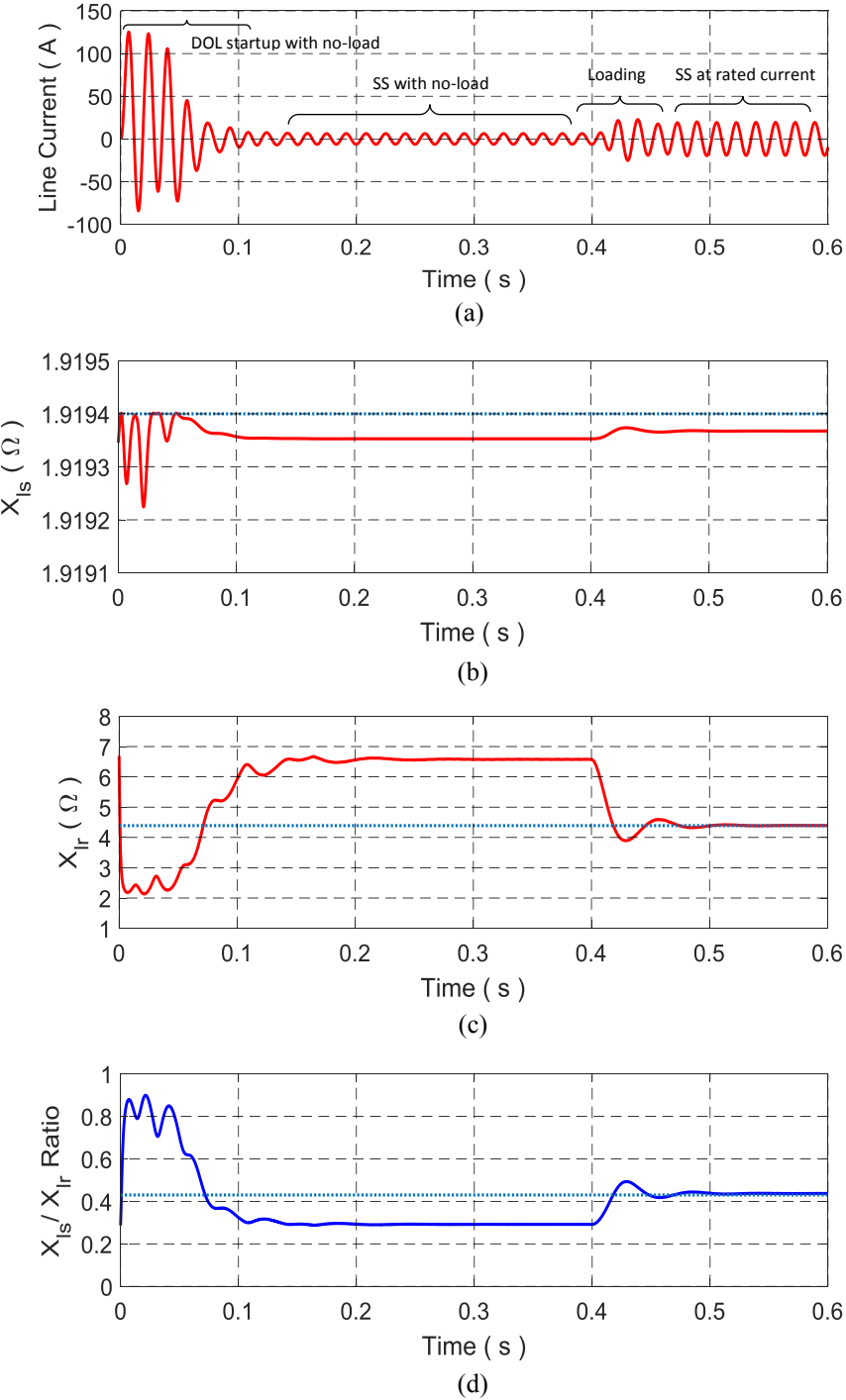


Fig. 3-11 Machine parameters variation during DOL startup, SS with no-load, and loading condition. (a) Line current response. (b) Stator leakage reactance. (c) Rotor leakage reactance. (d) Leakage reactance ratio.

3.4.3 FEM- and Matlab/Simulink- based IM performance including the saturation effect with variable X_{ls}/X_{lr} ratio compared to the experimental IM dynamic response

To verify the machine model that includes the saturation effect and parameters estimated using the proposed method, the machine model has been implemented in FEM and Matlab/Simulink using the dq-model discussed in Chapter II. The predicted response of the induction motor during a severe transient such as the DOL startup are compared with the measured results obtained from the induction motor running at rated voltage and under the same operating condition. Fig. 3-12 shows the line current response drawn by the 5-hp induction motor during the DOL startup at rated voltage with no-load resulted from the FEM and Matlab/Simulink. Both results are superimposed with the experimental response of the machine at same operating condition. The figure exhibits the high peak current values that oscillate at about the source frequency 60 Hz. These peaks push the machine core to saturate. Hence, the model which includes the nonlinear saturation model with variable X_{ls}/X_{lr} ratio exhibits an acceptable agreement with the measured response as displayed in the zoomed part. However, the FEM model shows some differences due to the inaccurate compensation for the end winding reactance. The figure also reveals a good response agreement between the two models and the measured one at the steady-state condition.

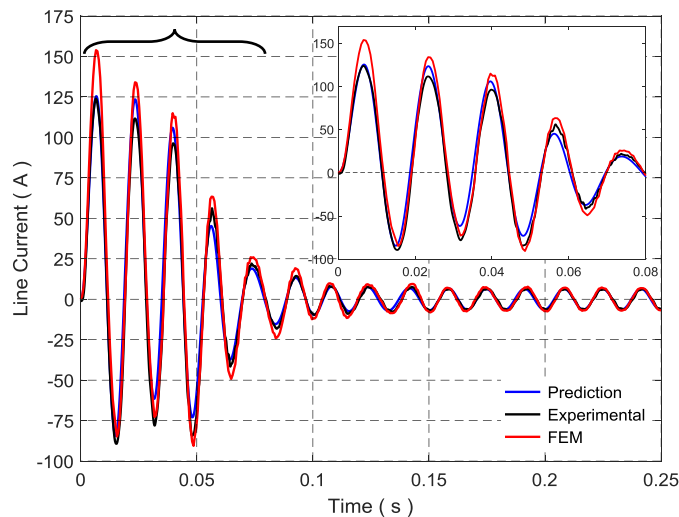


Fig. 3-12 Current response during DOL startup of the 5-hp IM.

The motor speed during the DOL startup in FEM and the predicted by Matlab/Simulink are plotted as displayed in Fig. 3-13. It is then compared to the one recorded experimentally. The

figure demonstrates an acceptable speed response correlation between them. However, the FEM model shows a slight difference due to the reason discussed earlier.

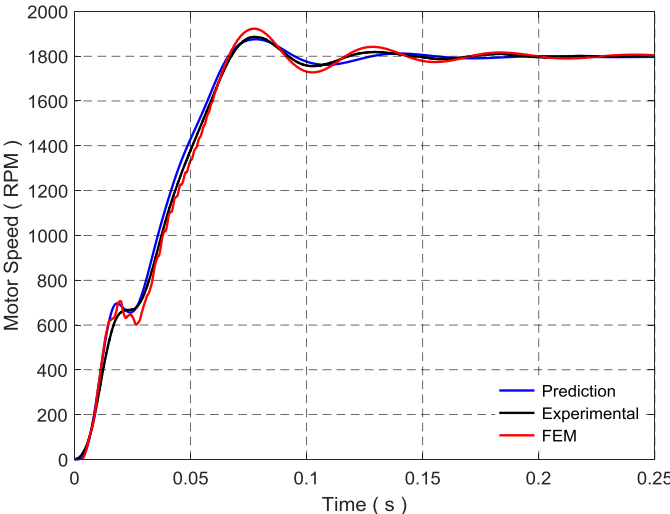


Fig. 3-13 Speed response during DOL startup of the 5-hp IM.

Moreover, the electromagnetic or motor torque response at the DOL startup calculated by the FEM is shown in Fig. 3-14. It reveals a high starting torque and its oscillation around the average value which is compared to the torque predicted by Matlab/Simulink. It demonstrates a good agreement between the model solved in FEM and the model predicted and implemented using the current-dependent leakage reactance parameters extracted using the proposed method in the FEM.

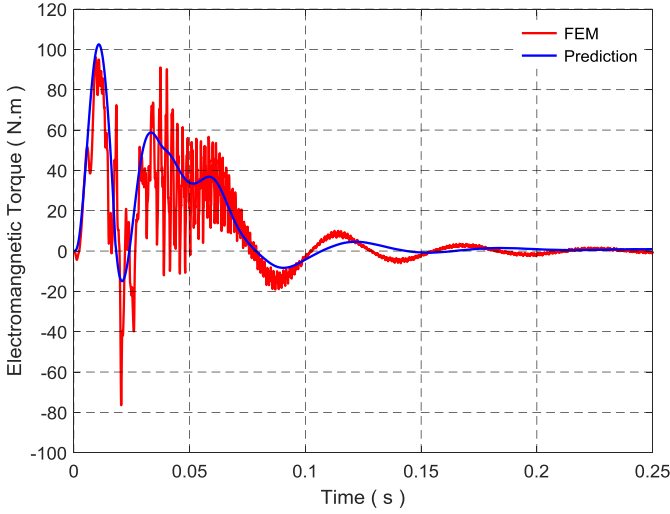


Fig. 3-14 Electromagnetic torque response during DOL startup of the 5-hp IM.

3.5 Summary

The stator and rotor leakage reactance parameters of the induction machine can be calculated and separated according to IEEE Std. 112TM only when the machine is run at steady-state and rated condition. During severe transients such as a DOL startup and loading conditions of a three-phase induction motor, the linear parameters of the equivalent circuit of the machine mainly, the magnetizing and both stator and rotor leakage reactance parameters should be replaced by their current-dependent reactance functions. This ensures including the saturation effect in the machine model and hence, predicting accurately the dynamic performance of the induction motor. Furthermore, the ratio between the stator and rotor leakage reactance X_{ls}/X_{lr} under saturation circumstance is no longer constant. To obtain an accurate ratio, the machine leakage reactance should be separated according to the saturation effect in each stator and rotor flux paths distinctly.

A 2D finite element modeling with the coupled circuit method is proposed to determine accurately the stator leakage reactance of a three-phase squirrel-cage induction motor at different current values. The stator leakage reactance that is determined using the proposed method shows a good agreement with the experimental results when the total leakage reactance is separated according to IEEE Std. 112TM at rated current. The locked rotor test and the current sources in a circuit coupled model in a 2D nonlinear time-stepping in FEM are used to determine and extract the rotor leakage reactance under normal operating conditions and also when the core is highly saturated. The remaining equivalent circuit parameters are determined using the well-known techniques in FEM. These parameters are used to predict the dynamic response of the motor. The results are compared with experimental motor dynamics. Moreover, the effect of a current-dependent leakage reactance ratio on the performance of the induction machine has been studied and results acknowledge considering the variation of this ratio to accurately resemble a real machine. Results show the effectiveness of the method discussed in this chapter. More accurate parameter estimation using the proposed method can be implemented when a 3D FEM is used in calculating the stator end-winding reactance.

Chapter 4. Power Electronic Converter-Based Induction Motor Emulator Including Main and Leakage Flux Saturation

4.1 Introduction

Different kinds of electrical machines are being considered for electrified transportation systems. Since the 1990's, induction machines (IMs), specifically the squirrel-cage type has been used in the propulsion systems [59]. This is due to its robustness, high-torque density and shock resistance, reduced acquisition and maintenance costs, safe operation, low vibration and acoustic noise emissions [60]. Induction motors and their drives have been increasingly utilized in large-power, high-voltage applications pertaining to marine propulsion systems especially when high-torque density and shock resistance are required [61]. Other applications of induction machines compared to other special machines in the field of traction system in electric/hybrid vehicles are reported in [62]. An induction machine diagnosis process to improve the availability and reliability of the transportation system is addressed in [63]. The approach helps to predict early faults of voltage imbalance and inherent asymmetry.

The electromechanical system for an electrical machine with its associated load can be replaced by solid-state devices that can be controlled and flexibly programmed to emulate a real machine. An emulator is typically a bidirectional power electronic interface; it has the capability to run either as an energy sink which draws electrical power from the grid or as an energy source by feeding back the energy. Furthermore, the emulator can be used to provide different load characteristics whereby various control algorithms and industrial converter designs can be tested. This offers a flexible platform to test machines and inverters in a laboratory environment.

Dimensional analysis was used in the 1960's to obtain preliminary test results before constructing a prototype by establishing laws of similitude between the original and its model [8]. The shortcoming of this approach lies in the difficulty of scaling the ratio of machine inertia to frictional loss [9]. Alternatively, power electronic systems are fast and accurate. They allow flexible control algorithms at numerous power levels. Hence, it is feasible to use the power electronics and their controls to mimic static or slow time-scale electrical dynamics in emulators. Machine emulation is achieved by simulating the dynamic model of the required system component in a real-time controller. The generated current and voltage commands of the model can then be used as reference signals for the controller of the power converter.

An induction machine emulation (IME) test platform is implemented in [10]. The emulating converter is interfaced with a variable speed drive via a transformer-based LCL-type coupling network. Different system inductances are considered constant and the saturation effect is not included in the IME model, this results in inaccuracies in the emulator performance. Another drawback of the IME stated in [10] is the initial peak voltage of 10V that is required for a stable phase-locked loop (PLL) operation prior to enabling the IM model operation.

A three-phase IME in the dq-reference frame is introduced in [22]. During start-up, the emulator's dq-currents show similar output responses of an induction motor with some differences in peak values. The dynamics of an inverter-virtual induction motor is examined in [12]. The inverter is connected to a bidirectional converter through a line inductor. The virtual machine is controlled by using a PI-controller in the abc-reference frame. Likewise, it discusses the virtual machine running in the steady-state condition.

In an attempt to increase the power and frequency capabilities of the testing platform, a multilevel parallel switch-based converter is applied in [13]. The virtual machine draws the same currents from the motor drive during transient and steady-state conditions. It shows high bandwidth and low-harmonic current content. The drawback of this topology includes the cost of structural complexity in the three-phase 'LinVerter' and a large number of devices and common-mode chokes. A current control method using a linear quadratic regulator optimization is proposed in [26]. The proposed IME was validated experimentally. However, the current tracking is inaccurate with unwanted high order harmonics being introduced into the line currents.

The main and leakage reactance parameters of the IM were experimentally calculated and verified. The obtained current-dependent reactance functions for a 2-hp machine were included in the mathematical model of the IM. The simulation results of the converter-based IM emulator were presented by the authors in [58].

In this chapter, the work is modified and extended by updating the literature review with the most recent related publications. Experimental procedures are used to calculate the parameters of the mathematical model for the 5-hp induction machine. The leakage reactance parameters of the machine are extracted and separated by using the finite-element modeling (FEM) when the machine is deeply saturated. The machine model that includes the saturation effect in both the main as well as the stator and rotor leakage flux paths has been verified

experimentally with the real machine. Furthermore, an emulator based on a power electronic converter (PEC) has been developed and the proportional-resonant current controller in the abc-frame has been used. The IME has been tested and results show the effectiveness of the developed emulation system to resemble closely the dynamic performance of the actual motor especially, during direct online (DOL) startup and loading conditions.

4.2 Induction Motor Emulator Structure

In order to replace expensive test benches and equipment as well as the risks associated with development and testing of new drive systems, electrical machine emulator can be used. Various kinds of electric machines with different power ratings or the conventional and advanced control strategies can be tested. This can be implemented by utilizing the concept of power hardware-in-the-loop (PHIL) along with an inclusive model of the machine and load dynamics.

4.2.1 Voltage source converter

The structure of the machine emulation in the abc-frame is depicted in Fig. 4-1. It shows the main elements of an emulation system. Basically, it comprises two back-to-back, six-switch, bridge-type voltage source converters (VSCs). One runs as an active front-end converter (AFEC) to maintain a fixed DC link voltage of the emulator and also control the bidirectional power flow from/to the emulating converter. The three-phase currents drawn by the PEC are

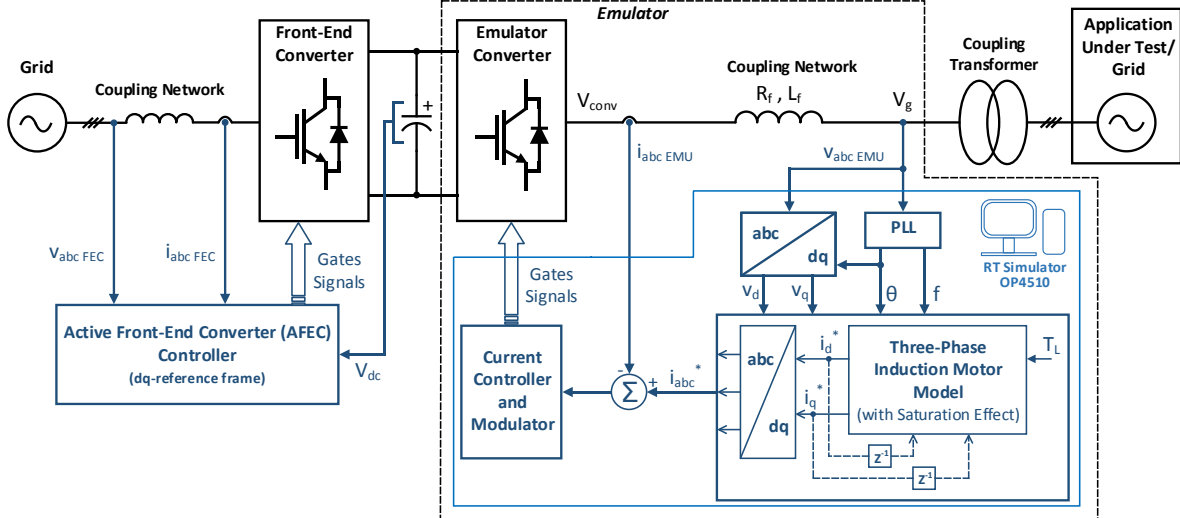


Fig. 4-1 Emulator structure with abc-reference frame current control.

compared with the calculated currents in a real-time simulator (RTS). The error signal is the input to the current controller in which the output signal is sent to the modulator to generate the required pulses of the emulating converter. This offers a flexible way to test and analyze the characteristics of the emulated machine or device under test at particular operating conditions.

A coupling transformer is used for isolation purposes and to avoid common-mode circulating currents flowing through the power converter assembly. The transformer rating, as well as the coupling network, are chosen appropriately so as to avoid saturation, which could complicate emulator control significantly. As shown in Fig. 4-1, the parameters of the induction motor model would change depending on the type of the motor being emulated e.g. squirrel-cage or wound-rotor. However, the developed system can emulate a machine up to 15 hp at steady-state with a current control bandwidth capability up to 2 kHz but it is limited only by the converter ratings.

4.2.2 Synchronous reference frame phase-locked loop

Grid-connected applications require an accurate and fast estimate of the grid or supply angle. In fact, the quality of the phase-lock directly affects the control loop performance in grid-tied applications [64]. A method to design an industrial phase-locked loop discussed in [65] is employed in this research work as presented in Fig. 4-2(a). It uses the three-phase measured voltages of the power supply as inputs and performs an abc- $\alpha\beta$ -dq transformation. The phase-lock procedure is implemented in the synchronous reference frame by using the q-component as the phase detect value. For a balanced three-phase system when PLL is locked, v_q reduces to zero. When it is not locked or there is a small error, v_q is linearly proportional to the error. Hence, a PI-controller is included to eliminate the steady-state error. The output of the controller is the grid (supply) frequency which is added to the feed-forward frequency to provide the grid phase angle. The PLL should also be able to reject frequency variation and phase loss and maintain a phase-lock to the grid. The block diagram of the PLL algorithm is implemented and tested while the proportional gain and integral time are calculated according to [65] as $K_p = 533$ and $T_i = 4$ ms, respectively. Fig. 4-2(b) shows the simulated behavior of the PLL when the grid frequency varies to 60.5 Hz and a phase jump of 90° occurs. The figures exhibit that the PLL is capable of locking into the grid phase angle with less than 18% of the cycle and estimating the grid frequency within 47 ms under different disturbances.

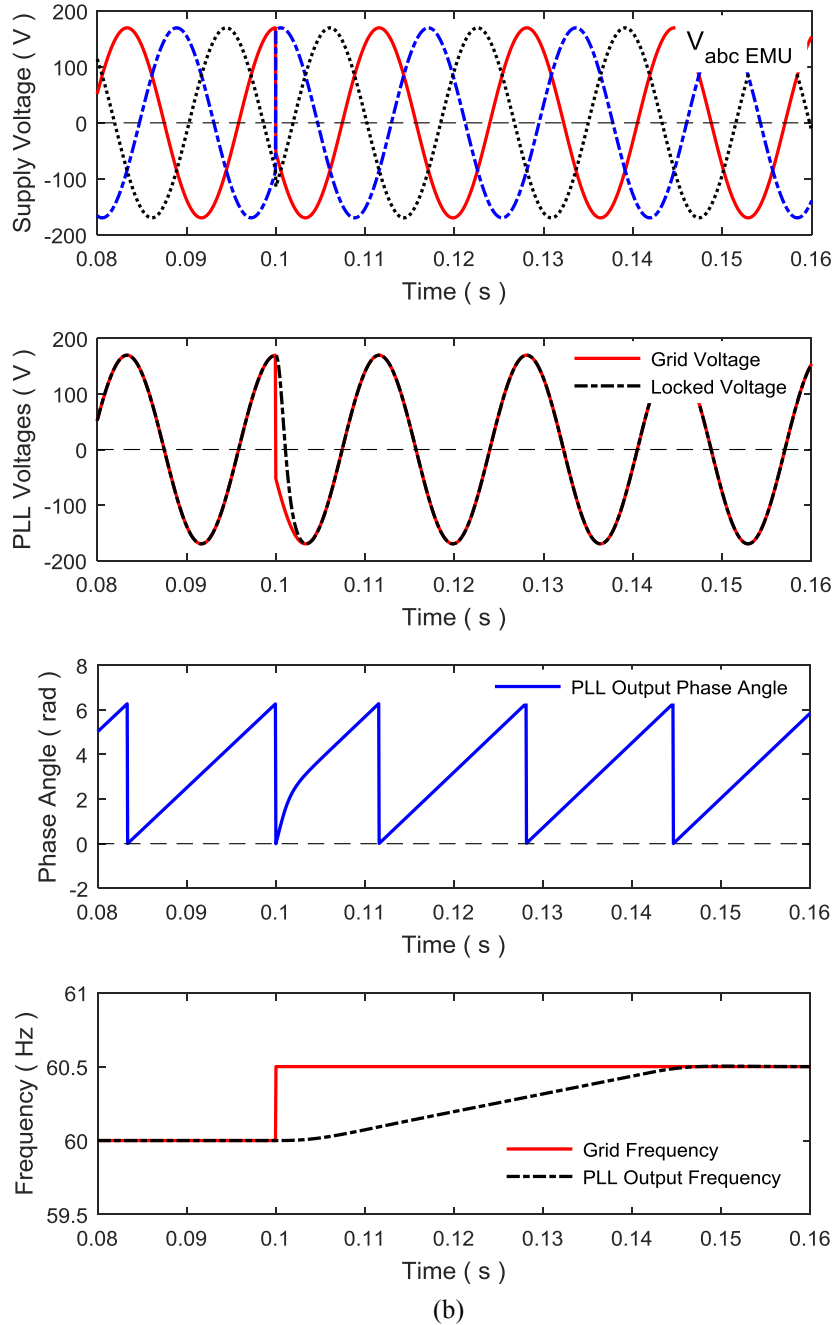
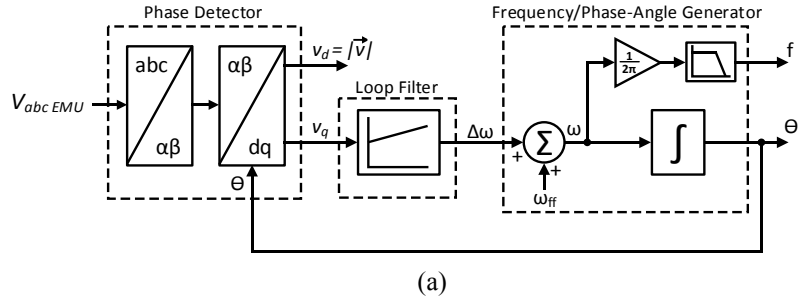


Fig. 4-2 A three-phase synchronous reference frame PLL. (a) General structure. (b) PLL response to varying grid frequency 60.5 Hz and a phase jump of 90° .

4.2.3 Coupling network

Another essential element in the emulation system shown in Fig. 4-1 is the coupling network which connects the emulating converter with the grid or the application under test (AUT). Moreover, It helps in designing the control scheme of the emulating converter.

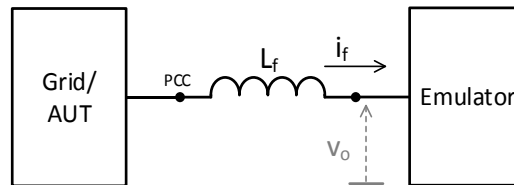
The simplest coupling configuration is shown in Fig. 4-3(a) in which the emulator is connected to the grid (or AUT) through an inductor L_f as a filter. The added inductor results in a higher effective value of the ac side inductance which reduces current harmonics and improves the power factor [66]. The Laplace transfer function of the inductor filter is given by (4-1).

$$H_f(s) = \frac{I_f(s)}{V_{PCC}(s) - V_o(s)} = \frac{1}{L_f s} . \quad (4-1)$$

An alternative topology can be used by adding a filter capacitor C_f , which sets up a low pass filter at the input of the emulator as depicted in Fig. 4-3(b). This provides a low impedance path for high switching frequency current ripples. Moreover, the voltage at the PCC will improve. Conversely, since the current drawn from the grid is different from the desired reference currents. Therefore, while a large capacitor C_f will result in a smooth PCC voltage, the resulting error in the currents drawn from the grid will increase as $i_c = C_f \frac{dv_{pcc}}{dt}$ [26]. Obvious drawbacks of this topology are cost, size (space), and losses [66]. The transfer function of this topology is expressed by (4-2).

$$H_f(s) = \frac{V_o(s)}{V_{PCC}(s)} = \frac{1}{L_f C_f s^2 + 1} . \quad (4-2)$$

The third configuration that is shown in Fig. 4-3(c) is used specifically when an AUT (e.g. inverter) is used. The inductor L_f and capacitor C_f filters help in removing some of the switching frequency harmonics producing a smoother inverter current i_i .



(a)

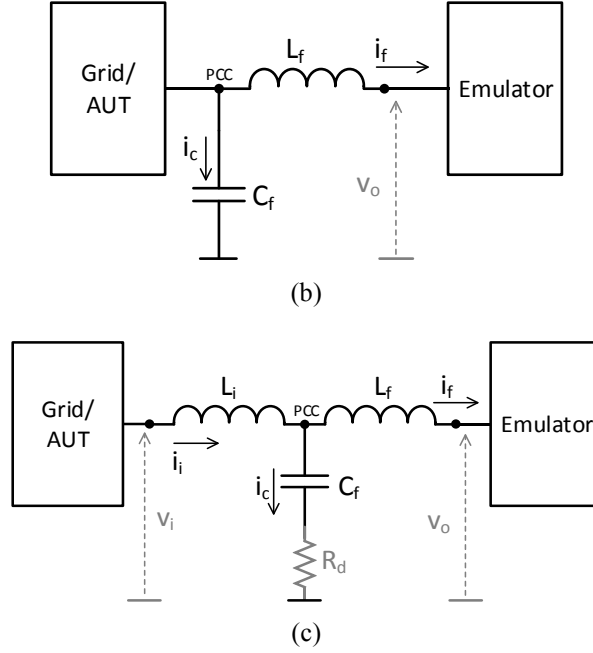


Fig. 4-3 Grid-emulator network coupling per-phase using: (a) An L. (b) An LC. (c) An LCL.

The complete configuration for the equivalent single-phase LCL filter for power converter input is shown in Fig. 4-4.

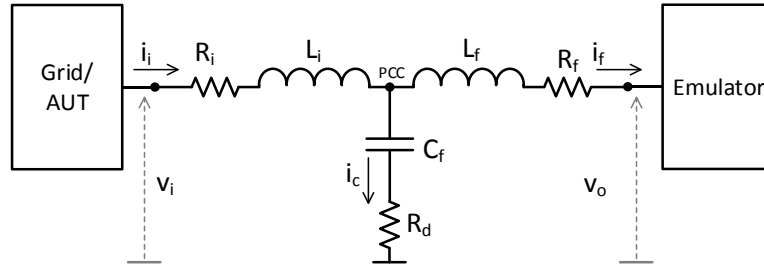


Fig. 4-4 Equivalent circuit for a single-phase LCL filter.

The corresponding mathematical model is given as follows:

$$i_i = i_c + i_f, \quad (4-3)$$

$$v_i = v_{PCC} + R_i i_i + L_i \frac{di_i}{dt}, \quad (4-4)$$

$$v_o = v_{PCC} - R_f i_f - L_f \frac{di_f}{dt}, \quad (4-5)$$

$$v_{PCC} = \frac{1}{C_f} \int i_c dt + R_d i_c, \quad (4-6)$$

where v_i and i_i are the voltage and current values of grid or AUT side, respectively. v_o and i_f are the voltage and current values of the emulator side, respectively. R_d is the damping resistor which helps in absorbing part of switching frequency ripples to avoid resonance [67].

The block diagram of the LCL filter including all parasitic resistances of the filter capacitance is shown in Fig. 4-5.

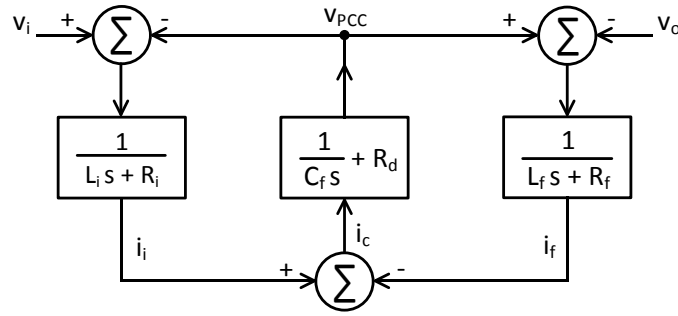


Fig. 4-5 Equivalent circuit for a single-phase LCL filter.

Its transfer function is derived in Appendix - B and expressed as follows:

$$H_f(s) = \frac{I_f(s)}{V_o(s)} = \frac{L_i C_f s^2 + (R_i + R_d) C_f s + 1}{-L_i L_f C_f s^3 - (R_f L_i + R_i L_f + R_d L_f + R_d L_i) C_f s^2 - (R_i R_f C_f + R_d R_f C_f + R_i R_d C_f + L_f + L_i) s - (R_f + R_i)}. \quad (4-7)$$

Although LCL coupling network shows some advantages over other types of filter, however, it complicates the emulator control which reduces the emulator bandwidth and then decreases significantly the emulation accuracy. Moreover, poor filter design may cause lower attenuation than expected or a distortion increase because of oscillation effects [67].

4.3 Current Controller Design

The performance of the emulator relies mainly on the current control approach used in the emulation system. The current control loop ensures that the converter with the help of a three-phase coupling network (in this case, an inductor) draws the desired current from the grid or application under test. The implementation of the emulator current control in the natural abc-

reference frame is depicted in Fig. 4-6. The three-phase measured current signals are compared with corresponding current references calculated by the motor model in the RTS. The error signal is the input to the proportional-resonant (PR) current controller. The output of the controller is the input to the pulse-width modulation (PWM) generator. The generated gate drive signals are the duty cycles that control the three-phase power converter. The current loop dynamics is governed by:

$$v_{con}(t) = L_f \frac{di(t)}{dt} + R_f i(t) + v_g(t), \quad (4-8)$$

where $v_{con}(t)$ is the converter-side voltage, $v_g(t)$ is the grid-side voltage, R_f and L_f are network filter parameters, and $i(t)$ is the drawn current.

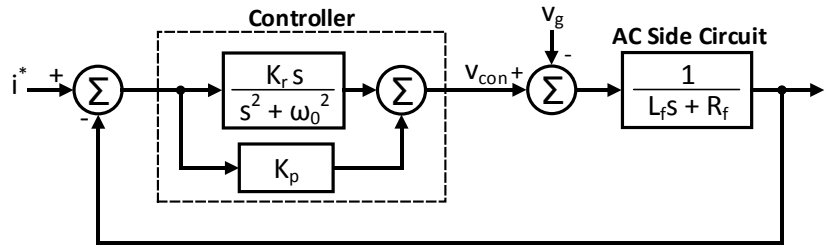


Fig. 4-6 Block diagram of the AC-input current control system.

Developing the transfer function for the coupling network current and voltages; the grid-side voltage can be considered as a disturbance signal while designing the current control system, then the transfer function of the AC side is obtained as:

$$G_{ac}(s) = \frac{I(s)}{V_{con}(s)} = \frac{1}{L_f s + R_f}. \quad (4-9)$$

In the natural abc-reference frame, the control variables, which are the source currents, are time-varying waveforms. Hence, PI controllers encounter difficulties in eliminating the steady-state error. The tracking error can be minimized by choosing a larger controller gain [13].

The proportional-resonant (PR) controller developed in [68] has been recently used in [69] - [72] to regulate the current in grid-tied systems. It shows its capability of eliminating the steady-state error when regulating sinusoidal waveforms without using the acquired values of the supply voltage and the network coupling parameters. Furthermore, this controller can be

used with carrier-based PWM rectifiers in which the switching frequency is maintained constant and hence, it is suitable for high power rectifiers [68]. Its transfer function is expressed by [73]:

$$G_{PR}^{abc}(s) = K_p + \frac{K_r s}{s^2 + \omega_0^2}, \quad (4-10)$$

where K_p is the proportional gain, K_r is the resonant controller time constant, and ω_0 is the resonant angular frequency which is set to the angular frequency of the supply voltage.

The PR controller is characterized by a very high gain in a narrow band around the resonance frequency which facilitates elimination of the steady-state error. The frequency bandwidth around the resonance point relies on the resonant controller time constant. A low time constant results in a narrow bandwidth, whereas larger time constant results in a wider band. The Bode plot of the PR controller is shown in Fig. 4-7. It describes the effect of varying the resonant controller time constant on the controller gain and operating bandwidth.

By using the ac-side transfer function given in (4-9) and the controller transfer function given in (4-10), the closed-loop transfer function of the current control is written as:

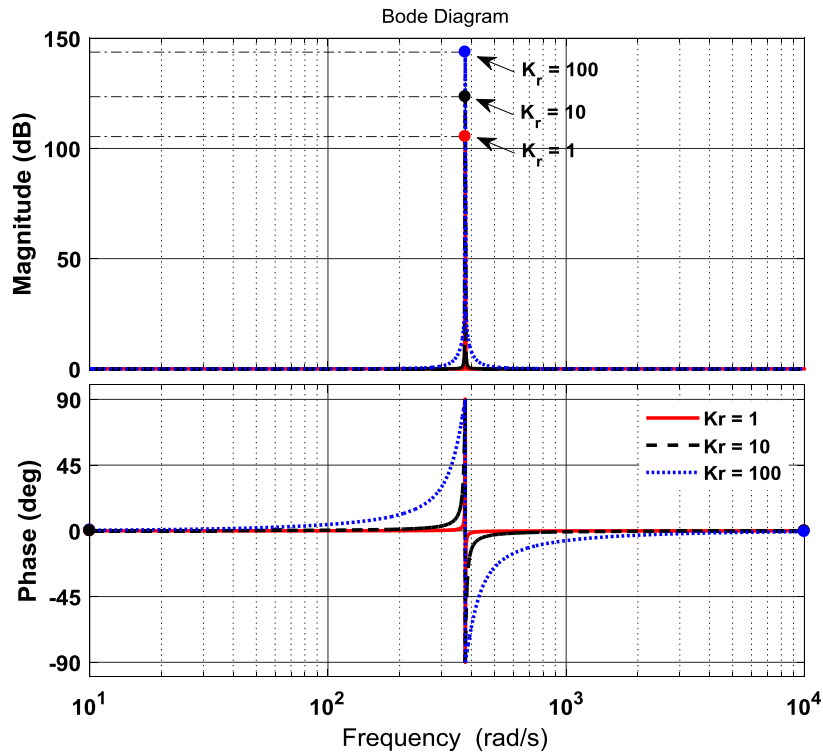


Fig. 4-7 Bode plot of PR current controller with different values for K_r .

$$H_{CL}(s) = \frac{I(s)}{I^*(s)} = \frac{G_{ac}(s)G_{PR}(s)}{1+G_{ac}(s)G_{PR}(s)} \quad (4-11)$$

The value of the resonant controller time constant has been chosen using the Bode plot of the open-loop system in which the value of $K_r = 100$ provides a high gain at the resonant frequency of the controller which is 60 Hz, thus having a minimum steady-state error. Moreover, the frequency response of the closed-loop system given by (4-11) is used to obtain the proportional gain of the PR controller with a damping factor (ζ) of $1/\sqrt{2}$. Hence, the proportional gain of the controller has been selected as $K_p = 1$.

The controller (4-10) has an objective to achieve a zero phase and magnitude error. Since the controller has an infinite gain at, or close to, the grid frequency as depicted in Fig. 4-7, it is still weak when frequency changes. A possible method to solve this concern by inserting a damping factor and choose a bandwidth of the controller system represented by the cutoff frequency ω_{co} as given in (4-12) [74].

$$G_{PR}^{abc}(s) = K_p + \frac{K_r \omega_{co} s}{s^2 + 2\omega_{co} s + \omega_o^2} \quad (4-12)$$

where ω_{co} is selected so $\omega_{co} \ll \omega_o$.

From (4-12), it is clear that the steady-state output phase and magnitude error achieved by this controller is still approximately zero, provided $G_{PR}(s)$ continues to achieve a relatively high gain at the resonant frequency as shown in Fig. 4-8. As seen from the plot, the resonant gain has now a finite gain of around 35 dB which is quite high to eliminate the tracking error. Furthermore, the band width around the resonant frequency has been increased which minimizes the sensitivity of the controller to slight grid frequency variations. However, the gain has reduced. For this work, ω_{co} is chosen as 10 rad/s. Greater than this value, the reference frequency will reduce.

For variable frequency applications, it is required that the resonant frequency of the PR-controller is continuously adjusted to match the output fundamental frequency. However, this is not challenging since different standard techniques in signal processing theory can be utilized to operate across variable frequencies. For digital implementation, the digital filter coefficient needs to be re-calculated to suit the target frequency. This coefficient can be computed as part of the control loop calculation [74].

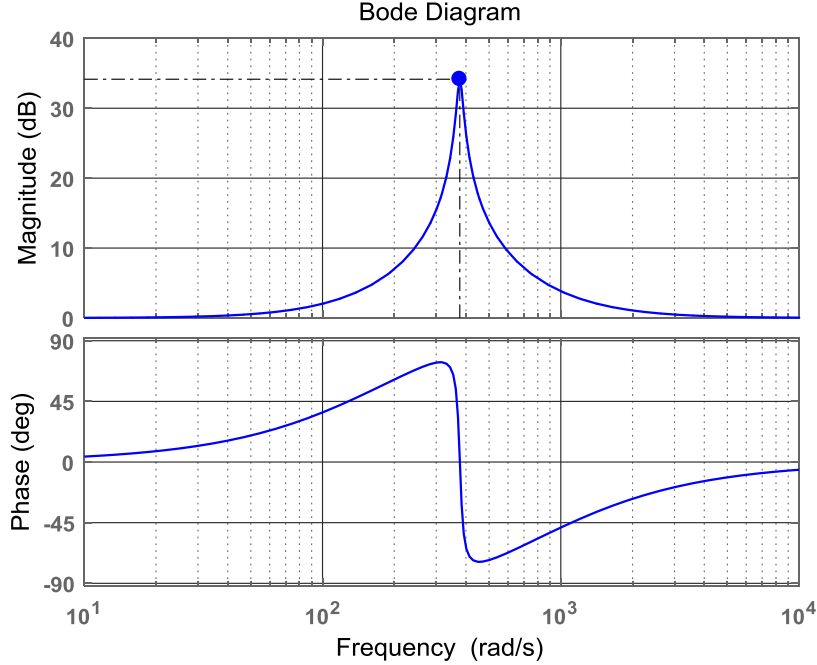


Fig. 4-8 Bode plot of PR current controller with damping factor $\omega_{co} = 10$ rad/s, $K_p = 1$, and $K_r = 100$.

4.4 Experimental Results and Discussion

The validated model for the 5-hp IM that is discussed in Chapter 2 and modified in Chapter 3 was run on the real-time simulator (RTS) OP4510 from OPAL-RT[®] [75] and the current responses were used as the reference signals for the developed emulator.

The experimental setup for the emulation system is shown in Fig. 4-9. It consists of a back-to-back, two-level VSCs, an RTS, which runs the IM model and controls both the emulator converter and the AFEC in real-time, over-voltage and over-current protection circuits, coupling inductors for both converters, and the isolation transformer. The two-level SEMICRON-VSCs are designed to run at 440 V AC, 30 A-RMS per phase with a DC-link voltage of 750 V [76]. The AFEC control has to be fast so the emulator converter can attain the reference response. The switching frequency chosen for both converters is 15 kHz. The AC terminals of both VSCs are connected to the AC grid (220V) through coupling filters of 2.5 mH. The controller design for the AFEC is not discussed in this work, details pertaining to the control structure and controller gains design required for the AFEC are explained in [77]. However, the appropriate controller gains are chosen to have a current control loop bandwidth of about 4 kHz.

In the emulation system developed in this research work, the line to line voltage achieved is around 220 V, as this is the rated voltage of the machine being emulated. This requires a DC

bus voltage of 350 V and the same is maintained by the AFEC control. Currents within the switch rating, around 40 A peak is achieved by the machine emulator system. The VSC of the machine emulator system is operated at a switching frequency of around 15 kHz which is close to the maximum possible switching frequency [76]. A standard triangle comparison-based PWM is used and hence, the switching frequency and carrier frequency are the same.

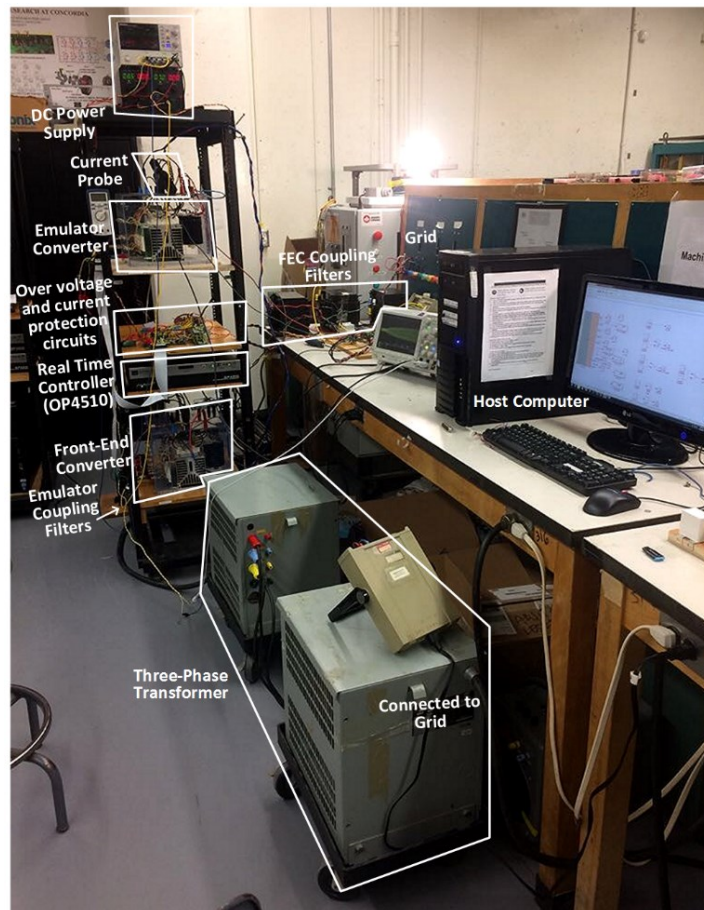


Fig. 4-9 Experimental setup for the power electronic-based induction motor emulation system.

The current control bandwidth is limited by the switching frequency of the inverter, which is 15 kHz, and the sampling time of the real-time simulator, which is 40 μ s. Typically, the innermost controller which is the current controller needs to be at least 5-10 times slower than the switching frequency of the voltage source inverter [77]. Hence, the current controller of the emulating converter is designed to achieve a bandwidth of around 2 kHz. This is the maximum possible bandwidth achievable by the emulator system for the given VSC specifications of the emulating converter.

The 5 HP machine has a stator resistance of 0.9649Ω and a stator leakage reactance of around 5 mH, which results in a time constant of around 5 ms. Hence, the designed emulator current loop, which has a bandwidth of 2 kHz is quite sufficient to emulate the transients associated with this machine. The developed IM emulator is capable of emulating the machine's behavior within the voltage and current ratings of the VSC used as the emulating converter. It is designed for a voltage rating of 440 V line-line RMS and a current rating of 30 A RMS. These rating limits cannot be exceeded during the transient behavior of the machine. A higher rated converter would allow larger machines to be emulated.

In order to show the effectiveness of the developed emulator and its controller capability at severe conditions, a DOL startup for the 5-hp induction motor emulator test was implemented. The DOL startup current for this machine can exceed the rated current of the switches hence, the motor model and the PEC-based emulator were run with a reduced voltage under no-load conditions.

Fig. 4-10 presents the experimental results of the phase current response drawn by the induction motor model in the real-time simulator during the DOL startup with no-load. As stated earlier, due to the limitation of the rated current of the emulating converter, which is rated at 30

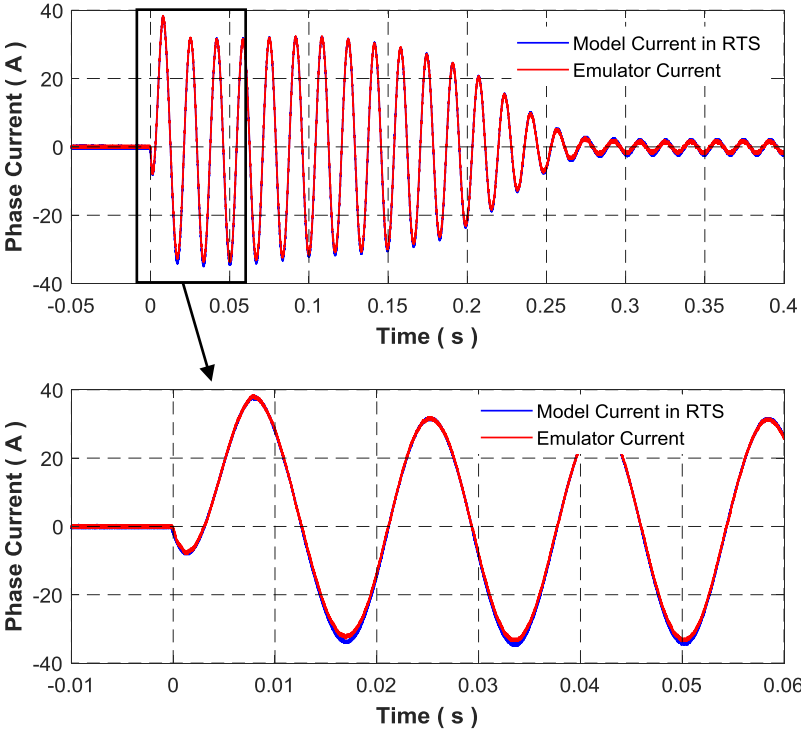


Fig. 4-10 Experimental phase current response drawn by the 5-hp IM emulator during the DOL startup with 60% of the rated voltage and no-load compared to the current drawn by the IM model in RTS.

A RMS and corresponds to about 42 A peak value [76], the applied voltage is reduced to 60% of the rated voltage and phase currents were emulated. The figure reveals the high starting current transients of the induction motor model, which reach a peak value of about 36 A with an oscillation frequency nearly equal to the supply frequency of 60 Hz for about 250 ms. Moreover, the figure displays the phase current drawn by the power electronic-based IM emulator under the same operating conditions. The drawn current by the emulator correlates well with the current waveform measured in real time which proves the effectiveness of the control scheme.

The current drawn by the emulator during the DOL startup at 60% of the rated voltage and the no-load condition has been compared with the current drawn by the real 5-hp machine running at the same operating conditions in Fig. 4-11(a). The figure shows an acceptable current response for the developed emulator. The experimental phase current responses of both the real motor and the PEC-based emulator at steady-state are shown in Fig. 4-11(b). It demonstrates a

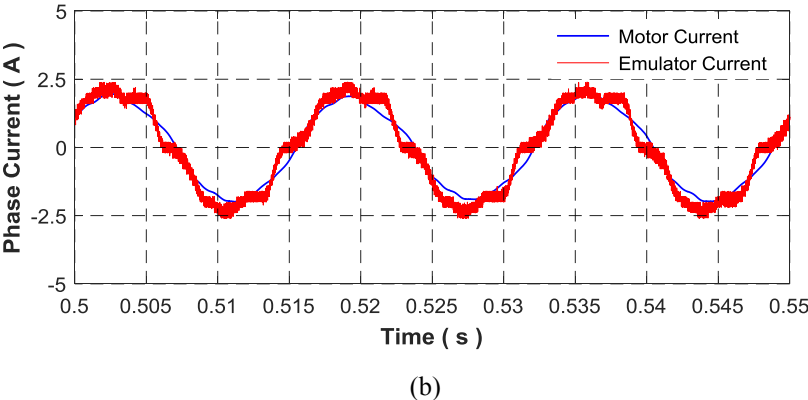
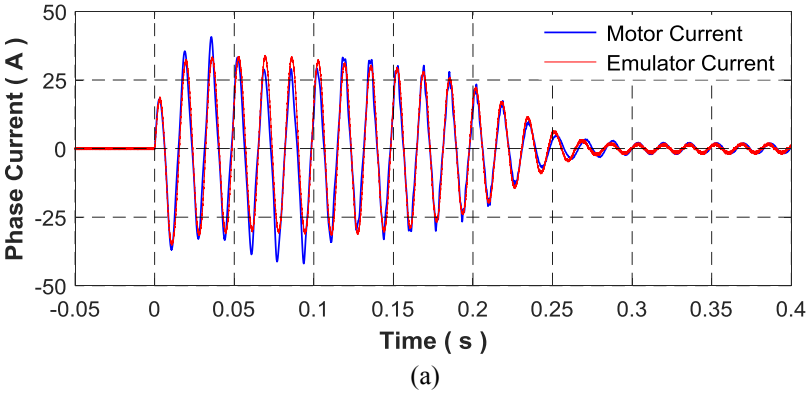
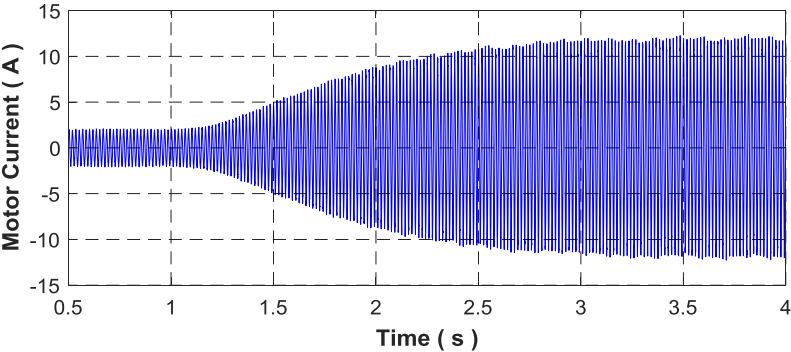


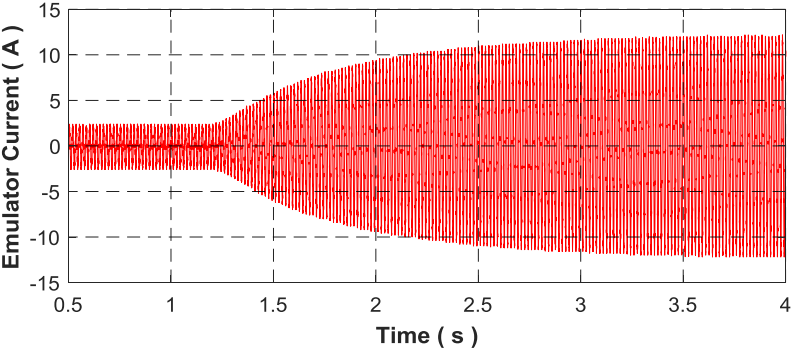
Fig. 4-11 Experimental phase current response of the 5-hp IM PEC-based emulator at 60% of the rated voltage and no-load condition compared to the real machine’s current response under similar operating conditions during: (a) DOL startup and (b) steady-state operation.

good agreement between both waveforms with some ripple around the desired value. This is due to the switching frequency of the PWM technique that is used to switch the six power electronic devices at low current. The distortion around zero-crossing is due to the dead time of about $2 \mu\text{s}$ that is predetermined for the converters arms for all phases. A higher bandwidth converter would produce lower ripples.

In order to demonstrate the effectiveness of the developed emulator and to study its dynamic response, the IM emulator is subjected to load torque. The real machine has been coupled to a 13-kW DC dynamometer and run under no-load, a load has then been applied at about 1.25 s and the motor current captured is shown in Fig. 4-12(a). The applied load is equivalent to a motor load torque of 12 N.m and a peak-to-peak current of about 23.6 A. The IM model has been run in the RTS with the new moment of inertia. Fig. 4-12(b) describes the response of the phase current drawn by the PEC-based IM emulator at the no-load condition and when a step change in the load torque of 12 N.m is applied at about 1.25 s. Basically, the load torque is applied to the IM model in the RTS. The drawn current is increased due to the newly



(a)



(b)

Fig. 4-12 Experimental current response drawn by (a) the 5-hp IM during loading condition of 12 N.m at 60% of the rated voltage and (b) the IM emulator running under the same operating conditions.

required torque. The current drawn by the emulator with its current control correlates well with the current response of the real machine.

Fig. 4-13 demonstrates the phase current drawn by the PEC-based IM emulator at steady-state. The machine model is supplied by 60% of the line voltage and run under 12 N.m load torque. The current drawn by the emulator shown in Fig. 4-13(b) is compared to the current drawn by the real 5-hp induction motor shown in Fig. 4-13(a) that is running at the same operating conditions. The figure demonstrates the tracking accuracy of the developed emulator converter, in which the experimental current drawn by the IM emulator correlates well with the measured current of the real machine.

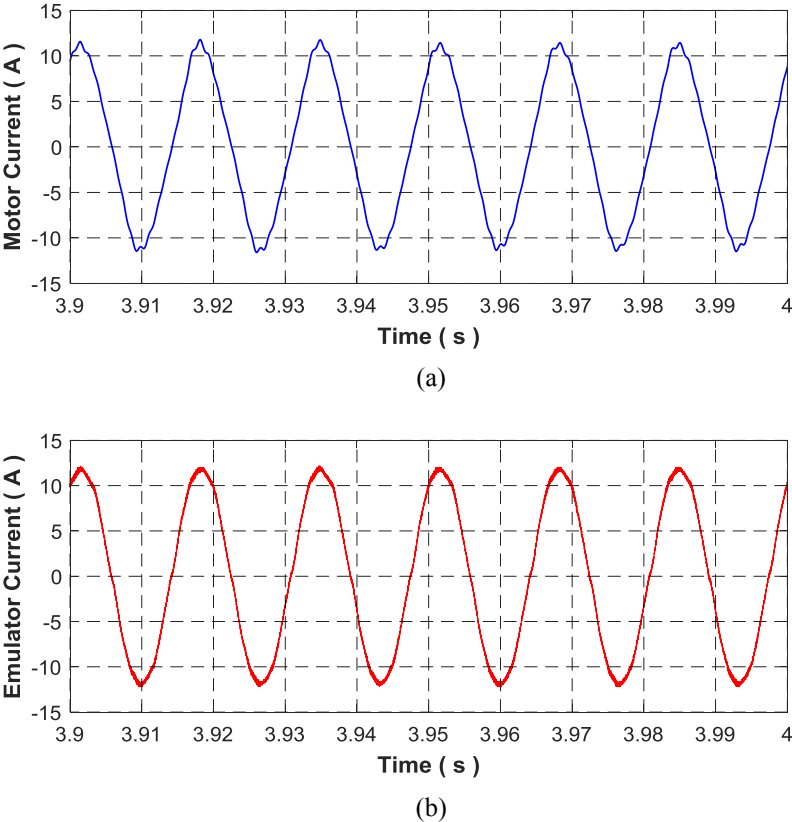


Fig. 4-13 Experimental current response drawn by (a) the 5-hp IM at steady-state with a load torque of 12 N.m and 60% of rated voltage and (b) the IM emulator running under the same operating conditions.

4.5 Summary

A failure in the control algorithm can result in a damage to both the drive and the connected machine. In this chapter, an induction motor emulator based on a power electronic converter is

developed to allow detailed testing the converter and controller. A proportional-resonant current controller with a damping factor in the abc-frame and pulse-width modulation are employed.

The mathematical model of the IM with modified parameters that is verified experimentally is employed in this chapter. The flux saturation characteristics in the main and both stator and rotor leakage flux paths have been included in the machine model to replicate accurately the IM's performance for severe transients specifically, during DOL starting and load conditions. However, this part has been detached to avoid repetition.

The developed PEC-based IM emulator has been tested experimentally during severe transients such as the DOL startup and loading transients. The dynamic response of the induction motor emulator shows the effectiveness of using the developed emulator and its control scheme to resemble closely a real induction motor.

Chapter 5. Self-Excited Induction Generator Emulator for Renewable Energy Tests within an Isolated Power System

5.1 Introduction

Induction generators have been widely employed to operate as a wind-turbine generator and small/micro-hydroelectric generator of isolated power systems or to supply additional power to a load in a remote area that is being served by a weak transmission line [78], [79]. The squirrel-cage induction generator can be operated as a self-excited induction generator (SEIG) which can be a good option for a standalone wind energy conversion system and other renewable energy sources [80], [81]. This configuration features simplicity, low capital and maintenance cost, rugged construction, and better transient performance [82]. Since the machine is not grid-connected, the terminal voltage and frequency are not fixed and the excitation should be provided by capacitors connected to the generator's terminals. The excitation capacitors could be connected in delta which results in more nearly balanced line currents [79].

Autonomous SEIGs are used to feed power for isolated loads through suitable power electronic converters [83], [84]. Moreover, proper designed power electronic interfaces are configured with SEIGs to achieve the maximum power point tracking for supplying microgrids [85], [86].

The electrical machine with its detailed design and its associated prime-mover can be replaced by solid-state devices that can be controlled and flexibly programmed in order to emulate the behavior of a real machine. An emulator is basically a power electronic interface that employs the idea of power-hardware-in-the-loop (PHIL) to offer a flexible platform for testing machines, industrial converters, conventional/novel control algorithms, and various renewable energy sources in a laboratory environment. Machine emulation is achieved by simulating the dynamic model of the required system component in a real-time simulator (RTS). The generated current and voltage commands of the model can then be used as reference signals for the rapid control prototyping (RCP) of the power converter or amplifier. The developed induction generator emulator helps in studying the dynamic performance of the standalone microgrid system when it is working in parallel with other renewable/nonrenewable generation system e.g. diesel-engine and wind/hydro generators, and when it is connected to different kinds of loads. Furthermore, it offers a safe and inexpensive testbed to study novel control schemes

for voltage and frequency regulation of a standalone induction generator for isolated power systems as in [84] and [87].

An electromechanical emulation machine platform is developed in [88] to evaluate and test the operation of a scaled down hydrokinetic turbine. A power take-off controller is used to track the maximum power point of the turbine when it is subjected to turbulence. The emulator response agrees well with the simulated results at low frequency. However, the speed response deviates when operating at higher frequencies. Various kinds of machines are emulated by utilizing the PHIL simulation for testing purposes. [24], [22], [10], and [89] are examples of the induction motor emulation for testing motor drives. The dynamic behavior of the permanent magnet synchronous generator is emulated in [90] to test the power electronic interface which controls the power flow supplied by a wind/hydrokinetic power generation system, and in [91] to test and validate the power electronic controllers and traction electrification systems. The synchronous generator emulator performance is developed in [92] for transmission power system testing and in [17] to investigate the stability of power systems dominated by parallel-operated inverters in distributed generation. However, there are few published works on the emulation of induction generators [93]. In [93], a grid-connected virtual induction generator has been built in Matlab/Simulink and used as an alternative synchronization strategy only to replace the operation of the phase-locked loop (PLL) to synchronize multiple units in a low inertia power system that is prone to fast frequency fluctuations.

In this chapter, a SEIG emulator based on a power electronic converter (PEC) has been developed. A cascaded control scheme using the proportional-integral (PI) controller in the dq-frame has been used to control the emulating converter. The mathematical model of the SEIG is implemented inside the RTS using the rotor reference frame while the saturation effect not only in the main but also in both stator and rotor leakage flux paths are included in the machine model. The excitation capacitance has been chosen to ensure an accurate operation of the PHIL and voltage buildup across the SEIG emulator terminals. To verify the generator model used in the emulation system, the predicted transient response of the voltage buildup process of the SEIG and the output loading characteristics and dynamics are compared with the real machine results. Furthermore, the dynamic response of the SEIG emulator during voltage buildup and loading conditions show the effectiveness of using the developed emulation setup to resemble closely the dynamic performance of the actual squirrel-cage induction generator.

5.2 Self-Excited Induction Generator Model with Modified Parameters

To emulate the behavior of the three-phase SEIG, an accurate mathematical model that represents its dynamics is required. The machine model which includes the saturation effect in both the main and leakage flux paths is derived in Chapter 2 and 3 and discussed in [89]. Thus, the model with modified parameters is considered in this chapter. The dynamic model of the three-phase induction generator squirrel-cage type is derived from the well-known dq-coordinate equivalent circuits shown in Fig. 5-1. The mathematical modeling is expressed in the arbitrary reference frame by a set of first-order differential equations as given in (5-1) - (5-5).

$$v_s = -R_s i_s + \frac{d\lambda_s}{dt} + K\omega\lambda_s, \quad (5-1)$$

$$v_r = R_r i_r + \frac{d\lambda_r}{dt} + K(\omega - \omega_r)\lambda_r, \quad (5-2)$$

where

$$K = \begin{bmatrix} 0 & -1 \\ 1 & 0 \end{bmatrix} \quad (5-3)$$

and $v_s = [v_{ds} \ v_{qs}]^T$ is the stator voltage vector in the dq-frame, $v_r = [v_{dr} \ v_{qr}]^T$ is the rotor voltage vector in the dq-frame which goes to zero in the case of the squirrel-cage machine, $i_s = [i_{ds} \ i_{qs}]^T$ is the stator current vector in the dq-frame, $i_r = [i_{dr} \ i_{qr}]^T$ is the rotor current vector in the dq-frame, $\lambda_s = [\lambda_{ds} \ \lambda_{qs}]^T$ is the stator flux linkage vector in the dq-frame, and $\lambda_r = [\lambda_{dr} \ \lambda_{qr}]^T$ is the rotor flux linkage vector in the dq-frame. Also, R_s and R_r are the stator and rotor resistances, respectively. ω is the electrical angular frequency of the reference frame and ω_r is the electrical angular frequency of the rotor. In this chapter, the dq-reference frame is fixed in the rotor and hence, $\omega = \omega_r$.

The flux linkage equations, which relate the stator and rotor flux linkages with stator and rotor currents, are given as follows:

$$\lambda_s = -L_{ls} i_s + L_M (i_r - i_s) + \lambda_0, \quad (5-4)$$

$$\lambda_r = L_{lr} i_r + L_M (i_r - i_s) + \lambda_0, \quad (5-5)$$

where L_M is the magnetizing inductance, L_{ls} and L_{lr} are the stator and rotor leakage inductances, respectively. These inductances are denoted by their respective reactance values given as $X = \omega L$. The residual flux linkage in the machine is denoted by $\lambda_0 = [\lambda_{d0} \ \lambda_{q0}]^T$. This term is essential to solve the differential equations and promote voltage build-up process. It has been determined experimentally by driving the generator under no-load condition from standstill to the rated speed without connecting the excitation capacitance. The line voltage and its corresponding speed have been recorded and plotted. The slope of the resulted line which represents the flux linkage is then transformed to dq-quantities to be used as input parameters for (5-4) and (5-5). The specifications of the induction machine under test and experimentally measured parameters are given in Table C-2 in Appendix - C.

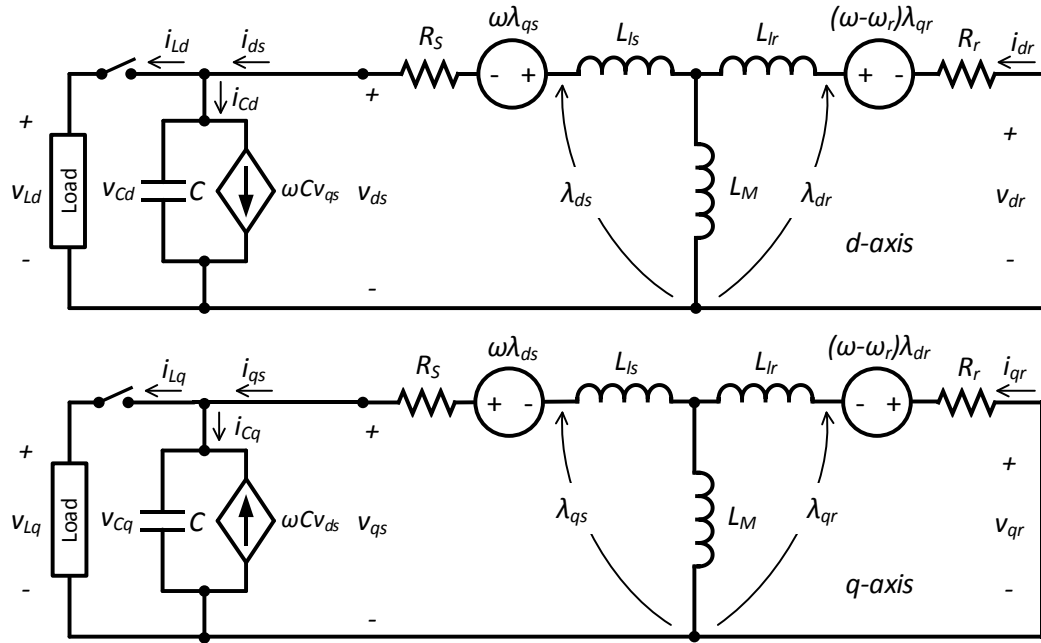


Fig. 5-1 Equivalent circuits of SEIG squirrel-cage type in the dq-coordinates and arbitrary reference frame (the 0-axis is neglected).

Assumptions for the modeling and analysis of the SEIG in this part of this work are given as follows:

- The friction and windage losses, as well as core losses are neglected.
- The effect of space harmonics in the air-gap flux and time harmonics in the electromotive force and current waveforms are neglected.
- The rotor resistance does not vary with the slip.

Both the magnetizing as well as leakage inductances depend significantly on the degree of magnetic saturation in both air-gap and machine core. The saturation effect in the main flux path and characterizing the magnetizing reactance is discussed and derived in Chapter 2. The leakage reactance in both the stator and rotor circuitry are estimated and separated using the FEM with coupled circuit according to the proposed method explained in Chapter 3. They are characterized under nominal operating condition and when the core is deeply saturated. All IM reactance parameters are then expressed by their corresponding saturation functions as follows:

$$X_{M\ sat}(I_m) = k_1 e^{-c_1 I_m} - k_2 e^{-c_2 I_m} , \quad (5-6)$$

$$X_{ls\ sat}(I_s) \cong k_3 , \quad (5-7)$$

$$X_{lr\ sat}(I_r) = k_4 e^{-c_3 I_r} + k_5 e^{-c_4 I_r} , \quad (5-8)$$

where $k_{1\ to\ 5}$, $c_{1\ to\ 4}$ are the main and leakage reactance saturation parameters, they were evaluated in Chapter 2 and modified in Chapter 3. For the sake of reference, they are listed in Table C-3 in Appendix - C. The saturation reactance parameters are updated during each calculation iteration of I_m , I_s and I_r . These currents represent the amplitude values of the magnetizing, stator and rotor currents, respectively, which are calculated and implemented in the dq-frame as the following:

$$I_m = \sqrt{(i_{qr} - i_{qs})^2 + (i_{dr} - i_{ds})^2} , \quad (5-9)$$

$$I_s = \sqrt{(i_{qs} + i_{ds})^2} , \text{ and} \quad (5-10)$$

$$I_r = \sqrt{(i_{qr} + i_{dr})^2} . \quad (5-11)$$

The abc-quantities of the voltage across the excitation capacitor and its current can be transformed into dq-frame ones. The transformed results are given as below [4]:

$$i_{cd} = C \frac{dv_{cd}}{dt} + \omega C v_{qs} = C \frac{dv_{ds}}{dt} + \omega C v_{qs} , \quad (5-12)$$

$$i_{cq} = C \frac{dv_{cq}}{dt} - \omega C v_{ds} = C \frac{dv_{qs}}{dt} - \omega C v_{ds} , \quad (5-13)$$

where i_{Cd} and i_{Cq} are the excitation capacitor current in dq-frame, v_{Cd} and v_{Cq} are the excitation capacitor voltage in dq-frame, and C is the excitation capacitance which is connected in delta with the generator terminals as an external source of reactive power.

When the generator is loaded, in this case by a resistive load, Kirchhoff's current law is used and hence, the current equations are written as follows:

$$i_L = i_s - i_C = \frac{1}{R_L} v_s, \quad (5-14)$$

where $i_L = [i_{Ld} \ i_{Lq}]^T$ is the load current vector in the dq-frame, $i_C = [i_{Cd} \ i_{Cq}]^T$ is the excitation capacitor current, and R_L is the load resistance.

The general block diagram that has been employed in this research work is shown in Fig. 5-2. (The dashed blocks and lines are used for predicted results and not implemented in the experimental work).

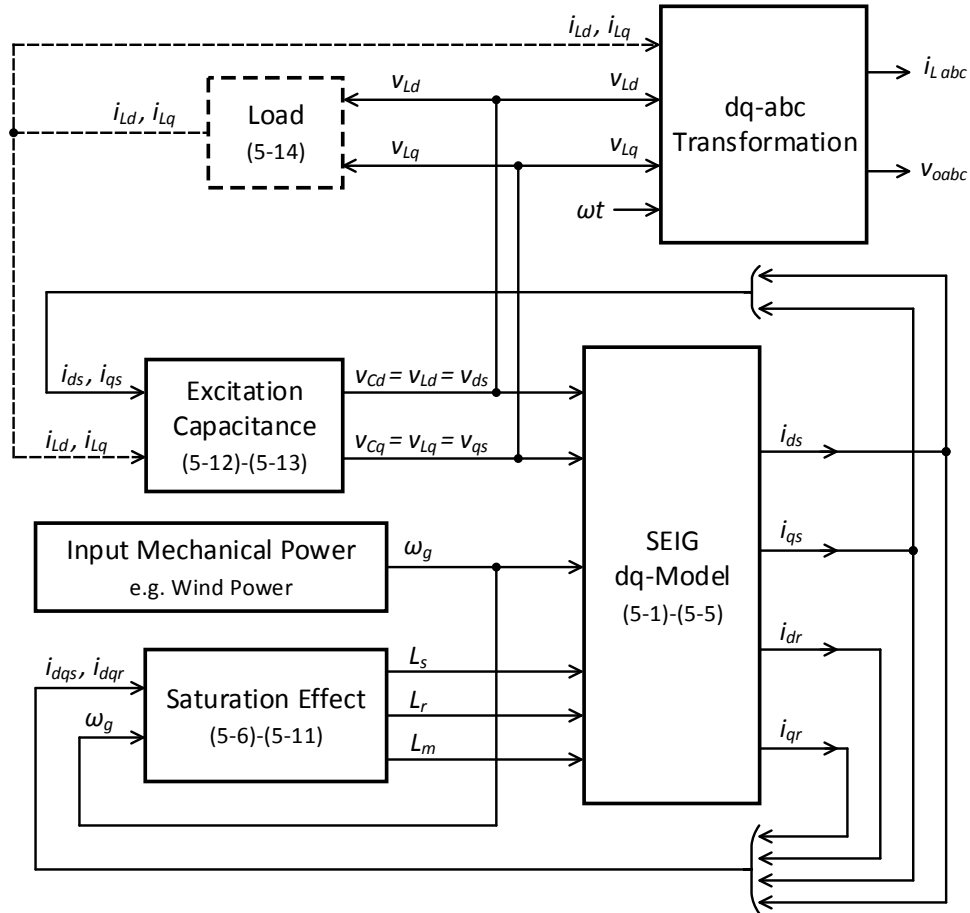


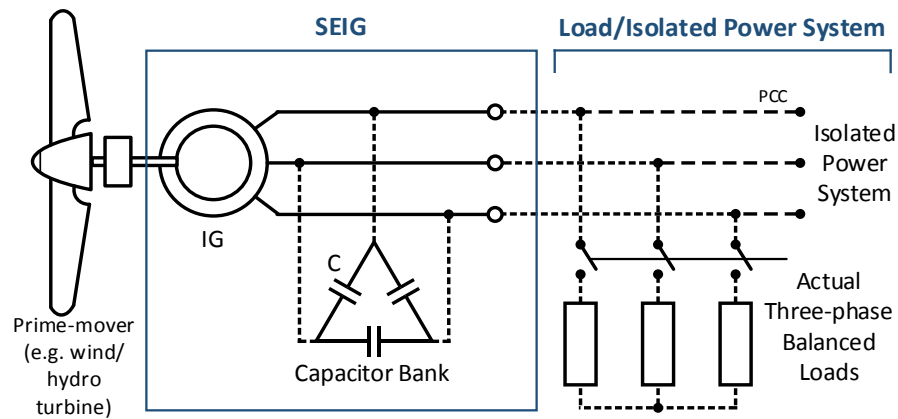
Fig. 5-2 General block diagram for the SEIG in dq-frame.

5.3 Self-Excited Induction Generator Emulator Structure

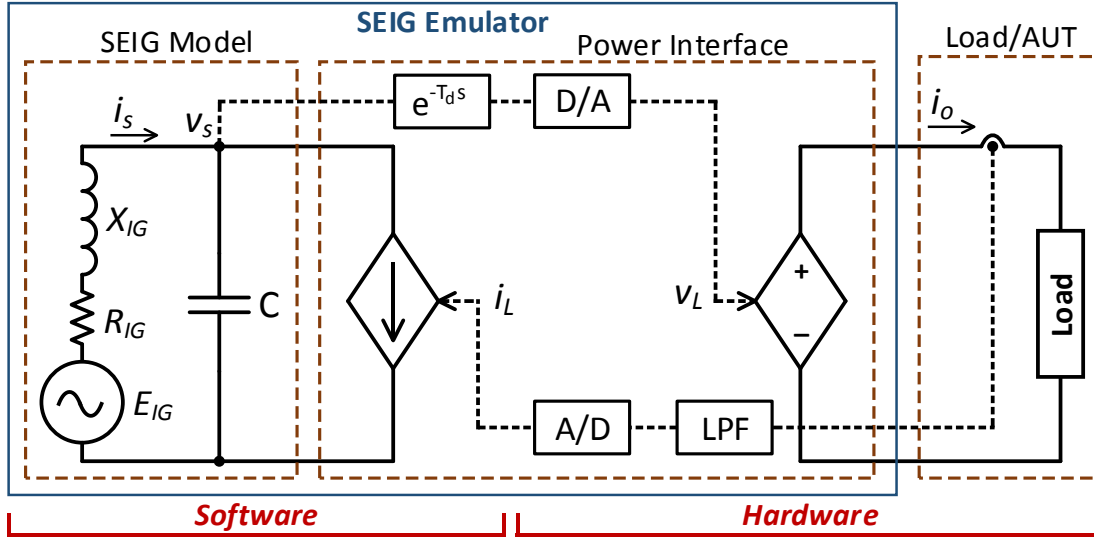
In order to replace expensive test benches and equipment as well as the risks associated with the development and testing large-scale power systems, electrical machine emulator can be used. Various kinds of electrical machines with different power ratings or conventional and advanced control strategies can be tested. This can be implemented by utilizing the concept of the PHIL along with an inclusive model of the generator and its associated prime-mover dynamics at an early stage of the design or development process.

The physical system of the SEIG which is connected to a load/islanded microgrid system is demonstrated in Fig. 5-3(a). The implementation of the PHIL-based SEIG emulation is shown in Fig. 5-3(b). It consists of three main parts: the real-time computing system in which the set of the nonlinear differential equations of the SEIG are solved, the actual load or the hardware under test, and the power interface that connects the real-time simulator (RTS) and the hardware system.

The developed emulator uses a voltage-type ideal transformer model (ITM) as a power interface with its associated interface algorithm [94], [95] as displayed in Fig. 5-3(b). In this case, the terminal voltage signal of the SEIG v_s is amplified by means of the voltage-controlled voltage source after being processed by the digital-to-analog converter (D/A). The software current-controlled current source is driven by the actual load current i_o . A current sensor, signal conditioning and an analog-to-digital converter (A/D) are employed in the feedback path. The excitation capacitance C helps building up the terminal voltage and hence, solve the SEIG's ordinary differential equations represented by (5-1) - (5-14).



(a)



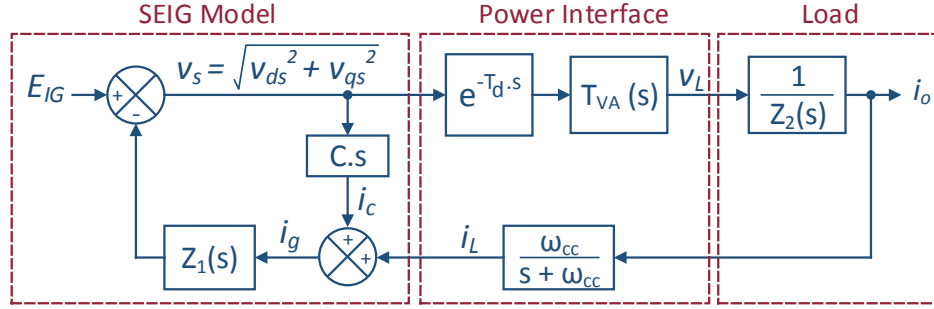
(b)

Fig. 5-3 Equivalent circuit. (a) The original system. (b) PHIL with voltage-type ITM power interface for the SEIG emulator.

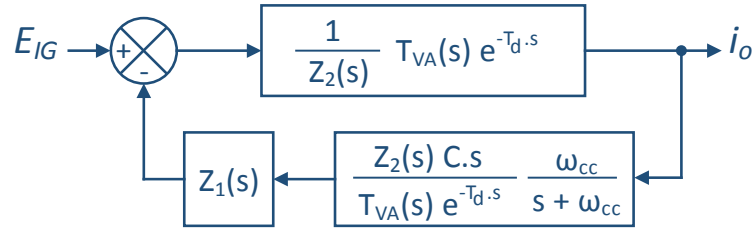
5.4 Block Diagram and Stability of the PHIL Emulation System

The signals that are exchanged between the hardware and software are the current which is measured in the hardware components and the voltage across the current source in the software side in which is computed by the real-time simulation system. The voltage amplifier is described by its transfer function $T_{VA}(s)$ that includes a delay and a low-pass filter with very high cut-off frequency. Moreover, a total time delay T_d is introduced in order to take into account the computation time of the numerical model in a discrete time of the real-time simulator, D/A, and A/D converters operation nature as well as the delay introduced by the voltage amplifier [95] and [96].

To study the stability of the PHIL implementation, the equivalent circuit of the voltage-type PHIL of Fig. 5-3(b) is represented by the block diagram shown in Fig. 5-4(a). The developed SEIG emulator consists of the SEIG model that can be represented by its back electromotive force (EMF) E_{IG} , machine stator impedance Z_1 , and the excitation capacitance C . The actual load is represented by its impedance Z_2 . A low pass filter with a cut-off frequency of 1600 Hz is employed in the current feedback path. The filter will help to ensure system stability and get rid of the high-frequency components arising due to numerical computations [94].



(a)



(b)

Fig. 5-4 Block diagram of the PHIL for the SEIG emulator. (a) Block diagram for the equivalent circuit. (b) Reduced block diagram.

To simplify the analysis of the PHIL simulation, the reduced block diagram of Fig. 5-4(b) is utilized and the time-delay expression is replaced by the first-order Padé approximation as the following:

$$e^{-T_d s} = \frac{1-ks}{1+ks}, \quad (5-15)$$

where $k = \frac{T_d}{2}$ and s is Laplace operator. Time delays due to the voltage and current sensors and PWM module are insignificant and hence, they are neglected.

The simulated impedance is the stator impedance of the machine $Z_1(s)$ while, the hardware impedance is the actual load impedance $Z_2(s)$. They are given as follows:

$$Z_1(s) = L_1 s + R_1 = L_{l_s} s + R_s, \quad (5-16)$$

$$Z_2(s) = L_2 s + R_2 = L_L s + R_L, \quad (5-17)$$

where R_L and L_L are the actual load resistance and inductance, respectively. R_s and L_{l_s} are machine parameters that discussed in Section 5.2 and tabulated in Table C-2 in Appendix - C.

The closed-loop transfer function for the reduced block diagram is derived as:

$$G_{CL}(s) = \frac{G_{VA}(s) e^{-T_d s}}{Z_2(s) + G_{VA}(s) e^{-T_d s} Z_1(s) \left[\frac{Z_2(s) C s}{G_{VA} e^{-T_d s} + s + \omega_{cc}} + \frac{\omega_{cc}}{s + \omega_{cc}} \right]}. \quad (5-18)$$

The characteristic equation of (5-18) is then calculated as follows:

$$Z_1(s) Z_2(s) C s + Z_1(s) \frac{(1-ks)}{(1+ks)} \frac{\omega_{cc}}{(s + \omega_{cc})} + Z_2(s) = 0. \quad (5-19)$$

The characteristic equation can be used to study the stability of the developed PHIL system. By substituting (5-15) - (5-17) into (5-19), one can result:

$$\begin{aligned} & \alpha k L_1 L_2 C s^5 + (k L_1 L_2 + \alpha k R_1 L_2 + \alpha k R_2 L_1 + \alpha L_1 L_2) C s^4 \\ & + (\alpha k L_2 + \alpha k R_1 R_2 C + k R_1 L_2 C + k R_2 L_1 C + \alpha R_1 L_2 C + \alpha R_2 L_1 C \\ & + L_1 L_2 C) s^3 \\ & + (\alpha k R_2 + k L_2 + \alpha L_2 + k R_1 R_2 C + \alpha R_1 R_2 C + R_1 L_2 C + R_2 L_1 C - k L_1) s^2 \\ & + (k R_2 + \alpha R_2 + L_2 + R_1 R_2 C + L_1 - k R_1) s + (R_1 + R_2) = 0, \end{aligned} \quad (5-20)$$

where $\alpha = \frac{1}{\omega_{cc}}$. For simplicity, a balanced resistive load is only considered and hence, the characteristic equation (5-20) can be approximated as follows:

$$\begin{aligned} & \alpha k R_2 L_1 C s^4 + (\alpha k R_1 R_2 + k R_2 L_1 + \alpha R_2 L_1) C s^3 \\ & + (\alpha k R_2 + k R_1 R_2 C + \alpha R_1 R_2 C + R_2 L_1 C - k L_1) s^2 \\ & + (k R_2 + \alpha R_2 + R_1 R_2 C + L_1 - k R_1) s + (R_1 + R_2) = 0. \end{aligned} \quad (5-21)$$

This clearly shows that the PHIL system will be unstable if $\alpha k R_2 + k R_1 R_2 C + \alpha R_1 R_2 C + R_2 L_1 C < k L_1$ or $k R_2 + \alpha R_2 + R_1 R_2 C + L_1 < k R_1$. These equations indicate the importance of selecting a proper value of α that reflects the filter cut-off frequency and excitation capacitance in which they place the closed-loop poles in a desirable manner and ensures voltage buildup across the generator terminals. The selected values listed in Table C-4 in Appendix - C ensure positive values of all elements of the first column of the Routh Hurwitz's array. Hence, the necessary and sufficient condition for stability is met.

5.5 Voltage Source Converter Modeling and Control

The voltage source converter (VSC) shown in Fig. 5-5 is a six-switch, two-level converter. It is controlled in such a way to emulate the SEIG. The DC side is fed by a three-phase uncontrolled rectifier. The AC side is connected to a three-phase load via an RLC coupling network that runs as a filter. Thus, the control objective is to regulate the output or load voltage $v_{o\ abc}$ and frequency to the desired reference signals. The filter is composed of an inductor L_f with an internal resistance R_f and a shunt capacitance C_f . It provides a low impedance path for switching current harmonics resulted by the pulse-width modulated output voltage and originated by the converter. The figure illustrates that the control system is implemented in the dq-frame and system variables are referred to a reference frame fixed in the rotor. Thus, abc- to dq-frame transformation is implemented when the transformation angle $\theta = \theta_r$. The angle is obtained from the electrical angular speed of the generator ω_r which is corresponding to the generator frequency as follows:

$$\theta = \theta_r = \int \omega_r(t) dt + \theta_r(0) \text{ and } \omega_r = \frac{P}{2} \omega_m, \quad (5-22)$$

where P is the number of poles of the machine and ω_m is the mechanical angular speed of the generator.

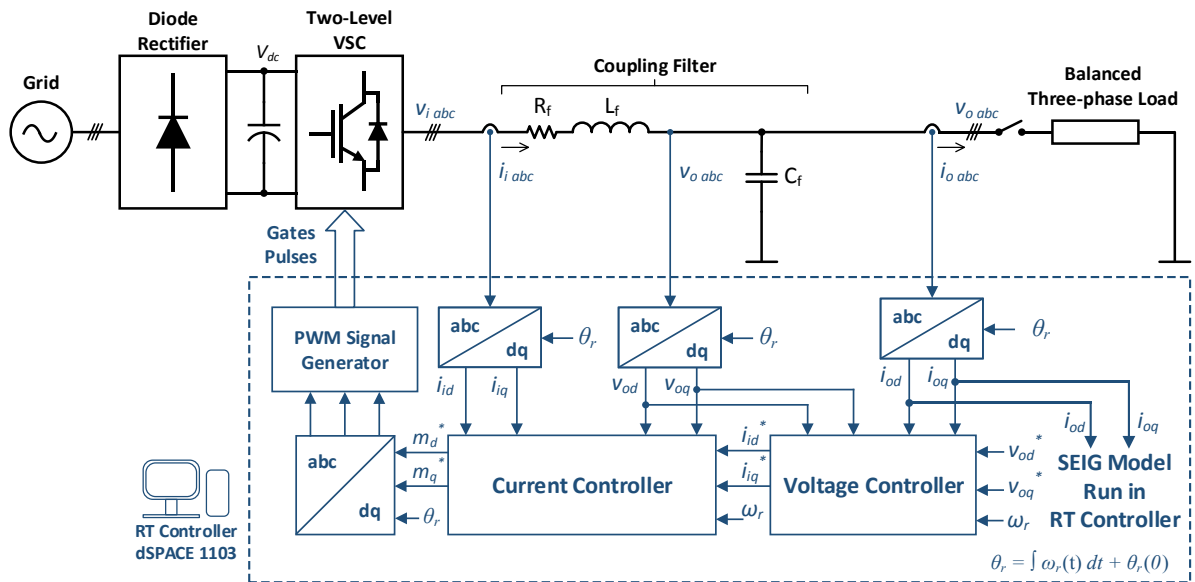


Fig. 5-5 Schematic diagram of the developed emulator with the cascaded control system.

The control procedure for the emulator is employed via a cascaded control system. The inner loop represents the current control loop while the outer loop is the voltage control loop. All control schemes are implemented inside the real-time digital system in a RCP mode. It is assumed that the VSC cascaded controllers are designed based on a balanced system and hence, the negative and zero-sequence components in dq-frame are ignored.

5.5.1 Current control scheme

The main objective of the current control scheme is to regulate the current of the AC-side of the VSC, $i_{i abc}$ by means of the pulse width modulation (PWM) switching strategy. As shown in Fig. 5-6, the control scheme is implemented in the dq-reference frame fixed in the rotor, in other words, ω is chosen to be equal to ω_r . Dynamics of the dq-frame components of $i_{i abc}$ are represented by:

$$L_f \frac{di_{id}}{dt} = -R_f i_{id} + \omega L_f i_{iq} + m_d \left(\frac{V_{dc}}{2} \right) - v_{od} , \quad (5-23)$$

$$L_f \frac{di_{iq}}{dt} = -R_f i_{iq} - \omega L_f i_{id} + m_q \left(\frac{V_{dc}}{2} \right) - v_{oq} , \quad (5-24)$$

where m_d and m_q denote the d- and q-axis components of the three-phase PWM modulating signal $m_{abc}(t)$.

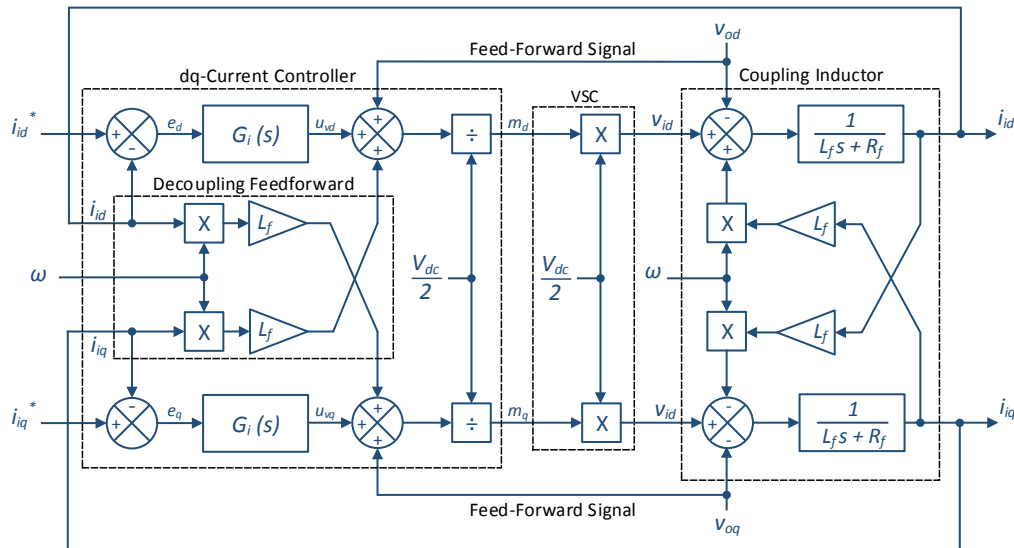


Fig. 5-6 Block diagram for the current control scheme of the SEIG emulator.

In the block diagram shown in Fig. 5-6, the current signals of the coupling inductor i_{id} and i_{iq} are controlled independently and compared to the reference currents i_{id}^* and i_{iq}^* . The desired signals in turn, are the output signals of the voltage controller. The error signals are processed by two identical proportional-integral (PI) compensators $G_i(s)$ given in (5-25). The controller outputs are then augmented with the feedforward and decoupling terms which are determined based on (5-23) and (5-24). The resulting signals are normalized to the gain of the VSC $\left(\frac{V_{dc}}{2}\right)$ in order to generate the dq-frame modulation indices m_d and m_q for the PWM gating pulse generator.

$$G_i(s) = K_{Pi} + \frac{K_{Ii}}{s} . \quad (5-25)$$

where K_{Pi} and K_{Ii} are the PI-controller gains for the current control scheme.

The control system loop gain can be found as follows:

$$\ell(s) = G_i(s) * \left(\frac{1}{L_f s + R_f} \right) = \left(\frac{K_{Pi}}{L_f s} \right) \left(\frac{s + \frac{K_{Ii}}{K_{Pi}}}{s + \frac{R_f}{L_f}} \right), \quad (5-26)$$

where R_f and L_f are the coupling inductor filter internal resistance and inductance, respectively.

The transfer function of (5-26) has a stable pole at $-\frac{R_f}{L_f}$. To improve the open-loop frequency response, the pole can be canceled by the zero of the PI compensator. Thus, choosing $\frac{K_{Ii}}{K_{Pi}} = \frac{R_f}{L_f}$ and $\frac{K_{Pi}}{L_f} = \frac{1}{\tau_i}$, where τ_i is a design choice which represents the desired time constant for the closed-loop system. Hence, the obtained transfer function of the closed-loop system is given by:

$$I_{id}(s) = H_i(s) I_{id}^*(s) = \frac{1}{\tau_i s + 1} I_{id}^*(s), \quad (5-27)$$

$$I_{iq}(s) = H_i(s) I_{iq}^*(s) = \frac{1}{\tau_i s + 1} I_{iq}^*(s), \quad (5-28)$$

which are first-order transfer functions with a unity DC gain. Since $\frac{1}{\tau_i}$ characterizes the current control bandwidth, this design parameter τ_i should be small enough to have a fast current control

response and an acceptable tracking, but adequately large such that the closed-loop bandwidth is 10 times less than the switching frequency of the converter [97].

5.5.2 Voltage control scheme

As depicted in Fig. 5-5, the output or load voltage dynamics can be described based on the voltage across the coupling capacitor C_f in the abc-frame using Kirchhoff's current law as follows:

$$C_f \frac{dv_{o\ abc}}{dt} = i_{i\ abc} - i_{o\ abc} , \quad (5-29)$$

where $i_{i\ abc}$ and $i_{o\ abc}$ are the three-phase currents of the inverter and load sides, respectively. Equation (5-29) can be represented in the dq-frame as follows:

$$C_f \frac{dv_{od}}{dt} = \omega C_f v_{oq} + i_{id} - i_{od} , \quad (5-30)$$

$$C_f \frac{dv_{oq}}{dt} = -\omega C_f v_{od} + i_{iq} - i_{oq} , \quad (5-31)$$

and re-written in the s-plan as the following:

$$C_f s V_{od}(s) = C_f \mathcal{L}\{\omega v_{oq}\} + I_{id}(s) - I_{od}(s) , \quad (5-32)$$

$$C_f s V_{oq}(s) = -C_f \mathcal{L}\{\omega v_{od}\} + I_{iq}(s) - I_{oq}(s) , \quad (5-33)$$

where $\mathcal{L}\{\cdot\}$ denotes Laplace transform operation, v_{od} and v_{oq} are the output voltages in the dq-frame, i_{id} and i_{iq} are the inverter side electric currents in the dq-frame, and the load side or output currents in dq-frame are represented by i_{od} and i_{oq} . The output voltage is represented by the voltage across the filter capacitance as shown in Fig. 5-7 and expressed by (5-32) and (5-33).

The voltage control block diagram including feedback and feedforward terms is depicted in Fig. 5-8. The output voltage control is attained by using a PI controller as:

$$G_v(s) = K_{Pv} + \frac{K_{Iv}}{s} , \quad (5-34)$$

where K_{Pv} and K_{Iv} are the PI-controller gains for the voltage control scheme.

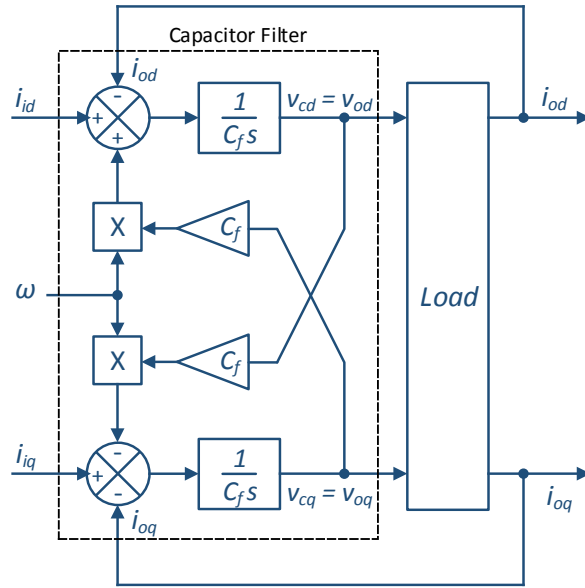


Fig. 5-7 Block diagram for the voltage across the filter capacitance the SEIG emulator.

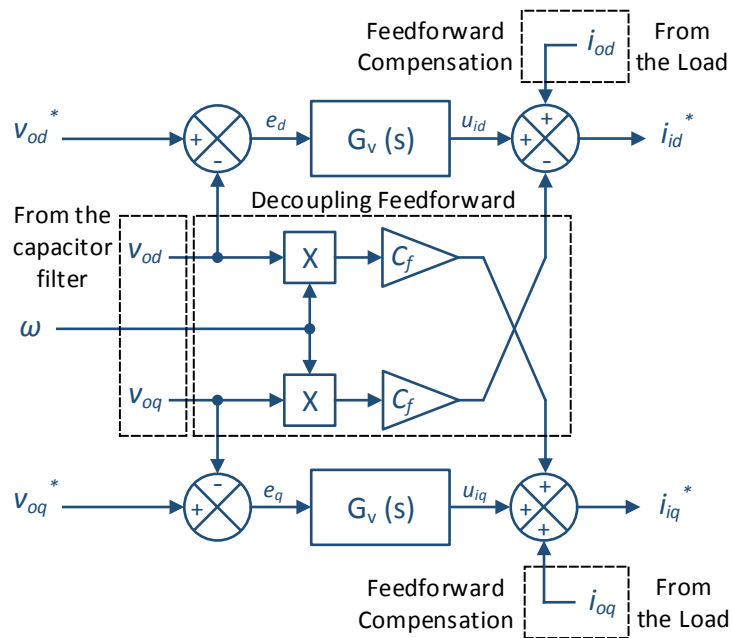


Fig. 5-8 Block diagram for the voltage control scheme of the SEIG emulator.

The reference voltage signals v_{od}^* and v_{oq}^* are set corresponding to the generator stator voltages in dq-frame, v_{sd} and v_{sq} . The reference current signals are determined in the s-domain as given in (5-35) and (5-36). A decoupling feedforward compensation is added in order to eliminate the coupling between the dq-frame output voltages v_{od} and v_{oq} [98]. Moreover, this configuration enables independent control of v_{od} and v_{oq} by i_{id}^* and i_{iq}^* , respectively. The output or load currents i_{od} and i_{oq} are included by means of a feedforward compensation scheme. Their measures are added to the reference currents i_{id}^* and i_{iq}^* as shown in Fig. 5-8. By this way, the compensated system will mitigate the impact of load dynamics on output voltages and avoid undesirable transients and hence, it will operate under all loading conditions mostly the same way as the system without compensation would perform under no-load condition [99].

$$I_{id}^*(s) = U_{id}(s) - C_f \mathcal{L}\{\omega v_{oq}\} + I_{od}(s) , \quad (5-35)$$

$$I_{iq}^*(s) = U_{iq}(s) + C_f \mathcal{L}\{\omega v_{od}\} + I_{oq}(s) , \quad (5-36)$$

where ω is the angular speed of the arbitrary reference frame which is fixed in the rotor $\omega = \omega_r$, and U_{id} and U_{iq} are current control inputs which are defined as follows:

$$U_{id}(s) = G_v * (V_{od}^*(s) - V_{od}(s)) , \quad (5-37)$$

$$U_{iq}(s) = G_v * (V_{oq}^*(s) - V_{oq}(s)) . \quad (5-38)$$

By substituting for $I_{id}^*(s)$ and $I_{iq}^*(s)$ of (5-35) and (5-36) in (5-27) and (5-28), respectively, one can result in the currents $I_{id}(s)$ and $I_{iq}(s)$. If the resulted variables are then substituted in (5-32) and (5-33), the impact of the load or output current on the output voltage can be represented as the following:

$$V_{od}(s) = A_v(s) V_{od}^*(s) + C_f B_t(s) \mathcal{L}(\omega v_{oq}) - B_t(s) I_{od}(s) , \quad (5-39)$$

$$V_{oq}(s) = A_v(s) V_{oq}^*(s) - C_f B_t(s) \mathcal{L}(\omega v_{od}) - B_t(s) I_{oq}(s) , \quad (5-40)$$

where

$$A_v(s) = \frac{H_i(s)G_v(s)}{C_f s + H_i(s)G_v(s)},$$

$$B_t(s) = \frac{[1-H_i(s)]}{C_f s + H_i(s)G_v(s)}, \text{ and } [1 - H_i(s)] = \frac{\tau_i s}{\tau_i s + 1}.$$

It is worth to mention that $A_v(s)$ is equivalent to the transfer function of the closed-loop voltage control scheme while, the transfer function $B_t(s)$ is available in the last two terms of (5-39) and (5-40). $H_i(s)$ has a unity DC gain while $[1 - H_i(s)]$ has a zero DC gain. Since the current control time constant τ_i is very small hence, $B_t(s)$ can be ignored over a wide frequency range which simplifies the controller design.

The voltage controller $G_v(s)$ is designed so that the output voltage can track the calculated reference voltage signal and ensure a fast response and zero steady-state error. Since the dq-frame is fixed in the rotor, the dq-voltages are varying at an insignificant frequency at no-load conditions that is the slip frequency. On the other hand, when it is loaded, the slip frequency will be of a few Hertz. Hence a simple PI controller as in (5-34) is employed.

The compensator design is carried out with the aid of the frequency-response or Bode plot for the open-loop transfer function calculated as in (5-41).

$$\ell(s) = H_i(s)G_v(s) \left(\frac{1}{C_f s} \right) = \frac{K_{pv}}{C_f \tau_i} \left(\frac{s+z}{s+p} \right) \frac{1}{s^2}, \quad (5-41)$$

where $z = \frac{K_{Iv}}{K_{Pv}}$ and $p = \frac{1}{\tau_i}$ are system design parameters and always $z \ll p$.

The controller parameters are chosen according to the method of symmetrical optimum [100], which is a standard design procedure for transfer functions that contain a double integration when the controller is included. The frequency response of the open-loop voltage control scheme that is represented by (5-41) is illustrated in Fig. 5-9. It shows the phase margin at the crossover frequency ω_c and the desired side frequencies ω_l and ω_h .

The unity-gain crossover frequency or system bandwidth occurs at ω_c rad/s. At frequencies lower than ω_c , the gain is maintained high while at frequencies higher than ω_c , the gain is kept low. The ratio of the two corner frequencies is given by:

$$\gamma = \frac{\omega_h}{\omega_l} = \frac{p}{z} > 1. \quad (5-42)$$

The crossover frequency is chosen as the geometric mean of the two corner frequencies. This results in a maximum phase margin and then improve the transient performance of the closed-loop system. It is determined as follows:

$$\log \omega_c = \frac{\log z + \log p}{2} \rightarrow \omega_c = \sqrt{z * p} . \quad (5-43)$$

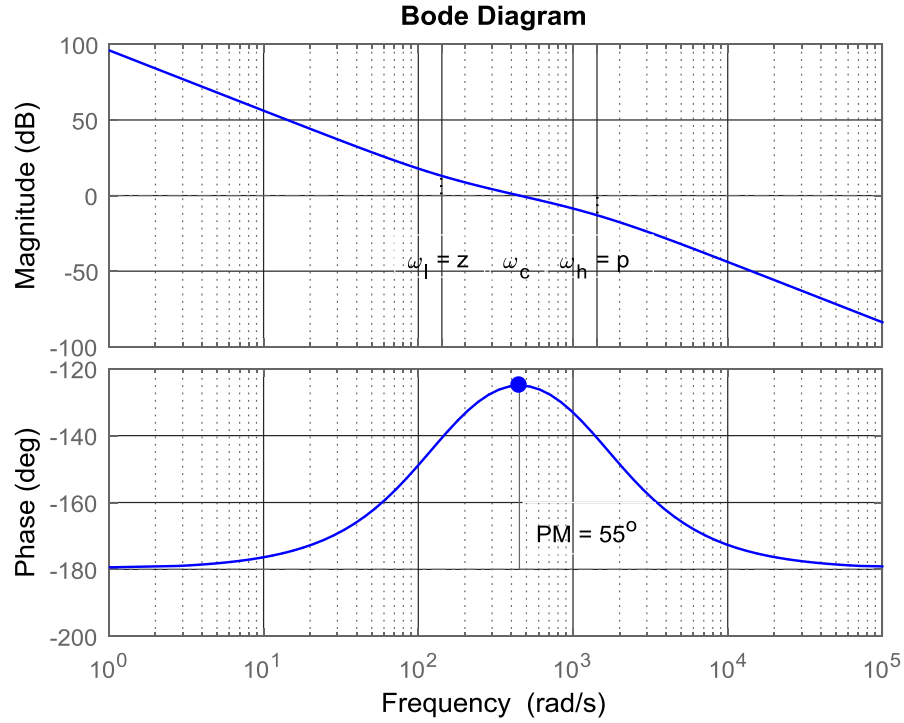


Fig. 5-9 Open-loop system Bode plot.

The expression for the phase margin is found from (5-41) to be:

$$\varphi = \tan^{-1}\omega z - \tan^{-1}\omega p . \quad (5-44)$$

The maximum phase margin is found at the frequency at which $d\varphi/d\omega = 0$ as follows:

$$\varphi_{max} = \sin^{-1}\left(\frac{\omega_h - \omega_l}{\omega_h + \omega_l}\right) = \sin^{-1}\left(\frac{p - z}{p + z}\right) = \sin^{-1}\left(\frac{\gamma - 1}{\gamma + 1}\right) . \quad (5-45)$$

Hence, the controller gain K_{pv} is obtained from the solution of $|\ell(j\omega_c)| = 1$ as follows:

$$|\ell(j\omega_c)| = \frac{K_{Pv}}{C_f \tau_i \omega_c^2} \frac{\sqrt{\omega_c^2 + z^2}}{\sqrt{\omega_c^2 + p^2}} = 1, \quad (5-46)$$

since $\omega_c \ll p$, one can obtain the gain as follows:

$$K_{Pv} = C_f \omega_c. \quad (5-47)$$

It is clear that the closed-loop voltage control system is of the third order. It has one real pole at the crossover frequency while the locations of the other two poles rely on the phase margin. A phase margin around 55° is sufficient to locate the other two poles at the same frequency of ω_c . This kind of open-loop frequency response shows its efficient tracking capabilities at low frequencies with high gain and its capability to attenuate the noise at high frequencies with low gain. The power electronic hardware data and calculated parameters for the control system are provided in Table C-4 in Appendix - C.

5.6 Experimental Results and Discussion

To investigate the effectiveness of the developed converter-based SEIG emulator and its controller capability at different operating conditions, its performance is compared with the output characteristics of the real 5-hp SEIG running at similar operating conditions. The experimental setup for the emulation system is shown in Fig. 5-10. It mainly consists of a two-level IGBT VSC from SEMIKRON [76] which runs as an emulating converter, an inductive-capacitive (LC) coupling filter, a real-time controller that runs the machine model and VSC control scheme, resistive load bank, and voltage/current sensors. The maximum capability of the developed emulator relies primarily on the VSC design which is rated at about 11 kVA and corresponds to approximately 15 hp. Meanwhile, the terminal voltage range can vary between 0-220 V and a frequency range of 0-60 Hz [76].

The induction machine model with the modified parameters including the saturation effect in both the main and leakage flux paths is implemented in MATLAB/Simulink. Furthermore, the simulation includes the excitation capacitance and the VSC control scheme. The complete Simulink file is run and built in real-time using dSPACE DS1103 controller. The fourth-order Runge-Kutta solver option with a fixed-step time is selected during simulation and code

generation. The minimum possible sampling time used to solve the differential equations related to the induction machine, the excitation capacitance and current filters is $110 \mu s$. Hence, the switching frequency of the VSC as well as the bandwidth of the control schemes are defined.

In this work, it is assumed that the generator is driven by a prime-mover in which the speed is the system input and varying with time until it reaches a constant speed. However, it can be modified as preferred since it has been added to the simulation part.

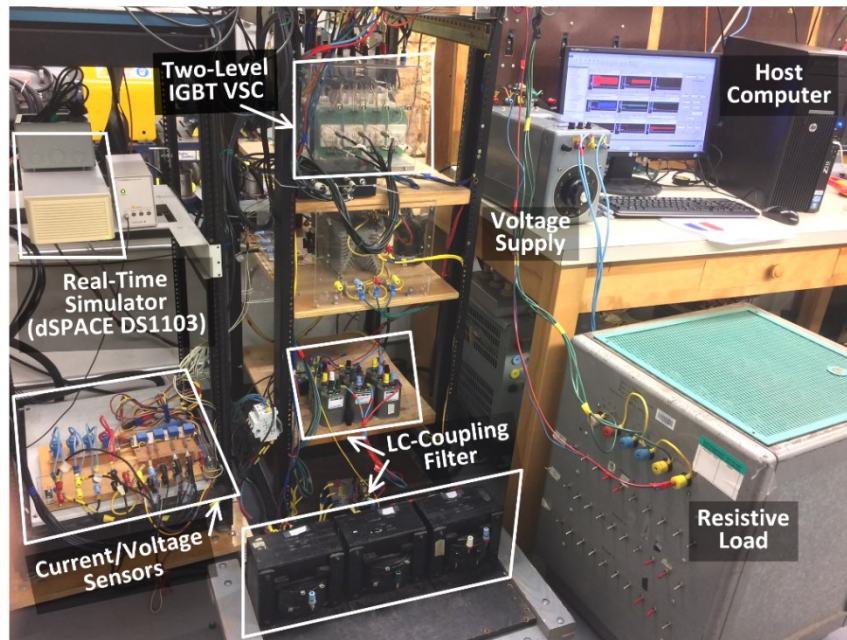
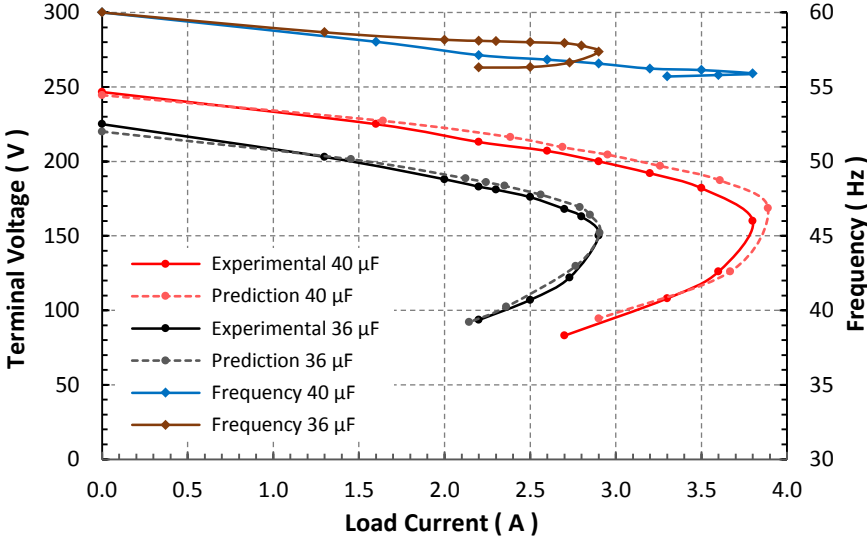


Fig. 5-10 Experimental setup for the converter-based SEIG emulator system.

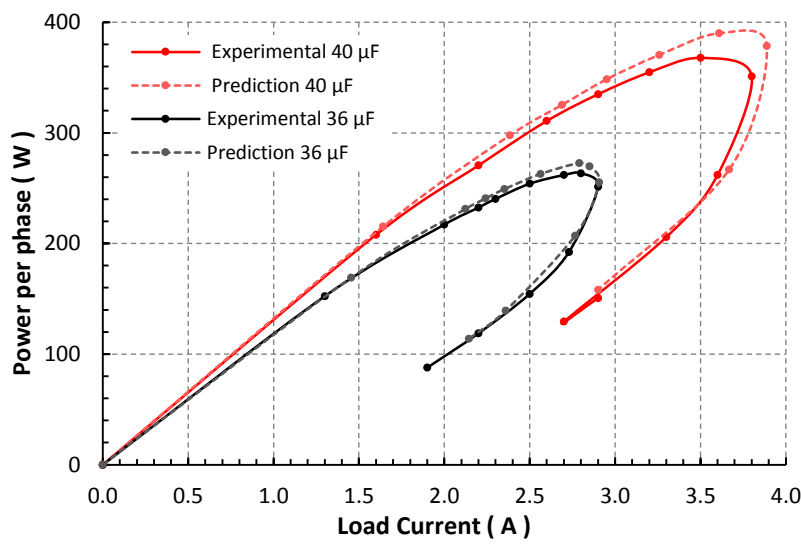
5.6.1 SEIG Model with modified parameters verification

The saturation effect in both main and leakage flux paths was implemented in the machine model. To prove the effectiveness of using the SEIG model with modified parameters, an experimental run of the real machine at no-load and loading conditions were implemented. The test results were compared with the generator model running at similar operating conditions. Fig. 5-11(a) and (b) show the load characteristics of the 5-hp SEIG indicating the variation of the terminal voltage, frequency, and power with the load current for two excitation capacitance values (36 and $40 \mu F$ per phase) and a unity power factor. As expected, terminal voltage drops with load while the load power rises then tends to reduce with excessive loading. The close agreement between the predicted and measured values for terminal voltage and power is

observed. When an excitation capacitance of 36 μF is connected to the output terminal of the generator, the frequency drops by approximately 4% from no-load to a load of about 265 W/phase while a frequency drop of almost 6% occurs at a drawn power of around 370 W/phase when a capacitance of 40 μF is connected to the generator's terminals.



(a)



(b)

Fig. 5-11 Measured and predicted output performance of the 5-hp SEIG for two different excitation capacitance values. (a) V-I output characteristics. (b) P-I output characteristics.

The dynamic response of the machine model is compared with the experimental results of a real 5-hp SEIG running under similar operating conditions. Fig. 5-12 shows the predicted dynamic response of voltage buildup process of the SEIG that considers the saturation effect in

both main and leakage flux paths under no-load condition. The excitation capacitance has been calculated from the magnetizing current characteristics at a rated voltage to be around $36 \mu\text{F}$. The speed of the prime-mover is gradually driven from standstill and to a speed of 1800 rpm within 6 s that is shown in Fig. 5-12(a). The impact of the generator speed can be noted on the output frequency of the generator. The generated sinusoidal voltage reaches its steady-state at the rated voltage and frequency after about 7 s as presented in Fig. 5-12(b). The buildup process could reduce if a larger capacitance would have been used while the terminal voltage would rise as well. The generator current shown in Fig. 5-12(c) is supplied by the excitation capacitance in order to maintain the stator magnetic field.

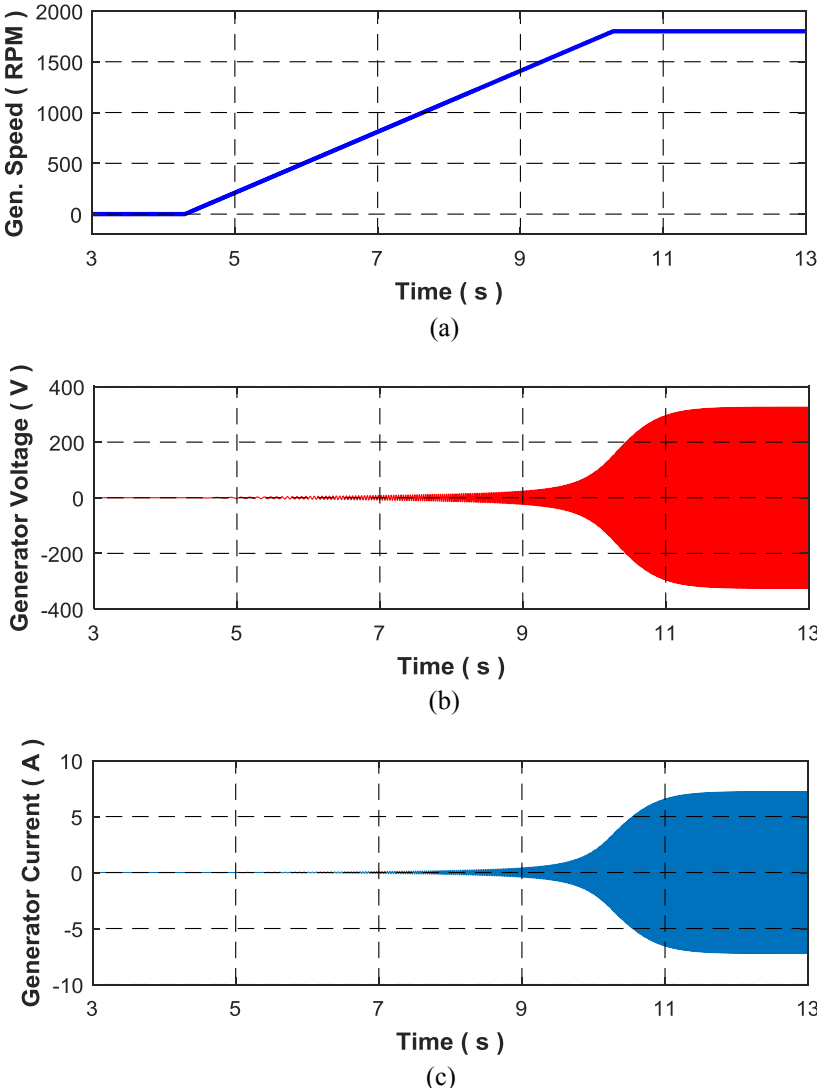


Fig. 5-12 Predicted response of the 5-hp SEIG during buildup with $C = 36 \mu\text{F}$. (a) Frequency. (b) Generator terminal voltage. (c) Generator line current.

On the other hand, the experimental results of the 5-hp SEIG running under similar operating conditions are shown in Fig. 5-13. There is a good agreement between the predicted and measured results. However, small discrepancies during the buildup process can be observed, this could be due to the inaccurate estimation of the residual flux in the machine. However, this is not the main objective of this work and hence, the SEIG model and its modified parameters can be used in the emulation system to mimic closely the dynamic and steady-state operation of a real induction generator.

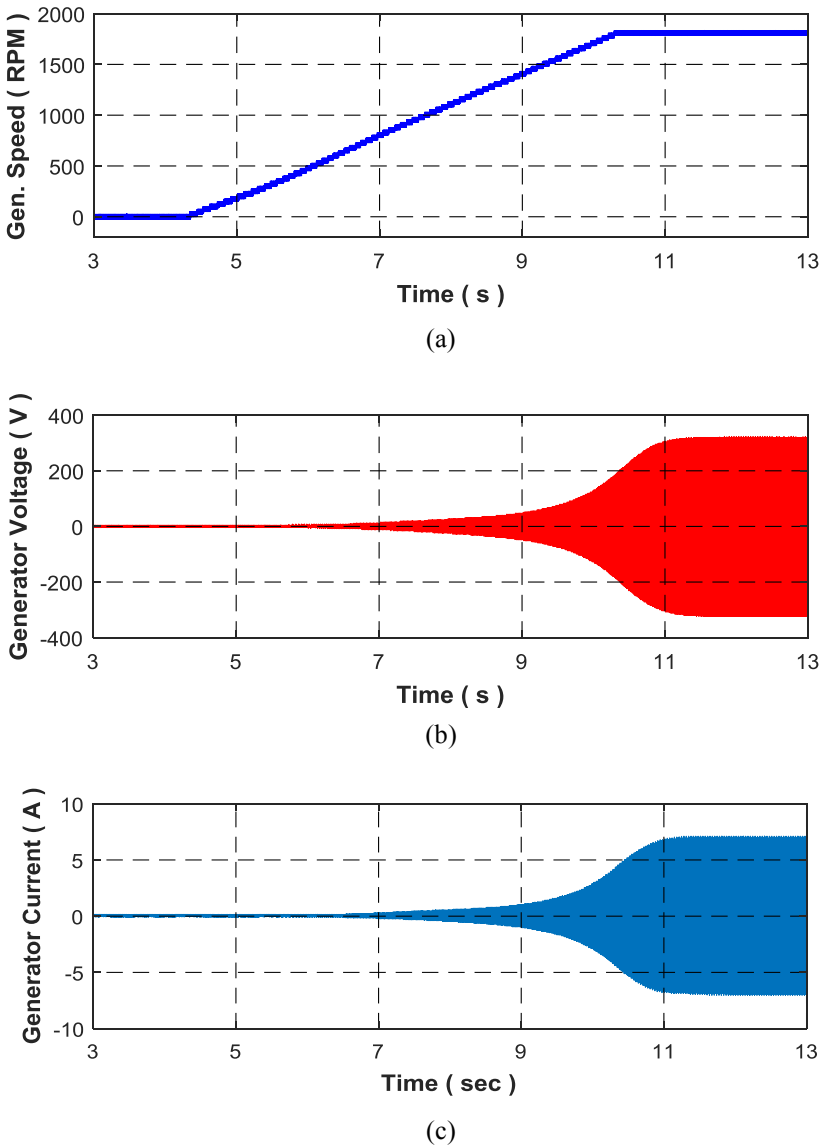
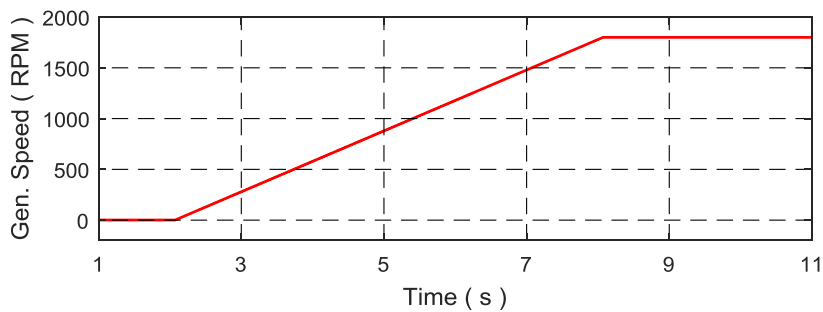


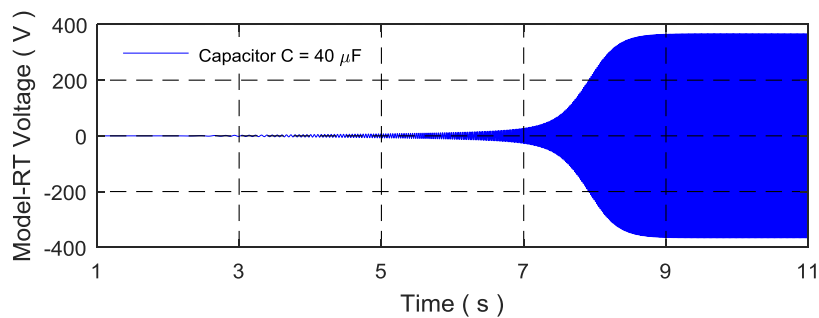
Fig. 5-13 Measured responses of real 5-hp SEIG during buildup with $C = 36 \mu\text{F}$. (a) Frequency. (b) Generator terminal voltage. (c) Generator line current.

5.6.2 SEIG emulator during voltage buildup

In order to demonstrate the effectiveness of the developed emulator with its control and to study its dynamic response, the system is used to emulate the SEIG during the voltage buildup at the no-load. The machine model with its modified parameters has been run in RTS. The generator is driven from standstill gradually to the speed of 1800 rpm as shown in Fig. 5-14(a), however, any speed profile e.g. wind, hydro, can be used. The output frequency of the generator follows its speed profile. In this part, a larger excitation capacitance of $40 \mu\text{F}$ is used and hence, the generated voltage has increased. This is observed in the terminal voltage response of the generator running in RTS in Fig. 5-14(b). Moreover, the generator's terminal voltage builds up faster, the figure shows a buildup duration of less than 6 s. The terminal voltage of the emulating converter shown in Fig. 5-14(c), replicates the generator response calculated in the RTS. Fig. 5-14(d) and (e) show zoom-in views of the emulating converter terminal voltage superimposed to the generator output voltage calculated in RT at different operation times. Fig. 5-14(d) demonstrates the case during highly dynamic buildup process at a time around 7.5 s while Fig. 5-14(e) exhibits the voltage response at steady-state operation. There is a good agreement between both responses with some ripples around the desired value. This is due to the switching frequency of the PWM technique used to switch the six power electronic devices.



(a)



(b)

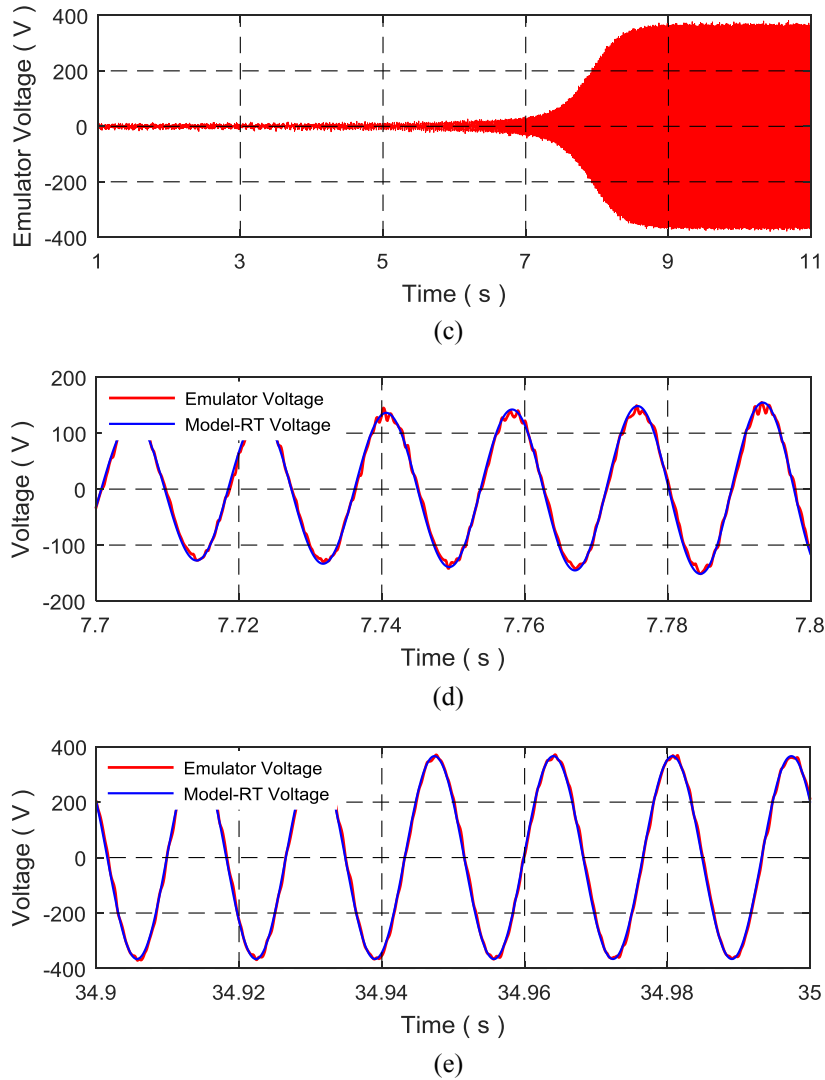


Fig. 5-14 Experimental results of the SEIG emulator buildup process at no-load with $C = 40 \mu\text{F}$; (a) output frequency, (b) generator model terminal voltage in RTS, (c) generator emulator terminal voltage, (d) a zoom-in during building up at $t = 7.7 \text{ s}$, (e) a zoom-in at steady-state at around $t = 35 \text{ s}$.

During voltage buildup and unloading condition, the generated voltage and variation of the magnetizing reactance are the primary quantities to be concerned. Fig. 5-15 demonstrates the variation of the magnetizing reactance and both stator and rotor leakage reactance parameters during voltage buildup process of the SEIG emulator. It can be noted that the value of X_m is varied from the unsaturated value about 79Ω to the saturated one about 64.5Ω during the interval corresponds to the variation of the generated voltage from transient state to its steady-state value. The rotor current is negligible at the no-load condition and hence, X_{lr} maintained constant. The reactance reduction in the main field is significant compared to the stator part in which it is considered almost constant [89].

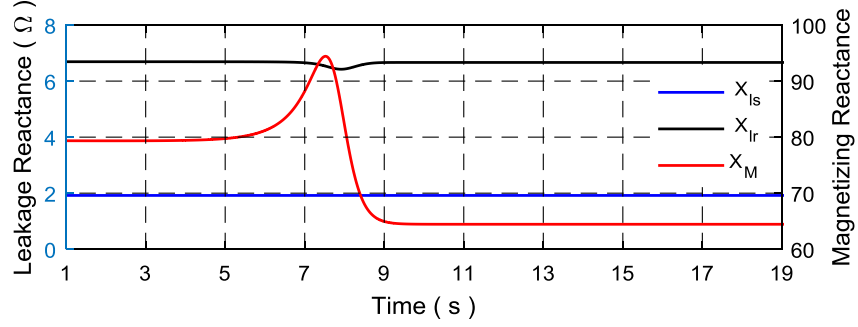
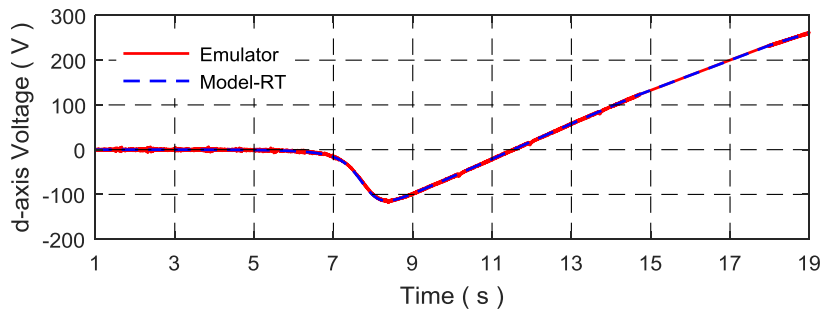


Fig. 5-15 Measured leakage and magnetizing reactance parameters variation in RT during voltage buildup at no-load condition of the SEIG emulator.

At no-load condition, the slip is insignificant which is about -0.3042×10^{-3} . Since the stationary circuit variables are referred to a reference frame fixed in the rotor ($\theta = \theta_r$) hence, the d- and q-axes terminal voltages of the SEIG emulator are varying at a very low slip frequency that is approximately equal to 18 mHz as displayed in Fig. 5-16 and represented by the Park's transformation [4]:

$$\begin{aligned} \begin{bmatrix} v_{ds} \\ v_{qs} \end{bmatrix} &= \begin{bmatrix} V_m \sin(\theta - \omega_s t) \\ V_m \cos(\theta - \omega_s t) \end{bmatrix} = \begin{bmatrix} V_m \sin(\omega_r t - \omega_s t) \\ V_m \cos(\omega_r t - \omega_s t) \end{bmatrix} \\ &= \begin{bmatrix} -V_m \sin(\omega_s - \omega_r)t \\ V_m \cos(\omega_s - \omega_r)t \end{bmatrix}. \end{aligned} \quad (5-48)$$

Furthermore, the dq-voltages measured across the terminals of the SEIG emulator are compared with the dq-voltages of the generator model calculated inside the RTS. Fig. 5-16(a) and (b) reveal a good agreement between the two responses during voltage buildup process and at the steady-state condition. Therefore the cascaded controllers using the conventional PI terms are capable to track appropriately the reference signals calculated in RT.



(a)

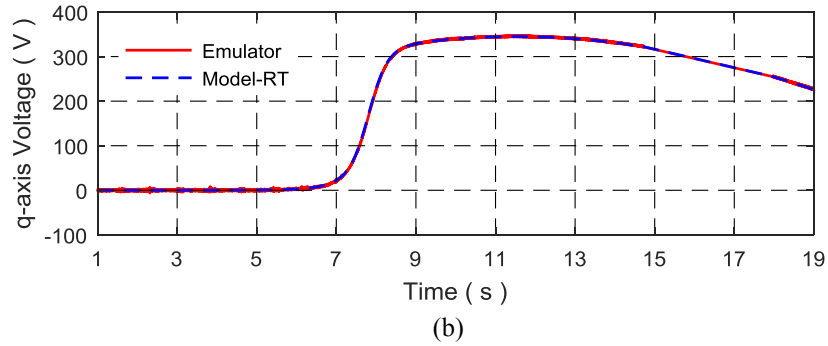


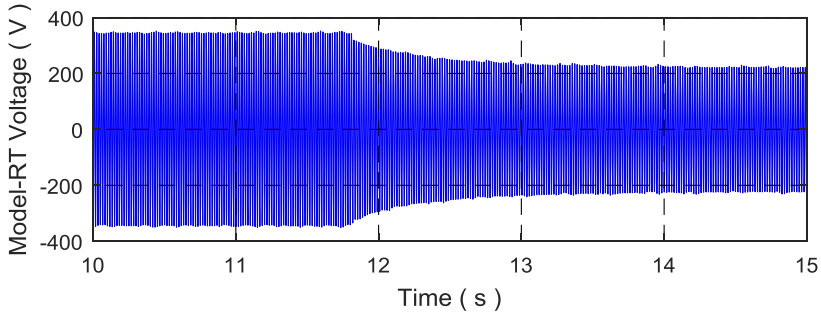
Fig. 5-16 Measured output voltage of the SEIG emulator during voltage buildup at no-load condition compared to the one calculated in RTS; (a) d-axis generator terminal voltage, (b) q-axis generator voltage.

5.6.3 SEIG emulator during loading condition

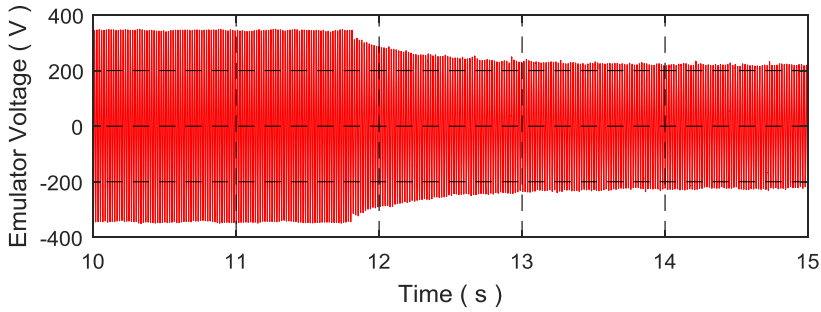
The performance of the SEIG emulator is tested during a loading circumstance and when it reaches the steady-state condition. An actual balanced three-phase wye-connected resistive load of 25Ω is connected to the terminals of the emulating converter and the real current is recorded. The SEIG emulator has been primarily driven at a speed of 1800 rpm at no-load with an excitation capacitance of $40 \mu\text{F}$. The load has been applied at around 11.8 s and the dynamic results of the SEIG emulator are compared with the response of the generator model run in real-time. Fig. 5-17(a) and (b) show respectively the dynamic responses of experimental results of the studied no-load SEIG emulator and generator model running in real-time when the emulator is subjected to a sudden connection of resistive loads. In general, a good agreement between the two responses is noted. The VSC controller is able to track the voltage reference in less than half cycle during loading as demonstrated in Fig. 5-17(c) and at the steady-state condition as shown in Fig. 5-17(d). Moreover, the figure reveals that loading causes an obvious terminal voltage drop. The feature is mainly referred to the variation in the magnetizing reactance shown in Fig. 5-18 which pushes the reactance in the main field to the unsaturated region and causes the voltage to have a significant drop. On the other hand, loading the generator causes an increase in the stator and rotor currents and hence, pushes the leakage reactance values of the machine into a deeper saturation region. The reduction in the rotor leakage part is significant compared to the stator part in which it is considered almost constant [89].

Fig. 5-17(e) shows the actual current drawn from the generator emulator. It reveals a zero current prior to load application while an inrush current is drawn at the instant of switching on the load. The load current reaches the steady-state condition after about 1.2 s.

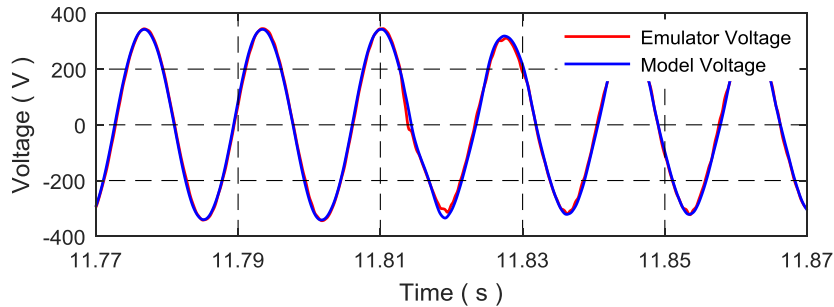
During loading, a sharp negative increase in the electromagnetic torque of the SEIG is clearly noted in Fig. 5-19(a). The rapid rise at this moment is related to a large demand of active power to be supplied by the generator. The torque is then declined gradually to reach its steady-state condition.



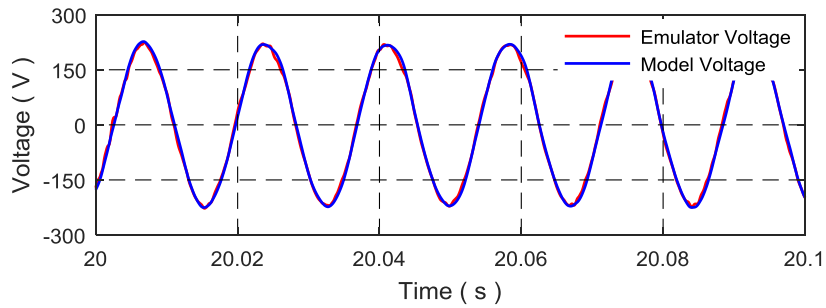
(a)



(b)



(c)



(d)

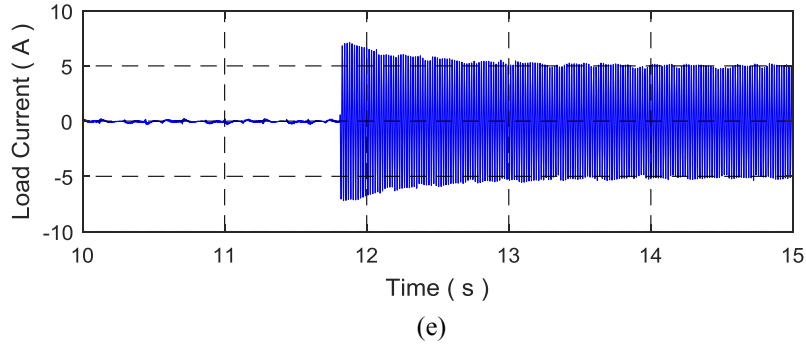


Fig. 5-17 Experimental results of the SEIG emulator during loading condition with $R_L = 25 \Omega$; (a) generator terminal voltage in RTS, (b) emulator terminal voltage, (c) zoom-in during loading condition around $t = 11.8$ s, (d) zoom-in at steady-state at around $t = 20$ s, and (e) actual load current.

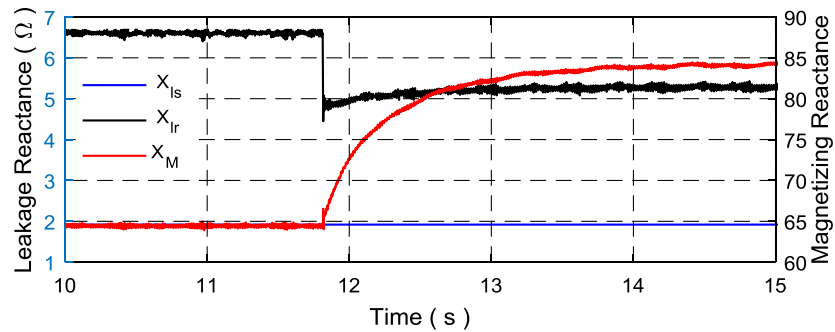
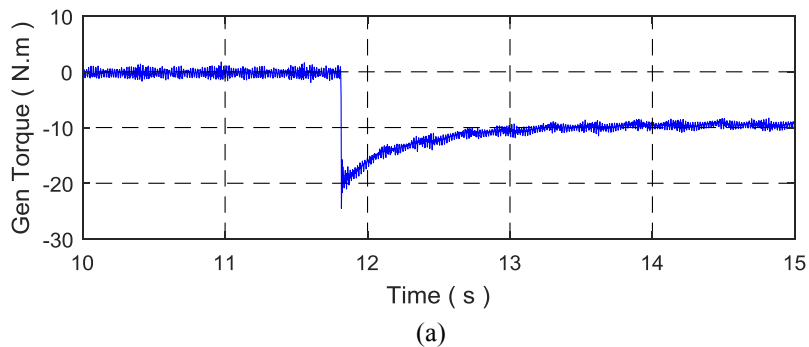
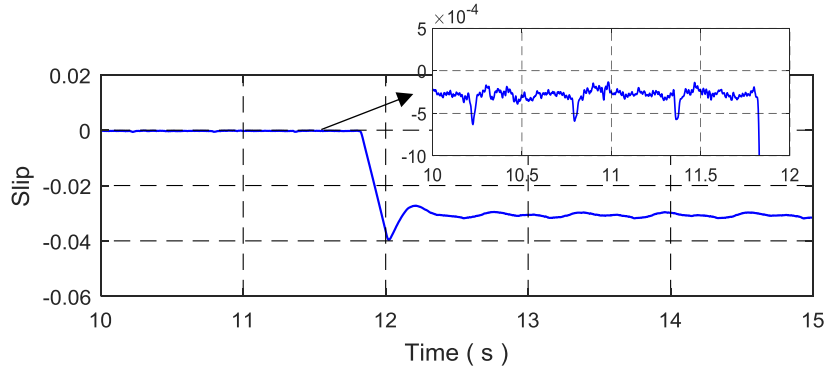


Fig. 5-18 Measured leakage and magnetizing reactance parameters variation in RT during SEIG emulator loading condition with $R_L = 25 \Omega$.

As discussed earlier, the slip at no-load condition is insignificant, $s = -0.3042 \times 10^{-3}$ as shown in Fig. 5-19(b). Hence, the dq-frame voltages of the SEIG that are calculated in RTS are varying with a very low slip frequency (approximately 18 mHz). After loading condition, the slip increases to around $s = -0.033$. Therefore, the dq-frame voltages vary as a function of the slip frequency which is in this case about 2 Hz as shown in Fig. 5-20. The controller uses a reference frame fixed in the rotor and hence, the dq-voltages are again represented by (5-48).

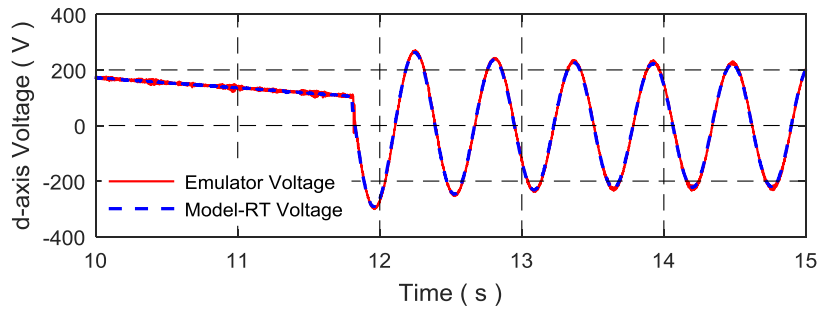




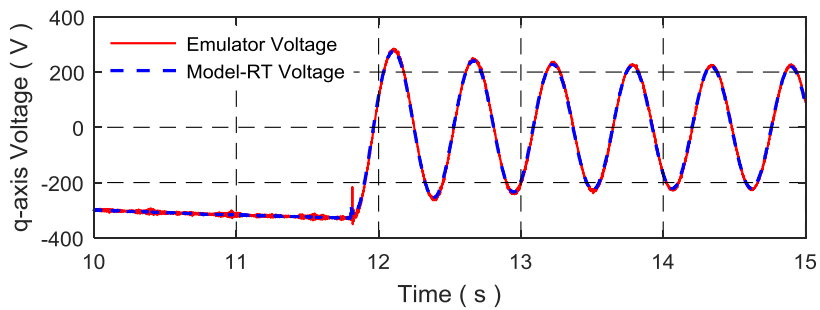
(b)

Fig. 5-19 Experimental results of the SEIG emulator during loading condition with $R_L = 25 \Omega$; (a) generator emulator torque calculated in real-time, (b) generator slip ratio.

Since the slip frequency is within the bandwidth of the designed controller of the emulator, a PI controller in the dq-coordination is quite enough to track accurately the desired voltages. To ensure the effectiveness of the control scheme used in this work, the dq-voltages measured across the emulator terminals are compared to the model variables calculated in RT. Fig. 5-20(a) and (b) reveal a good correlation between the two responses during loading condition. Hence, the developed emulator can emulate accurately the dynamic performance of a real SEIG.



(a)



(b)

Fig. 5-20 Measured output voltage of the SEIG emulator during loading condition with $R_L = 25 \Omega$ compared to the one calculated in RTS; (a) d-axis generator terminal voltage and (b) q-axis generator terminal voltage.

5.7 Summary

In this chapter, a power electronic converter-based self-excited induction generator emulator is developed. The testbed replaces a wind- or microhydro-turbine driven squirrel-cage induction generator that works within an isolated power system to feed the power in remote areas. It helps testing and analyzing the dynamic performance of an islanded microgrid generation system which comprises various kinds of parallel-operated renewable energy sources. Hence, the risk and cost associated with the testing, analysis and development of novel control topologies, electrical machine prototypes, and another renewable energy system will be considerably reduced.

The dq-model of the induction generator with modified machine reactance parameters in the rotor reference frame was implemented. The saturation effect in the main and both rotor and stator leakage flux paths were included in the machine model. The predicted response of the generator during voltage buildup was compared and verified experimentally with the response of a real 5-hp induction generator. The predicted output (V-I, f-I, and P-I) characteristics of the generator were verified experimentally with the real machine's characteristics.

The validated model was implemented in RTS and the dq-frame terminal voltages were used as reference signals for the emulating converter cascaded controller to follow. The voltage-type ideal transformer model was used as a power interface for the SEIG emulator and the excitation capacitance had been included in the PHIL simulation block diagram. The PHIL system revealed an appropriate operation especially when the time delay of the system and the current filter in the feedback path were introduced. Likewise, the dynamic performance of the SEIG emulator testbed was experimentally compared with the output response of a 5-hp SEIG-dynamometer setup. The comparison includes the transient performance during voltage buildup process at the no-load condition and when the generator terminals are connected to a balanced three-phase resistive load. The results validate the effectiveness of using the developed emulator to resemble closely a real induction generator.

Chapter 6. Conclusions and Future Work

This Ph.D. work is devoted to

- Developing a power electronic converter-based induction machine emulator which can then be used to mimic closely the dynamic performance of a real machine when it is running as a motor. This offers a flexible platform for testing and analyzing industrial converter designs and novel control algorithms in a laboratory safe environment.
- Secondly, developing a power electronic converter-based self-excited induction generator. This testbed can replace a wind- or microhydro-turbine driven squirrel-cage induction generator that works within an isolated power system to feed electric power in remote areas. Furthermore, it supports testing and analyzing the dynamic performance of islanded generation systems which comprise numerous kinds of parallel-operated renewable energy sources. Therefore, the risk and cost associated with testing, analysis and development of novel control topologies, and electrical machine prototypes are reduced significantly.

6.1 Conclusions

In **Chapter 1**, a review of different kinds of developed machine emulation in the literature showed that conventional or simplified machine models were used. The developed emulation systems were used only when the emulated machine was running at steady state or when the current drawn by the emulating converter is at low levels. The saturation effect in both main and leakage flux paths was ignored. As an attempt of increasing the power capability of the emulated machine, complicated converter structures and a large number of devices and common-mode chokes were used. This may result in different system delays, control complexity and prospective faults. The cost will also increase. Some of the developed systems showed different transients between the model and emulator. Complicated filter arrangements were used as coupling elements which results in: control topology complexity and a significant reduction in the emulation bandwidth and hence accuracy, the possibility of LC oscillation/resonance leading to stability issues, and additional losses in the damping resistances leading to a reduced emulation efficiency. Therefore, there is a necessity to develop a machine emulation system

which uses a comprehensive or detailed machine model, modest control scheme, and a simple coupling filter arrangement.

In order to have an accurate operation of the induction machine emulator and a close prediction for the machine performance, the conventional model of the induction machine with constant parameters does not represent accurately the performance of this machine with severe transients such as direct online startup and loading conditions. Hence, the magnetic saturation effects should be considered in the machine model. Therefore, experimental procedures based on IEEE Std. 112™ and IEC 60034-1 were implemented in **chapter 2** to determine the machine's leakage and main flux saturation characteristics which were then included in the dq-model. Machine models that consider or neglect the main and leakage flux saturation were compared with experimental results. The model which considers the magnetic saturation effect in both flux paths results in more accurate transient response calculations.

The relationship between the stator and rotor leakage reactance of the induction machine according to IEEE Std. 112™ is assumed to be constant under all operating conditions. However, this is not substantially accurate during severe transients such as the direct online startup and loading conditions of a three-phase induction motor. The reactance in the main and leakage flux paths of the induction machine can vary widely during severe conditions. Hence, using constant parameters in the machine model will result in an inaccurate dynamic performance prediction and significant errors may occur when designing the control scheme. Moreover, considering a constant ratio between the stator and rotor leakage reactance is no longer valid for all current levels. Therefore, a direct and precise method utilizing a 2D FEM with coupled circuit was proposed in **chapter 3**. It estimates and separates the stator and rotor leakage reactance parameters under normal operating conditions and when the core is deeply saturated. The dq-model of the machine with newly modified parameters was compared to the dynamic responses obtained experimentally from a three-phase, 5-hp squirrel-cage induction motor. Results acknowledged considering the effect of the current-dependent X_{ls}/X_{lr} ratio on the performance of the induction machine.

In **chapter 4**, the developed induction motor emulator which used the induction machine model with modified parameters was tested. The measured responses and comparison results verified the effectiveness of using the emulation system to resemble closely the dynamic response of an actual motor specifically during severe transient and steady-state conditions. The

PR-current controller in the abc-frame showed its ability in eliminating the steady-state error with time-varying reference signals close to the grid frequency. However, it is still weak when frequency changes. A possible method to mitigate this concern was achieved by inserting a damping factor as discussed in this chapter. For variable frequency applications, it is required that the resonant frequency of the PR-controller is continuously adjusted to match the output fundamental frequency.

As discussed in **Chapter 5**, an interface algorithm is essential to link the software and hardware. It can be implemented using numerous methods available in the literature, leading to different degrees of accuracy and system stability for the PHIL simulation. However, the ideal transformer model (ITM) method is simple to implement and highly accurate. Therefore, it was implemented in this work and its stability was also guaranteed for most generator operating conditions. During the no-load condition of the SEIG emulator, the slip was insignificant. Hence, the dq-frame voltages of the SEIG calculated in real-time vary at a very low slip frequency $s \approx -0.3 \times 10^{-3}$. After loading, the slip increased to around $s = -0.033$. Therefore, the dq-frame voltages varied as a function of the slip frequency of 2 Hz. Since the controller used a reference frame fixed in the rotor and the slip frequency was within the bandwidth of the designed controller of the emulator, a PI controller in the dq-frame was quite enough to track accurately the desired voltages and hence, the developed emulator could emulate closely the real SEIG operation and its dynamic performance.

6.2 Future Work

Improvements and prospective research works are addressed based on the acquired experiences throughout this work as follows:

- It is difficult to separate and measure the end-winding leakage field independently from the leakage field in the machine core. Therefore, in this work, the comparison of the obtained results with the measured data was accomplished in terms of the total stator leakage reactance instead of considering the end-winding leakage reactance separately. To mitigate the discrepancies between the FEM model and experimental results during startup, a more accurate end-winding reactance can be estimated by using a three-dimensional FEM. Its updated value can be connected the coupled circuit in FEM software.

- The developed induction motor emulator can be expanded by adding a third two-level converter which can be controlled to run as a driving converter. Different speed control techniques such as V/f, direct torque control, and other novel control schemes can be tested. Higher power capability emulating converter can be used to extend the voltage and current capabilities of the emulated induction machine. Hence, the DOL startup can be implemented at full-voltage. Moreover, a higher bandwidth converter would produce lower current ripples when the emulator converter is running at no-load conditions or low drawn current values. Modifying the PR-controller scheme so it can work with variable frequency applications.
- The developed induction generator emulator can be tested for different electrical loads such as nonlinear loads (uncontrolled and controlled rectifiers). Furthermore, it can be used to emulate a fault on output terminals or on one of the capacitance.

References

- [1] International Energy Agency, Key world energy statistics 2015. [Online]. Available: <http://www.iea.org/publications/freepublications/publication/key-world-energy-statistics-2015>.
- [2] International Energy Agency, Energy efficiency for electric systems. [Online]. Available: https://www.iea.org/publications/freepublications/publication/EE_for_ElectricSystems.
- [3] International Energy Agency, Energy technology perspectives 2012. [Online]. Available: <http://www.iea.org/publications/freepublications/publication/energy-technology-perspectives-2012>.
- [4] P. Krause, O. Wasynczuk, S. Sudhoff and S. Pekarek, Analysis of Electric Machinery and Drive Systems, 2nd ed., IEEE Press, John Wiley & Sons, Inc., 2013.
- [5] R. J. Lee, P. Pillay and R. G. Harley, "D,q reference frames for simulation of induction motors," *Electric Power System Research*, vol. 8, pp. 15-26, 1984/85.
- [6] R. Krishnan, Electric Motor Drives Modeling, Analysis and Control, Prentice Hall, 2001.
- [7] B. Belvedere, M. Bianchi, A. Borghetti, C. A. Nucci, M. Paolone and A. Peretto, "A microcontroller based power management system for standalone micro-grids with hybrid power supply," *IEEE Trans. Sustain. Energy*, vol. 3, no. 3, pp. 422-431, Jul. 2012.
- [8] R. Solomon, M. A. Khan, P. S. Barendse, P. Pillay and K. A. Folly, "Review and application of micromachines for wind energy integration," in *Inter. Conf. Electrical Machines (ICEM)*, Marseille, Sep. 2012, pp. 2151-2157.
- [9] L. Yang, Y. Ma, J. Wang, J. Wang, X. Zhang, L. M. Tolbert, F. Wang and K. Tomsovic, "Development of converter based reconfigurable power grid emulator," in *IEEE Energy Conversion Congr. Expo. (ECCE)*, Pittsburgh, PA, Sep. 2014, pp. 3990-3997.
- [10] O. Vodyakho, M. Steurer, C. Edrington and F. Fleming, "An induction machine emulator for high-power applications utilizing advanced simulation tools with graphical user interfaces," *IEEE Trans. Energy Convers.*, vol. 27, no. 1, pp. 160-172, Mar. 2012.
- [11] J. Wang, Y. Ma, L. Yang, L. M. Tolbert and F. Wang, "Power converter-based three-phase induction motor load emulator," in *Annu. IEEE Applied Power Electronics Conf. Expo.*, Long Beach, CA, Mar. 2013, pp. 3270-3274.
- [12] H. J. Slater, D. J. Atkinson and A. G. Jack, "Real-time emulation for power equipment development. Part 2: The virtual machine," *IEE Proc. Elect. Power Applicat.*, vol. 145, no. 3, pp. 153-158, May 1998.
- [13] S. Grubic, B. Amlang, W. Schumacher and A. Wenzel, "A high performance electronic hardware-in-the-loop drive-load simulation using a linear inverter (LinVerter)," *IEEE Trans. Ind. Electron.*, vol. 57, no. 4, pp. 1208-1216, Apr. 2010.
- [14] M. Armstrong, D. J. Atkinson, A. G. Jack and S. Turner, "Power system emulation using a real time, 145 kW, virtual power system," in *Proc. Eur. Conf. Power Electron. Appl.*, Dresden, Sep. 2005, pp. 1-10.

- [15] S. Lentijo, S. D'Arco and A. Monti, "Comparing the dynamic performances of power hardware-in-the-loop interfaces," *IEEE Trans. Ind. Electron.*, vol. 57, no. 4, pp. 1195-1207, Apr. 2010.
- [16] M. Torres and L. A. C. Lopes, "Inverter-based virtual diesel generator for laboratory-scale applications," in *Proc. IEEE-IECON*, Glendale, AZ, Nov. 2010, pp. 532-537.
- [17] Q. Zhong and G. Weiss, "Synchronverters: inverters that mimic synchronous generators," *IEEE Trans. Ind. Electron.*, vol. 58, no. 4, pp. 1259-1267, Mar. 2011.
- [18] A. D. Paquette, M. J. Reno, R. G. Harley and D. M. Divan, "Transient load sharing between inverters and synchronous generators in islanded microgrids," in *IEEE Energy Conversion Congr. Expo. (ECCE)*, Raleigh, NC, Sep. 2012, pp. 2753-2742.
- [19] L. Yang, X. Zhang, Y. Ma, J. Wang, L. Hang, K. Lin, L. M. Tolbert, F. Wang and K. Tomsovic, "Hardware implementation and control design of generator emulator in multi-converter system," in *Annu. IEEE Applied Power Electronics Conf. Expo.*, Long Beach, CA, Mar. 2013, pp. 2316-2323.
- [20] M. Kesler, E. Ozdemir, M. C. Kisacikoglu and L. M. Tolbert, "Power converter-based three-phase nonlinear load emulator for a hardware testbed system," *IEEE Trans. Power Electron.*, vol. 29, no. 11, pp. 5806-5812, Nov. 2014.
- [21] J. Wang, L. Yang, Y. Ma, X. Shi, X. Zhang, L. Hang and K. Lin, "Regenerative power converters representation of grid control and actuation emulator," in *IEEE Energy Conversion Congr. Expo. (ECCE)*, Raleigh, NC, Sep. 2012, pp. 2460-2465.
- [22] J. Wang, L. Yang, Y. Ma, J. Wang, L. M. Tolbert, F. Wang and K. Tomsovic, "Static and dynamic power system load emulation in converter-based reconfigurable power grid emulator," *IEEE Trans. Power Electron.*, vol. 31, no. 4, pp. 3239-3251, Apr. 2016.
- [23] J. Wang, L. Yang, Y. Ma, J. Wang, L. M. Tolbert, F. Wang and K. Tomsovic, "Static and dynamic power system load emulation in converter-based reconfigurable power grid emulator," in *IEEE Energy Conversion Congr. Expo. (ECCE)*, Pittsburgh, PA, Sep. 2014, pp. 4008-4015.
- [24] M. Steurer, C. S. Edrington, M. Sloderbeck, W. Ren and J. Langston, "A megawatt-scale power hardware-in-the-loop simulation setup for motor drives," *IEEE Trans. Ind. Electron.*, vol. 57, no. 4, pp. 1254-1260, 2010.
- [25] B. Liu, S. Zheng, Y. Ma, F. Wang and L. M. Tolbert, "Control and implementation of converter based ac transmission line emulation," in *IEEE Applied Power Electronics Conf. Expo.*, Charlotte, NC, Mar. 2015, pp. 1807-1814.
- [26] Y. S. Rao and M. Chandorkar, "Real-time electrical load emulator using optimal feedback control technique," *IEEE Trans. Ind. Electron.*, vol. 57, no. 4, pp. 1217-1225, Apr. 2010.
- [27] Y. S. Rao and M. Chandorkar, "Electrical load emulation using power electronic converters," in *TENCON IEEE Region 10 Conf.*, Hyderabad, Nov. 2008, pp. 1-6.
- [28] D. S. L. Dolan, "Real-time wind turbine emulator suitable for power quality and dynamic control studies," M.Sc. Thesis, Department of Electrical and Computer Engineering, University of Toronto, Apr. 2005.

- [29] L. A. C. Lopes, J. Lhuilier, A. Mukherjee and M. F. Khokar, "A wind turbine emulator that represents the dynamics of the wind turbine rotor and drive train," in *Proc. IEEE Conf. Power Electronics Specialists*, Recife, Jun. 2005, pp. 2092–2097.
- [30] M. Monfared, H. M. Kojabadi and H. Rastegar, "Static and dynamic wind turbine simulator using a converter controlled dc motor," *Renewable Energy*, vol. 33, no. 5, pp. 906-913, May 2008.
- [31] Y. Ma, L. Yang, J. Wang, F. Wang and L. M. Tolbert, "Emulating full-converter wind turbine by a single converter in a multiple converter based emulation system," in *Annu. IEEE Applied Power Electronics Conf. Expo. (APEC)*, Fort Worth, TX, Mar. 2014, pp. 3042-3047.
- [32] W. Cao, Y. Ma, J. Wang, L. Yang, J. Wang, F. Wang and L. M. Tolbert, "Two-stage PV inverter system emulator in converter based power grid emulation system," in *IEEE Energy Conversion Congr. Expo. (ECCE)*, Denver, CO, Sep. 2013, pp. 4518-4525.
- [33] W. Cao, Y. Ma, J. Wang and F. Wang, "Virtual series impedance emulation control for remote PV or wind farms," in *Annu. IEEE Applied Power Electronics Conf. Expo. (APEC)*, Fort Worth, TX, Mar. 2014, pp. 411-418.
- [34] *IEEE Standard Test Procedure for Polyphase Induction Motors and Generators*, IEEE Std 112™, IEEE Power and Energy Society, 2017.
- [35] *Rotating Electrical Machines - Part 1: Rating and Performance*, IEC 60034-1, Edition 11.0, 2004.
- [36] T. A. Lipo and A. Consoli, "Modeling and simulation of induction motors with saturable leakage reactances," *IEEE Trans. Ind. Appl.*, Vols. IA-20, no. 1, pp. 180-189, Jan. 1984.
- [37] P. Vas, "Generalized analysis of saturated AC machines," *Archiv für Elektrotechnik*, vol. 64, no. 1, pp. 57-62, Jan. 1981.
- [38] P. Run-hao, Z. Haisen, Z. Dongdong and L. Jiakuan, "Analytical method for starting performance calculation of induction motors considering skin effect and leakage flux saturation," in *Int. Conf. Electrical Machines and Systems (ICEMS)*, Hangzhou, China, Oct. 2014, pp. 135-138.
- [39] D. C. Aliprantis, S. D. Sudhoff and B. T. Kuhn, "Experimental characterization procedure for a synchronous machine model with saturation and arbitrary rotor network representation," *IEEE Trans. Energy Convers.*, vol. 20, no. 3, pp. 595-603, Sep. 2005.
- [40] H. M. Jabr and N. C. Kar, "Starting performance of saturated induction motors," in *Proc. IEEE Power Eng. Soc. General Meeting*, Jun. 2007, pp. 1-7.
- [41] J. Pedra, I. Candela and A. Barrera, "Saturation model for squirrel-cage induction motors," *Elsevier Elect. Power Sys. Research*, vol. 79, no. 7, pp. 1054-1061, Jul. 2009.
- [42] M. H. Jabr and N. C. Kar, "Leakage flux saturation effects on the transient performance of wound-rotor induction motors," *Elsevier Elect. Power Sys. Research*, vol. 78, no. 7, pp. 1280-1289, Jul. 2008.
- [43] A. Tessarolo, "Leakage field analytical computation in semiclosed slots of unsaturated electric machines," *IEEE Trans. Energy Convers.*, vol. 30, no. 2, pp. 431-440, Jun. 2015.
- [44] I. Kiraly and D. Zarko, "Extended space vector method for calculation of induction motor parameters," *Electric Power Components and Systems*, vol. 44, no. 8, pp. 928-940, Apr. 2016.

- [45] Z. Ling, L. Zhou, S. Guo and Y. Zhang, "Equivalent circuit parameters calculation of induction motor by finite element analysis," *IEEE Trans. Magn.*, vol. 50, no. 2, pp. 833-836, Feb. 2014.
- [46] K. Yamazaki, A. Suzuki, M. Ohto, T. Takakura and S. Nakagawa, "Equivalent circuit modeling of induction motors considering stray load loss and harmonic torques using finite element method," *IEEE Trans. Magn.*, vol. 47, no. 5, pp. 986-989, May 2011.
- [47] A. Tessarolo, S. Mohamadian and M. Bortolozzi, "A new method for determining the leakage inductances of a nine-phase synchronous machine from no-load and short-circuit tests," *IEEE Trans. Energy Convers.*, vol. 30, no. 4, pp. 1515-1527, Dec. 2015.
- [48] S. D. Sudhoff, D. C. Aliprantis, B. T. Kuhn and P. L. Chapman, "Experimental characterization procedure for use with an advanced induction machine model," *IEEE Trans. Energy Convers.*, vol. 18, no. 1, pp. 48-56, Mar. 2003.
- [49] Mentor, a Siemens Business, *MagNet 7.8*, 2D/3D Electromagnetic Field Simulation Software, Wilsonville, OR, USA, 2018.
- [50] P. A. Bastos and N. Sadowski, *Electromagnetic Modeling by Finite Element Methods*, NY: Marcel Dekker, 2003.
- [51] S. J. Salon, *Finite Element Analysis of Electrical Machines*, Springer Science+Business Media New York, 1995.
- [52] P. Zhou, J. Gilmore, Z. Badics and Z. J. Cendes, "Finite element analysis of induction motors based on computing detailed equivalent circuit parameters," *IEEE Trans. Magn.*, vol. 34, no. 5, pp. 3499-3502, Sep. 1998.
- [53] *Rotating Electrical Machines - Part 4: Methods for determining synchronous machine quantities from tests*, IEC 60034-4, Edition 3.0, 2008.
- [54] D. Ban, D. Zarko and I. Mandic, "Turbogenerator end-winding leakage inductance calculation using a 3-D analytical approach based on the solution of Neumann Integrals," *IEEE Trans. Energy Convers.*, vol. 20, no. 1, pp. 98-105, Mar. 2005.
- [55] Mentor, a Siemens Business, *MotorSolve 6.0.1*, Electric Machine Design Software, Wilsonville, OR, USA, 2018.
- [56] S. Seman, J. Saitz and A. Arkkio, "Dynamic model of cage induction motor considering saturation and skin effect," in *Int. Conf. Electrical Machines and Systems*, Beijing, China, Nov. 2003, pp. 710-713.
- [57] Mentor, a Siemens Business, *MagNet Live Docs*, 2018. [Online]. Available: <https://www.mentor.com/products/mechanical/magnet/magnet/>. [Accessed Sep. 2018].
- [58] M. A. Masadeh and P. Pillay, "Induction motor emulation including main and leakage flux saturation effects," in *IEEE Int. Electric Machines and Drives Conference (IEMDC)*, Miami, FL, USA, May 2017.
- [59] D. Ronanki, S. A. Singh and S. S. Williamson, "Comprehensive Topological Overview of Rolling Stock Architectures and Recent Trends in Electric Railway Traction Systems," *IEEE Trans. Transport. Electrific.*, vol. 3, no. 3, pp. 724-738, Sep. 2017.

- [60] E. Bostanci, M. Moallem, A. Parsapour and B. Fahimi, "Opportunities and challenges of switched reluctance motor drives for electric propulsion: a comparative study," *IEEE Trans. Transport. Electrification*, vol. 3, no. 1, pp. 58-75, Mar. 2017.
- [61] G. Sulligoi, A. Vicenzutti and R. Menis, "All-electric ship design: from electrical propulsion to integrated electrical and electronic power systems," *IEEE Trans. Transport. Electrification*, vol. 2, no. 4, pp. 507-521, Dec. 2016.
- [62] Z. Yang, F. Shang, I. P. Brown and M. Krishnamurthy, "Comparative study of interior permanent magnet, induction, and switched reluctance motor drives for EV and HEV applications," *IEEE Trans. Transport. Electrification*, vol. 1, no. 3, pp. 245-254, Oct. 2015.
- [63] V. Nguyen, D. Wang, J. Seshadrinath, A. Ukil, M. S. Krishna, S. Nadarajan and V. Vaiyapuri, "A method for incipient interturn fault detection and severity estimation of induction motors under inherent asymmetry and voltage imbalance," *IEEE Trans. Transport. Electrification*, vol. 3, no. 2, pp. 703-715, Sep. 2017.
- [64] F. Blaabjerg, R. Teodorescu, M. Liserre and A. V. Timbus, "Overview of control and grid synchronization for distributed power generation systems," *IEEE Trans. Ind. Electron.*, vol. 53, no. 5, pp. 1398-1409, Oct. 2006.
- [65] M. Bhardwaj, "Software phase locked loop design using C2000TM Microcontrollers for three phase grid connected applications," Texas Instruments SPRABT4A, Nov. 2013.
- [66] N. Mohan, T. M. Undeland and W. P. Robbins, *Power Electronics: Converters, Applications, and Design*, 3rd ed., John Wiley & Sons, Inc., 2003.
- [67] M. Liserre, F. Blaabjerg and S. Hansen, "Design and control of an LCL-filter-based three-phase active rectifier," *IEEE Trans. Ind. Appl.*, vol. 41, no. 5, pp. 1281-1291, Sep./Oct. 2005.
- [68] Y. Sato, T. Ishizuka, K. Nezu and T. Kataoka, "A new control strategy for voltage-type PWM rectifiers to realize zero steady-state control error in input current," *IEEE Trans. Ind. Appl.*, vol. 34, no. 3, pp. 480-486, May/Jun. 1998.
- [69] A. Kuperman, "Proportional-resonant current controllers design based on desired transient performance," *IEEE Trans. Power Electron.*, vol. 30, no. 10, pp. 5341-5345, Oct. 2015.
- [70] D. Stanciu and M. Teodorescu, "Zero steady-state error PWM control system for sinusoidal voltage," in *Int. Symp. Advanced Topics in Electrical Engineering (ATEE)*, Bucharest, May 2015, pp. 656-661.
- [71] X. Yuan, W. Merk, H. Stemmler and J. Allmeling, "Stationary-frame generalized integrators for current control of active power filters with zero steady-state error for current harmonics of concern under unbalanced and distorted operating conditions," *IEEE Trans. Ind. Appl.*, vol. 38, no. 2, pp. 523-532, Mar./Apr. 2002.
- [72] A. K. Adapa and V. John, "Active phase-converter for operation of three-phase induction motors on single-phase grid," *IEEE Trans. Ind. Appl.*, vol. 0, no. 99, pp. 1-1, Aug. 2017.
- [73] A. Timbus and M. Liserre, "Evaluation of current controllers for distributed power generation systems," *IEEE Trans. Power Electron.*, vol. 24, no. 3, pp. 654-664, Mar. 2009.
- [74] D. N. Zmood and D. G. Holmes, "Stationary frame current regulation of PWM inverters with zero steady-state error," *IEEE Trans. Power Electron.*, vol. 18, no. 3, pp. 814-822, May 2003.

- [75] OPAL-RT TECHNOLOGIES, Inc., [Online]. Available: <https://www.opal-rt.com/simulator-platform-op4510/>. [Accessed Oct. 2017].
- [76] SEMIKRON, [Online]. Available: <http://www.shop.semikron.com/en/Products-and-Shop/Product-Groups/STACKs/SEMITEACH/SEMITEACH-B6U-E1CIF-B6CI.html>. [Accessed Jan. 2018].
- [77] J. S. S. Prasad, T. Bhavsar, R. Ghosh and G. Narayanan, "Vector control of three-phase AC/DC front-end converter," *Sadhana*, vol. 33, no. 5, pp. 591-613, Oct. 2008.
- [78] K. Arthishri, K. Anusha, N. Kumaresan and S. S. Kumar, "Simplified methods for the analysis of self-excited induction generators," *IET Electr. Power Appl.*, vol. 11, no. 9, pp. 1636 - 1644, Nov. 2017.
- [79] G. McPherson and R. D. Laramore, *An Introduction to Electrical Machines and Transformers*, John Wiley & Sons, Inc., 1990.
- [80] R. Bansal, "Three-phase self-excited induction generators: an overview," *IEEE Trans. Energy Convers.*, vol. 20, no. 2, pp. 292-299, Jun. 2005.
- [81] M. G. Simoes and F. A. Farret, *Modeling and Analysis with Induction Generators*, Broken Sound Parkway, NW: CRC Press, Taylor & Francis Group, 3rd Edition, 2015.
- [82] V. Yaramasu, B. Wu, P. C. Sen, S. Kouro and M. Narimani, "High-power wind energy conversion systems: state-of-the-art and emerging technologies," *Proc. IEEE*, vol. 103, no. 5, p. 740-788, May 2015.
- [83] L. Wang and D.-J. Lee, "Coordination control of an AC-to-DC converter and a switched excitation capacitor bank for an autonomous self-excited induction generator in renewable-energy systems," *IEEE Trans. Ind. Appl.*, vol. 50, no. 4, pp. 2828-2836, Aug. 2014.
- [84] L. G. Scherer, R. V. Tambara and R. F. d. Camargo, "Voltage and frequency regulation of standalone self-excited induction generator for micro-hydro power generation using discrete-time adaptive control," *IET Renewable Power Generation*, vol. 10, no. 4, pp. 531-540, Apr. 2016.
- [85] S. S. Kumar, N. Kumaresan and M. Subbiah, "Analysis and control of capacitor-excited induction generators connected to a micro-grid through power electronic converters," *IET Gener. Transmiss. Distrib.*, vol. 9, no. 10, pp. 911-920, Jun. 2015.
- [86] V. Nayanar, N. Kumaresan and N. A. Gounden, "A single-sensor-based MPPT controller for wind-driven induction generators supplying DC microgrid," *IEEE Trans. Power Electron.*, vol. 31, no. 2, pp. 1161-1172, Feb. 2016.
- [87] U. K. Kalla, B. Singh, S. S. Murthy, C. Jain and K. Kant, "Adaptive sliding mode control of standalone single-phase microgrid using hydro, wind and solar PV array based generation," *IEEE Trans. Smart Grid*, vol. DOI: 10.1109/TSG.2017.2723845, Jul. 2017.
- [88] R. J. Cavagnaro, J. C. Neely, F.-X. Fa, J. L. Mendia and J. A. Rea, "Evaluation of electromechanical systems dynamically emulating a candidate hydrokinetic turbine," *IEEE Trans. Sustain. Energy*, vol. 7, no. 1, pp. 390-399, Jan. 2016.
- [89] M. A. Masadeh, K. S. Amitkumar and P. Pillay, "Power electronic converter-based induction motor emulator including main and leakage flux saturation," *IEEE Trans. Transport. Electrific.*, vol. 4, no. 2, pp. 483-493, Jun. 2018.

- [90] M. Ashourianjozdani, L. A. C. Lopes and P. Pillay, "Power electronic converter-based PMSG emulator: a testbed for renewable energy experiments," *IEEE Trans. Ind. Appl.*, Mar. 2018.
- [91] R. S. Kaarthik, K. S. Amitkumar and P. Pillay, "Emulation of a permanent-magnet synchronous generator in real-time using power hardware-in-the-loop," *IEEE Trans. Transport. Electrific.*, vol. 4, no. 2, pp. 474-482, Jun. 2018.
- [92] L. Yang, J. Wang, Y. Ma, J. Wang, X. Zhang, L. M. Tolbert, F. F. Wang and K. Tomsovic, "Three-phase power converter-based real-time synchronous generator emulation," *IEEE Trans. Power Electron.*, vol. 32, no. 2, pp. 1651-1665, Feb. 2017.
- [93] U. Markovic, P. Aristidou and G. Hug, "Virtual induction machine strategy for converters in power systems with low rotational inertia," in *Proc. 10th Bulk Power Systems Dynamics and Control Symp.*, Espinho, Portugal, Sep. 2017.
- [94] G. Lauss, F. Lehfuß, A. Viehweider and T. Strasser, "Power hardware in the loop simulation with feedback current filtering for electric systems," in *37th Annual Conf. of the IEEE Ind. Electron. Society IECON*, Melbourne, Australia, Nov. 2011.
- [95] W. Ren, M. Steurer and T. L. Baldwin, "Improve the stability and the accuracy of power hardware-in-the-loop simulation by selecting appropriate interface algorithms," *IEEE Trans. Ind. Appl.*, vol. 44, no. 4, pp. 1286-1294, Jul./Aug. 2008.
- [96] M. Hong, S. Horie, Y. Miura, T. Ise and C. Dufour, "A method to stabilize a power hardware-in-the-loop simulation of inductor coupled systems," in *Int. Conf. on Power Systems Transients IPST*, Kyoto, Japan, Jun. 2009.
- [97] M. A. Zamani, A. Yazdani and T. S. Sidhu, "A control strategy for enhanced operation of inverter-based microgrids under transient disturbances and network faults," *IEEE Trans. Power Del.*, vol. 27, no. 4, pp. 1737-1747, Oct. 2012.
- [98] N. Pogaku, M. Prodanovic and T. C. Green, "Modeling, analysis and testing of autonomous operation of an inverter-based microgrid," *IEEE Trans. Power Electron.*, vol. 22, no. 2, pp. 613-625, Mar. 2007.
- [99] A. Yasdani and R. Iravani, *Voltage-Sourced Converters in Power Systems: Modeling, Control, and Applications*, Hoboken, New Jersey: John Wiley & Sons, Inc., 2010.
- [100] W. Leonhard, *Control of Electrical Drives*, Springer-Verlag Berlin Heidelberg, 3rd Edition, 2001.

Appendix - A

abc/dq Coordinates Transformation

A change of variables that formulates a transformation of the three-phase *abc*-coordinate variables of a stationary circuit elements to the *dqo*-arbitrary reference frame coordinate is expressed as the following formula [4]:

$$f_{dq0} = T f_{abc} \quad (\text{A-1})$$

where

$$f_{dq0} = \begin{bmatrix} f_d \\ f_q \\ f_0 \end{bmatrix} \text{ and } f_{abc} = \begin{bmatrix} f_a \\ f_b \\ f_c \end{bmatrix} \quad (\text{A-2})$$

The transformation matrix when the rotating frame is aligned 90° behind the stator a-axis, is given as follows:

$$T = \frac{2}{3} \begin{bmatrix} \sin \omega t & \sin \left(\omega t - \frac{2\pi}{3} \right) & \sin \left(\omega t + \frac{2\pi}{3} \right) \\ \cos \omega t & \cos \left(\omega t - \frac{2\pi}{3} \right) & \cos \left(\omega t + \frac{2\pi}{3} \right) \\ \frac{1}{2} & \frac{1}{2} & \frac{1}{2} \end{bmatrix} \quad (\text{A-3})$$

The inverse transformation is given as follows:

$$f_{abc} = T^{-1} f_{dq0} \quad (\text{A-4})$$

where

$$T^{-1} = \begin{bmatrix} \sin \omega t & \cos \omega t & 1 \\ \sin \left(\omega t - \frac{2\pi}{3} \right) & \cos \left(\omega t - \frac{2\pi}{3} \right) & 1 \\ \sin \left(\omega t + \frac{2\pi}{3} \right) & \cos \left(\omega t + \frac{2\pi}{3} \right) & 1 \end{bmatrix} \quad (\text{A-5})$$

Appendix - B

LCL Transfer Function

Equations (4-3) - (4-6) can be re-written in s-domain as follows:

$$I_i(s) = I_C(s) + I_f(s) , \quad (\text{B-1})$$

$$V_i(s) = V_{PCC}(s) + (L_i s + R_i)I_i(s) , \quad (\text{B-2})$$

$$V_{PCC}(s) - V_o(s) = (L_f s + R_f)I_f(s) , \quad (\text{B-3})$$

$$V_{PCC}(s) = \frac{R_d C_f s + 1}{C_f s} I_C(s) . \quad (\text{B-4})$$

For filter analysis, v_i is considered as a disturbance signal and hence $v_i = 0$, (B-2) becomes:

$$V_{PCC}(s) = -(L_i s + R_i)I_i(s) . \quad (\text{B-5})$$

By equating (B-4) and (B-5):

$$V_{PCC}(s) = \frac{R_d C_f s + 1}{C_f s} I_C(s) = -(L_i s + R_i)I_i(s) , \quad (\text{B-6})$$

I_C can be calculated as follows:

$$I_C(s) = -\frac{L_i C_f s^2 + R_i C_f s}{R_d C_f s + 1} I_i(s) . \quad (\text{B-7})$$

By substituting (B-7) in (B-1), one can get:

$$I_i(s) = \frac{R_d C_f s + 1}{L_i C_f s^2 + (R_i + R_d)C_f s + 1} I_f(s) . \quad (\text{B-8})$$

If (B-5) is substituted in (B-3), one can get:

$$V_o(s) = -(L_i s + R_i)I_i(s) - (L_f s + R_f)I_f(s) , \quad (\text{B-9})$$

And then, (B-8) is substituted in (B-9) to get:

$$\begin{aligned} V_o(s) &= \left[\frac{-R_d L_i C_f s^2 - (L_i + R_i R_d C_f) s - R_i}{L_i C_f s^2 + (R_i + R_d)C_f s + 1} - (L_f s + R_f) \right] I_f(s) \\ &= \frac{-L_i L_f C_f s^3 - (R_d L_i + R_f L_i + R_i L_f + R_d L_f) C_f s^2 - (L_i + L_f + R_i R_d C_f + R_i R_f C_f + R_d R_f C_f) s - (R_i + R_f)}{L_i C_f s^2 + (R_i + R_d)C_f s + 1} I_f(s) \end{aligned}$$

Hence, the transfer function of the whole coupling filter can be described as follows:

$$\begin{aligned} H_f(s) &= \frac{I_f(s)}{V_o(s)} \\ &= \frac{L_i C_f s^2 + (R_i + R_d)C_f s + 1}{-L_i L_f C_f s^3 - (R_d L_i + R_f L_i + R_i L_f + R_d L_f) C_f s^2 - (L_i + L_f + R_i R_d C_f + R_i R_f C_f + R_d R_f C_f) s - (R_i + R_f)} \quad (\text{B-10}) \end{aligned}$$

Appendix - C

System Parameters and Specifications

Table C-1 IM under test specifications and some design parameters

Three-phase, 5-hp, 220 V, 60 Hz, 16 A, 1730 rpm, C-Class, Δ -Connected squirrel-cage induction motor			
Parameter	Value	Parameter	Value
Stator outer diameter	188 mm	No. of poles	4
Stator inner diameter	109 mm	No. of stator slots	36
Rotor outer diameter	108.45 mm	No. of rotor bars	28
Rotor inner diameter	33.5 mm	Stator winding factor	0.96
Air gap thickness	0.275 mm	Stator winding layers	single/double
Stack length	125 mm	No. of turns for each coil	48/24
Skewing of rotor bars	1.5/36	No. of coils per-phase	4
End-winding reactance	0.12 Ω	No. of parallel branches	2
End-winding resistance	0.45 Ω	Steel type	M-45 29 GA
End-ring reactance	18.76 $\times 10^{-6}$ Ω	Wire 21 SWG area	0.5189 mm ²
End-ring resistance	4.21 $\times 10^{-6}$ Ω	No. of search coil turns	1

Table C-2 SEIG measured parameters and specifications

Three-phase, 5-hp, 4-pole 220 V, 16 A, 60 Hz, 1730 rpm, Δ -connected Squirrel-cage induction machine	
Parameter	Value
Stator resistance R_s	0.9649 Ω
Rotor resistance R_r	1.3046 Ω
Moment of inertia J_m	0.0138 Kg.m ²
Friction coefficient B_m	0.0021
Excitation capacitance C	36 μ F

Table C-3 Magnetizing and leakage reactance saturation parameters

Parameter	Value	Parameter	Value	Parameter	Value
k_1	111.7	k_4	3.807	c_2	3.45
k_2	97	k_{50}	2.003	c_{30}	0.1347
k_{30}	1.342	k_5	2.885	c_3	0.1182
k_3	1.9194	k_{60}	3.512	c_{40}	0.0105
k_{40}	2.353	c_1	0.1502	c_4	0.0058

Table C-4 Hardware and control systems parameters

Voltage source converter (VSC): three-phase, two-level IGBT inverter from SEMIKRON, SKM 50 GB 123D, 440 VAC, 30 A [76]			
Parameter	Value	Parameter	Value
Supply voltage V_s	220 V _{LL}	L_f	1 mH
Supply frequency f_s	60 Hz	R_f	0.12 Ω
Sampling time T_s	110 μ s	C_f	6.67 μ F
Delay time T_d	15 μ s	V_{dc}	300 V
Switching frequency f_{sw}	9 kHz	K_{pi}	1.43
Crossover frequency ω_c	450 rad/s	K_{ii}	171.43
τ_i	0.7 ms	K_{pv}	0.003
R_L	17-50 Ω	K_{lv}	0.4265